**Universidade de Aveiro**

Departamento de Engenharia de Materiais e Cerâmica

**2017**

**Laura Isabel Vilas Holz**

# Zircónia estabilizada com ítria com coloração bege

# Yttria-stabilized Zirconia with *beige* colour

**Universidade de Aveiro**

**2017**

Departamento de Engenharia de Materiais e Cerâmica

**Laura Isabel Vilas Holz**

# Zircónia estabilizada com ítria com coloração bege

# Yttria-stabilized Zirconia with *beige* colour

Relatório de Estágio apresentado à Universidade de Aveiro para cumprimento dos requisitos necessários à obtenção do grau de Mestre em Engenharia de Materiais realizado sob a orientação científica da Doutora Maria Margarida Tavares Lopes de Almeida, Professora Auxiliar do Departamento de Engenharia de Materiais e Cerâmica, coorientação da Doutora Florinda Mendes da Costa, Professora Associada do Departamento de Física da Universidade de Aveiro e do Doutor Nuno Vitorino, supervisor da empresa INNOVNANO.

Por ser uma verdadeira inspiração, dedico este trabalho ao meu irmão Tiago.

**O júri**

Presidente

Prof. Doutor Fernando Manuel Bico Marques
Professor Catedrático no Departamento de Engenharia de Materiais de Cerâmica da Universidade de Aveiro

Doutor Duncan Paul Fagg
Equiparado a Investigador principal na Divisão de Investigação em Nanotecnologia do Centro de Tecnologia Mecânica e Automação da Universidade de Aveiro.

Prof.ª Doutora Maria Margarida Tavares Lopes de Almeida
Professora auxiliar no Departamento de Engenharia de Materiais e Cerâmica da Universidade de Aveiro

**agradecimentos**

Ao longo da minha formação, tive o privilégio de me cruzar com pessoas maravilhosas que me ajudaram não só na realização deste trabalho, mas também na minha formação enquanto pessoa.

Começo por expressar o meu profundo agradecimento à Professora Margarida Almeida, pelo incansável apoio, extrema dedicação e presença ao longo deste trabalho. Pelo conhecimento científico, disponibilidade constante e generosidade ao longo da minha formação.

Agradeço à Professora Florinda Costa, pelo conhecimento científico, dedicação, preocupação e apoio ao longo destes meses. Pela disponibilidade incansável, pela sincera amizade e generosidade.

Ao Doutor Nuno Vitorino, por me integrar e orientar na INNOVNANO, pela disponibilidade prestada, pelo conhecimento científico, dedicação, apoio e generosidade.

Ao Doutor Javier Macias, pelas preciosas sugestões, generosidade, conhecimento científico e pelo apoio incansável ao longo do meu trabalho.

À Engenheira Ana e ao João Pedro pela genuína amizade. Pela incansável ajuda e apoio. Por tornarem os desânimos em ânimos e me motivarem todos os dias. Pela enorme generosidade.

A toda Equipa da INNOVNANO: Daniel, Cátia, Cristina, Patrícia e Henrique pelo espírito de entre ajuda, motivação, preocupação constante e dedicação.

À Rosa Soares pela sua disponibilidade, sincera amizade e incansável apoio.

Ao António Fernandes pela atenção dedicada, preciosas contribuições, constante apoio e amizade. Agradeço à Professora Teresa Monteiro, Professor Luís Rino e ao Roberto Costa pela ajuda despendida nas propriedades óticas.

À Equipa do DEMAC, por todo apoio técnico durante a caracterização das amostras, em especial à Eng. Marta Ferro e Eng. Ana pelo apoio prestado.

À Regina Santos que possibilitou as minhas idas à empresa, pela generosidade e amizade.

Agradeço ao Gonzalo e ao Ricardo pela atenção e ajuda.

Aos meus Tios, Maria e José Guimarães, que se tornaram essenciais ao longo dos anos. Por me terem dado sempre a mão.

Aos verdadeiros Amigos.

Aos meus colegas de curso que se tornaram uma segunda família essencial ao longo dos anos.

Aos meus Irmãos Nina, Tiago e Marianna que são a minha força motriz em tudo na vida, por me ensinarem que só o amor vence e que só juntos somos mais fortes. E por fim agradeço profundamente à Minha Mãe, a mulher mais maravilhosa que alguma vez já conheci.

**keywords** Zirconia, 2YSZ, defects, colour centers, doping, iron oxide, mechanical properties

**abstract**

Zirconia is a very versatile advanced ceramic that offers an interesting combination of thermal, chemical, electrical, mechanical and optical properties which are uncommon to find in ceramic materials and therefore is used in several applications. INNOVNANO is one of the main Zirconia powders suppliers in the market with potential clients for *beige* YSZ ceramics with specific mechanical properties.

Thus, the work performed during this internship aimed to develop a material that meets the requested requirements, having as reference a sample provided by an INNOVNANO's client which colour was intended to be reproduced but which composition and processing were unknown. In this way, the work began with reference material characterization through Scanning Electron Microscopy, X-ray Diffraction, Raman Spectroscopy, Photoluminescence and Diffuse Reflectance in order to understand the colouring mechanism, which was shown to be based on structural defects developed under reducing conditions.

The introduction of extrinsic defects by doping with iron oxide ($Fe_2O_3$) in the matrix of 2 mol % yttria-stabilized Zirconia (2YSZ) was the alternative selected for the reproduction of the requested colour. The samples were studied from the microstructural, structural and optical point of view. Doping with iron oxide has proved to be a suitable, reproducible and irreversible colouring mechanism allowing the development of a chromatically stable material with respect to its use in different processing conditions such as different atmospheres and temperature ranges. Colour stability was proved by thermal treatments in oxidizing and reducing atmospheres.

The effect of dopant addition on the mechanical properties of Zirconia was studied by evaluating the fracture toughness ($K_{IC}$), Vickers hardness (HV10) and flexural strength ($\sigma_{flexural}$) in samples with high tetragonal Zirconia content (> 92%) and high relative density (> 96%). The developed material fulfils the requirements previously defined by INNOVNANO, but a slight decrease of the fracture toughness with the addition of dopant was observed while Vickers hardness and flexural strength were not significantly affected by the addition of $Fe_2O_3$.

**palavras-chave** Zircónia, 2YSZ, centros de cor, defeitos, dopagem, óxido de ferro, propriedades mecânicas

**resumo**

A Zircónia é um cerâmico avançado que se tem destacado como um material versátil e promissor, apresentando uma combinação interessante de propriedades térmicas, elétricas, óticas e mecânicas, pouco comuns nos materiais cerâmicos, sendo por isso utilizada em diversas aplicações. A empresa INNOVNANO produz pós de Zircónia com diferentes características e atualmente tem clientes interessados em cerâmicos à base de Zircónia estabilizada com ítria de coloração bege com propriedades mecânicas específicas.

Assim, o trabalho realizado neste estágio pretendeu desenvolver um material que cumpra os requisitos solicitados, tendo como referência uma amostra cedida por um cliente da INNOVNANO cuja cor se pretendia reproduzir, mas cuja composição e processamento eram desconhecidos. Deste modo, o trabalho teve início com a caracterização da amostra de referência através de Microscopia Eletrónica de Varrimento, Difração de raios X, espectroscopia de Raman, Fotoluminescência e Refletância Difusa de modo a permitir compreender o mecanismo de coloração, o qual mostrou ser baseado em defeitos estruturais, desenvolvidos em condições redutoras.

A introdução de defeitos extrínsecos pela dopagem com óxido de ferro ($Fe_2O_3$) na matriz da Zircónia estabilizada com 2 mol % de ítria (2YSZ) foi a alternativa selecionada para a reprodução da cor solicitada. As amostras foram estudadas do ponto de vista microestrutural, estrutural e ótico. A dopagem com óxido de ferro revelou ser um mecanismo de coloração adequado, reprodutível e irreversível, permitindo o desenvolvimento de um material cromaticamente estável no que concerne à sua utilização em diferentes condições de processamento, tais como diferentes atmosferas e intervalos de temperatura. A estabilidade da cor foi confirmada com tratamentos térmicos em atmosferas oxidantes e redutoras.

O efeito da adição do dopante nas propriedades mecânicas da Zircónia foi estudado, avaliando-se a tenacidade à fratura ($K_{IC}$), a dureza de Vickers (HV10) e a resistência à flexão ($\sigma_{flexural}$) em amostras com elevado teor de Zircónia tetragonal ( >92 %) e com elevada densidade relativa ( >96%). Os materiais desenvolvidos preenchem os requisitos previamente definidos pela INNOVNANO, tendo-se observado, contudo, um ligeiro decréscimo da tenacidade à fratura com a adição de dopante. Já a dureza Vickers e a resistência à flexão não foram significativamente afetadas pela adição de $Fe_2O_3$.

# Index

## List of Figures

## List of Tables

## List of Abreviations

| | |
|---|---|
| Y-TZP | Tetragonal Zirconia Polycrystals |
| EDS | Emulsion Detonation Synthesis |
| YSZ | Yttria-stabilized Zirconia |
| LTD | Low Temperature Degradation |
| 2YSZ | 2 mol % yttria-stabilized Zirconia |
| m-$ZrO_2$ | Monoclinic Zirconia |
| t-$ZrO_2$ | Tetragonal Zirconia |
| c-$ZrO_2$ | Cubic Zirconia |
| t'-$ZrO_2$ | Non-transformable Zirconia |
| r-$ZrO_2$ | Rhombohedral Zirconia |
| FSZ | Fully-stabilized Zirconia |
| PSZ | Partially-stabilized Zirconia |
| RT | Room Temperature |
| CIP | Cold Isostatic Pressing |
| HIP | Hot Isostatic Pressing |
| PL | Photoluminescence |
| SEM | Scanning Electron Microscopy |
| SEM/EDXA | Scanning Electron Microscopy / Energy Dispersive X-ray Analysis |
| SSA | Surface Specific Area |
| XRD | X-ray Diffraction |
| XRF | X-ray Fluorescence |
| XPS | X-ray Photoelectron Spectroscopy |

# CHAPTER 1

## 1. Introduction and Objectives

## 1.1. Introduction

Zirconium dioxide ($ZrO_2$) was recognized in 1789 by the German chemist Martin Klaproth in the reaction products obtained after heating some gems and it was used for an extensive time mixed with rare earth oxides as pigment in ceramics [1]. In 1975, Garvie proposed a model to justify the outstanding mechanical behaviour of Zirconia, by virtue of which it has been termed "ceramic steel" [2,3]. Zirconia based materials have a diversity of unique physicochemical, electrical and mechanical properties including high strength, hardness, fracture toughness, wear resistance, low friction coefficient, high melting point, chemical inertness, low thermal conductivity and biocompatibility. These properties account for the wide range of applications, from wear resistant ceramic bearings to medical and surgical instruments. The high temperature ionic conductivity makes the cubic zirconia ceramics suitable as solid electrolytes in fuel cells and in oxygen sensors. This material, with its high fracture toughness, due to the inherent and well-known phase transition similar to martensitic transformations in steels, is classified as an engineering ceramic [4].

Several studies have been published regarding the investigation of the transformation toughening mechanism associated with the tetragonal (t) to monoclinic (m) phase transformation present in Zirconia. The occurrence of this transformation and its relationship to improve the mechanical properties, including fracture toughness and strength, contributes for a high crack propagation resistance. The phase nature and microstructure can be tailored by a suitable choice of dopant oxides, combined with appropriate choice of sintering conditions and heat treatments. The amount of stabilizer, such as yttria ($Y_2O_3$), ceria ($CeO_2$), calcia (CaO) and magnesia (MgO), which are the most studied stabilizers used, has to be controlled carefully as it determines the phase stability or transformability, and the mechanical properties of the final product [5,6].

The high strength of yttria-tetragonal zirconia polycrystal (Y-TZP) is derived from the tetragonal to monoclinic stress-induced transformation: under stress, at the crack tip, tetragonal grains transform into the monoclinic phase. This transformation is accompanied by an increase in volume and shear strain thus closing the crack tip and avoiding further crack propagation. The most attractive compositions for transformation toughening are those with low yttria concentrations (but high enough to prevent spontaneous t-m transformation during cooling), typically 2–3 mol % $Y_2O_3$. For these reasons, yttria stabilized zirconia (YSZ) seems to be a promising ceramic engineering to be used as a "ceramic steel". However, many of these attractive features of zirconia, especially fracture toughness and strength, are compromised after prolonged exposure to water vapor at intermediate

temperatures (~30ºC –300ºC) in a process referred as low-temperature degradation (LTD), identified over two decades ago [5,7,8].

The interest in obtaining coloured zirconia without damaging its promising properties, led to more detailed studies about the effect of coloured dopants on mechanical properties. Coloured zirconia can be obtained by small additions of various metal oxides to the starting powder [9]. Several metal oxides have been tested to pigment zirconia by mixing powders, among them, $Fe_2O_3$ and $CeO_2$ were considered as having minor adverse effects on the mechanical properties of zirconia ceramics [10]. Based on some investigations [11, 12], the effect of $Fe_2O_3$ doping on mechanical and optical properties of 2 mol % yttria-stabilized zirconia (2YSZ) will be discussed during this work.

## 1.2. INNOVNANO

INNOVNANO is a Portuguese company stablished in Coimbra since 2009, part of CUF- the largest chemical company in Portugal – and it is dedicated to nanostructured yttria-stabilized zirconia (YSZ) powders manufacturing, using Emulsion Detonation Synthesis (EDS) as a unique production method.

Through EDS, INNOVNANO produces a range of nanostructured zirconia ceramic powders that can be tailored for unique structures and properties, ideally suitable for industrial applications that demand high material performance such as thermal barrier coatings (TBC), hard-wearing components (cutting tools, grinding materials and others), energy materials (thin-films transparent conducting oxides (TCOs)) and biomaterials [13].

### 1.2.1. Emulsion Detonation Synthesis

Emulsion Detonation Synthesis (EDS) is a unique approach to the manufacturing of ceramic powders developed and patented by INNOVNANO. Based on gaseous-phase synthesis, two water-in-oil (W/O) emulsions (precursor mix) are detonated under high temperatures (from 500 to 3000 ºC), high pressures (>10 GPa) and rapid quenching ($10^9$ $K.s^{-1}$) to produce powders with small grain size and enhanced homogeneity, as it can be seen from Figure 1.1 [14].

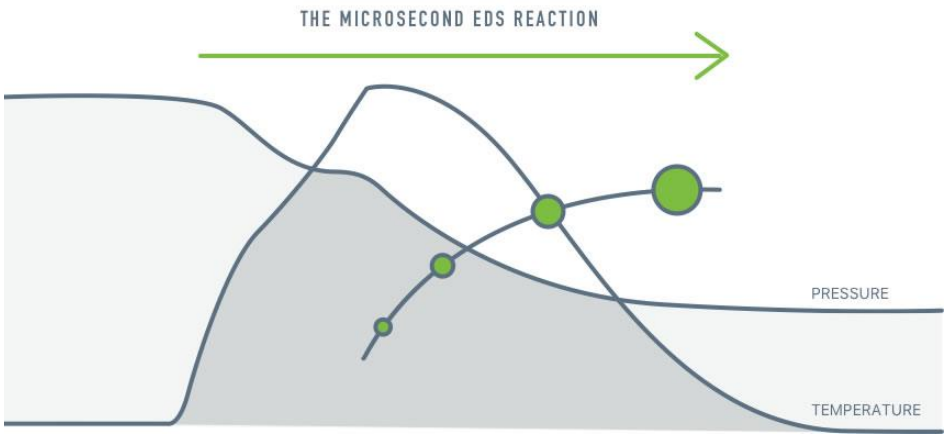


Figure 1.1 – Schematic representation of the Emulsion Detonation Synthesis (EDS) method [14].

There are two phases in the water-in-oil emulsion matrix - an external oil phase (combustible) and an internal aqueous phase (oxidizer). A variety of high purity soluble powder precursors are uniformly dispersed into the emulsion matrix, which has a high contact surface between the combustible and oxidizer phases [15].

The detonation is a very high speed chemical reaction and produces nanostructured ceramic powders with extremely favourable properties compared to conventional micrometric powders such as [14]:

- High chemical homogeneity;
- High density;
- Uniform grain sizes;
- Low sintering temperature;
- High specific surface area;
- High mechanical properties.

Close control of dopant concentration by EDS helps to optimize the powder to a particular end application. Grain growth is also minimized by low sintering temperatures that helps maintain a uniform microstructure [15] .

## 1.3. Motivation and Objectives

Nowadays, several companies are well-established in the market with the ability to provide tuned formulations according to the requirements of each client, particularly *beige* colour zirconia (bulk and powders).

INNOVNANO is one of those companies, being one of the main YSZ powders suppliers in the market, currently working on the development of a new 2YSZ *beige* grade ceramics combining outstanding properties, with potential clients for 2YSZ ceramics, if the following requirements are met:

- *Beige* colour;

- Physical/Mechanical properties in the following ranges:

  - Sintered density ($g/cm^3$): > 6.00 $g/cm^3$
  - Biaxial flexural strength (MPa): 1000-1200
  - Fracture toughness ($MPa.m^{0.5}$): > 8
  - Hardness, HV10 (MPa): > 1200

The aim of this work was to go through in a deep investigation of the reference sample collecting hints to overcome a zirconia formulation which physical properties meet the reference material.

In order to fulfill these requirements an investigation of the mechanical and optical properties, specifically the colour, was developed starting from commercial 2YSZ produced by EDS. Within the different strategies to get colours, the use of colouring oxides such as iron oxide ($Fe_2O_3$) was the chosen strategy, once the incorporation of specific ions into the $ZrO_2$ matrix can be used to tune zirconia colour while phase stabilization can enhance its mechanical properties such as hardness, biaxial flexural strength and fracture toughness [12,16].

## 1.4. Document Structure

This document is organized into five chapters. The first one is dedicated to a general introduction, objectives and the motivation behind the realization of this work. The literature review is presented in chapter two as also as an overview of zirconia material properties. In chapter three, the experimental procedure and the characterization techniques used to evaluate the morphology, structural, mechanical and optical (specifically, the colour) properties of the produced samples and of the reference material are described. The results of this characterization are presented and discussed in chapter four. The last chapter is dedicated to the main findings/conclusions and future work.

# CHAPTER 2

## 2. Literature Review

## 2.1. Zirconia

At atmospheric pressure, pure zirconia, which can be found in nature as a natural mineral called Baddeleyite (β-$ZrO_2$), exists in one of three crystalline phases depending upon the temperature, as it can be seen from Figure 2.1. At around 1170 ºC the monoclinic (m) phase transforms into the tetragonal (t) phase, which is thermally stable until around 2370 ºC. At this temperature zirconia changes to cubic (c) which remains until the melting point (~2700 ºC) [17].

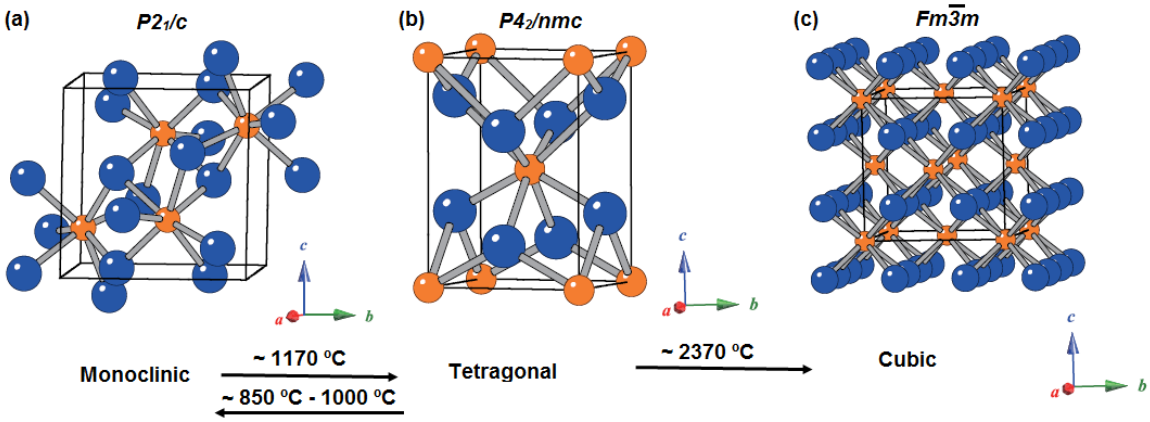


Figure 2.1 - Monoclinic (a), tetragonal (b) and cubic (c) $ZrO_2$ unit cells and space groups. The large light blue spheres and small orange ones represent O and Zr atoms, respectively. Phase transition temperatures: monoclinic to tetragonal (m-t) and tetragonal to cubic (t-c) are also represented (adapted from [17]).

The monoclinic structure belongs to the *P2₁/c* space group with lattice parameters of *a*=5.31 Å, *b*=5.21 Å, *c*=5.15 Å and β=99.2˚(see appendix A). This phase is very stable under natural conditions (atmospheric pressure) and this structure can be seen as a result of high distortion of the cubic structure. On the other hand, tetragonal phase has a slightly distorted fluorite structure and it belongs to the *P4₂/nmc* space group with the lattice parameters *a*=*b*=3.60 Å and *c*= 5.15 Å (see appendix B). The cubic zirconia phase has a face-centred cubic fluorite-type structure, belonging to the space group $Fm\bar{3}m$ with a lattice parameter of *a*= 5.12 Å [18]. Although c-$ZrO_2$, t-$ZrO_2$ and m-$ZrO_2$ are the commonly reported phases, other zirconia phases such as non-transformable tetragonal (t'-$ZrO_2$) and rhombohedral (r-$ZrO_2$) can be found under certain conditions (for example, at high pressures) [18].

Table 2.1 summarizes the structural characteristics of $ZrO_2$ phases at atmospheric pressure. The density values of different crystalline zirconia structures displayed in the table consider only pure $ZrO_2$, once the density values are affected by stabilizers addition.

Table 2.1 – Crystallographic data of pure $ZrO_2$ at atmospheric pressure (adapted from [18]).

| $ZrO_2$ Phase | Space Group | Lattice parameters | Theoretical density ($g/cm^3$) |
|---|---|---|---|
| **Monoclinic** | $P2_1/c$ | $a$=5.31 Å, $b$=5.21 Å, $c$=5.15 Å; α=γ=90º, $\beta$=99.22 º | 5.82 |
| **Tetragonal** | $P4_2/nmc$ | $a$=$b$=3.60 Å; $c$=5.15 Å; α=β=γ=90º | 6.13 |
| **Cubic** | $Fm\bar{3}m$ | $a$=$b$=$c$=5.12 Å; α=β=γ=90º | 6.09 |

## 2.2. Zirconia Phase Transformation

When attempts are made to fabricate dense ceramics of pure $ZrO_2$ by sintering at high temperatures there is, as mentioned above, an increase in volume of approximately 3 to 5% associated with the tetragonal-to-monoclinic phase transformation when the material cools from the sintering temperature [19].The volumetric change associated with this phase transformation is large enough to affect the structural integrity of the material, causing extensive micro cracking and failure of the sintered ceramic. Therefore, pure $ZrO_2$ is not used for structural applications. However, the same martensitic tetragonal-to-monoclinic transformation, occurring without diffusion and involving only a cooperative shift of the ions from its starting positions, has a great technological importance for mechanical applications since it is the basis for the toughening process of ceramic components [3].

The phase transformation toughening process can be described as follows: tetragonal particles can be preserved in a densely sintered structure down to room temperature (RT), however metastable. A micro-crack rising under stress and its impact on the particle causes the transformation into the stable monoclinic phase. This transformation releases energy creating compressive stresses, hence slowing the crack growth or splitting the crack into reduced and less risky cracks: this is the cause for the increase in the strength (Figure 2.2) [20, 21].

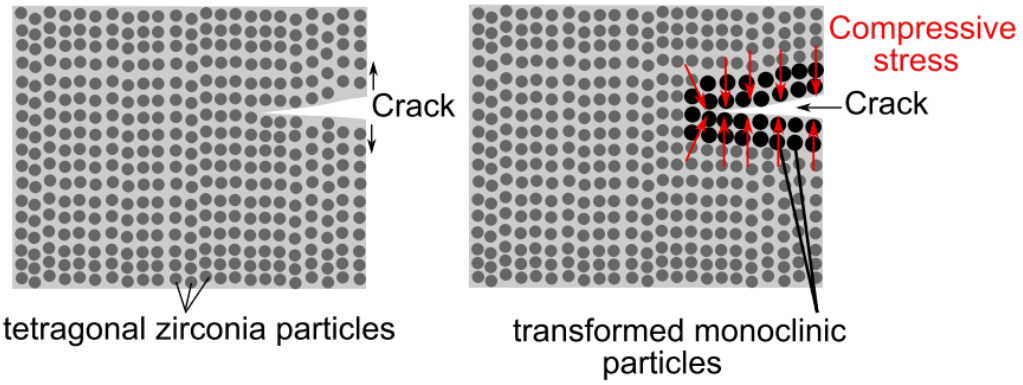


Figure 2.2 - Illustration of the stress-induced toughening process. The crack propagates through the material and grains surrounding the crack are transformed from tetragonal into monoclinic [22].

For the effective contribution of the transformation toughening the retention of the maximum amount of t-$ZrO_2$ at RT is needed. This fraction of t-retained is dependent on the grain size, on the stabilizer content such as $Y_2O_3$, $CeO_2$ and CaO and on the sintering conditions.

The thermodynamic approach, based on the total energy involved in the t → m transformation, expressed in terms of different energy contributions to the overall energy of transformation, was discussed by Lange [6].The change of total free energy ($\Delta G_{t\to m}$) for the particle transformation can be written as expressed in Equation 2.1:

$$\Delta G_{t\to m} = \Delta G_C + \Delta U_{SE} + \Delta U_S \qquad \textbf{(Equation 2.1)}$$

where $\Delta G_C$ is the difference in chemical free energy between the tetragonal and monoclinic phases and this term is dependent on temperature and composition, including the oxygen vacancies concentration; $\Delta U_{SE}$ is the change in elastic strain free energy associated with the t-m transformation and it is dependent on the modulus of the surrounding matrix, the size and shape of the particles as well as the presence of internal or external stresses; $\Delta U_s$ is the change of surface free energy associated with the formation of new interfaces, when transformation occurs, for instance, cracks. According to this approach, the particle remains in its tetragonal form if the overall thermodynamic driving force $\Delta G_{t\to m} > 0$. The total free energy can be increased and the tetragonal phase can be retained by decreasing the difference in chemical free energy by alloying with a stabilizing dopant oxide (e.g. yttria, ceria, calcia and magnesia). It also can be preserved by increasing the elastic strain free

energy change by dispersing the tetragonal phase in a constraining elastic matrix (e.g. alumina, cubic zirconia) or even by increasing the surface free energy change (e.g by reducing the tetragonal grain size) [5].

## 2.3. Low Temperature Degradation

The t-m phase transformation together with the volume expansion occurs without external stress in humid air environment, resulting in a crack propagation and deterioration of the mechanical properties. The premature failure of stabilized zirconia under humid environment, from room temperature to 400 ºC, is known as low temperature degradation (LTD) phenomenon [23]. The incorporation of water into the zirconia matrix, promotes the t-m transformation which spreads gradually along the surface and penetrates into the depth of the material in a process which has been called as ‘‘nucleation-and-growth’’ process [24], as it can be seen from Figure 2.3. Fabris *et al.* suggested that the moisture species penetrate into the tetragonal lattice, destabilizing the oxygen ion vacancies, causing loss of strength and microcracking [25].

This process is initiated at isolated surface grains, where water is incorporated into the zirconia lattice by disrupting Zr–O–Zr bonds. The existence of oxygen vacancies formed during zirconia stabilization triggers the diffusion of hydroxide ions and thereby accelerates the degradation. According to Kohorst and co-workers [24], yttria stabilized zirconia seems to be tremendously vulnerable to low temperature degradation caused by the t-m transformation. They also found that both alumina and ceria, as stabilizing oxides, reduce the susceptibility of zirconia to hydrothermal degradation and the alternative use of these oxides may enhance the long-term stability of tetragonal zirconia [24].

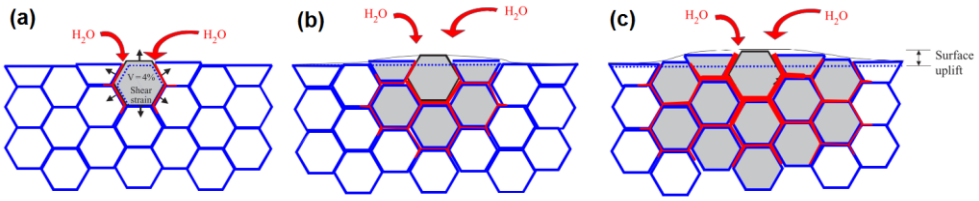


Figure 2.3 – Schematic illustration of LTD phenomenon: (a) Nucleation on a particular grain at the surface, leading to microcracking and stresses to the neighbour’s grains. (b) Growth of the transformed zone, leading to extensive microcracking and surface roughening. (c) Water penetration in the zirconia matrix. Transformed grains are in grey and red path represent the penetration of water due to microcracking around the transformed grains [8].

In the overall context of toughening process, the transformability of stabilized tetragonal phase plays an important role. Taking this fact into account, the t-$ZrO_2$ transformability should be discussed in detail.

The mechanism behind zirconia stabilization is still an open question: at room temperature various tetragonal phase stabilization mechanisms have been proposed by different research groups. The contribution of different processing variables in these investigations makes the proposed mechanisms valid only for the specified set of experimental conditions [26].

The thermodynamic stability of the monoclinic structure of zirconia at RT is associated with the strong covalent nature of the Zr-O bond. Since the ionic radius of $Zr^{4+}$ (0.84 Å) is very low, the distances between the oxygen ions in the zirconia lattice are small and electrostatic repulsion forces induce the distortion of dense ion package. In fact, this promote the formation of a more distorted crystalline structures as is the case of the monoclinic structure [22, 26].

By the addition of metal oxide dopants having fluorite-type cubic crystalline structure and moderately high solubility in $ZrO_2$, it is possible to retain the $ZrO_2$ in the tetragonal and/or cubic phases at room temperature. The oxides most commonly used to stabilize the higher temperature phases are calcia (CaO), magnesia (MgO), yttria ($Y_2O_3$) and ceria ($CeO_2$) [19].

Depending upon the nature and amount of stabilizing oxide added, $ZrO_2$ can be described as either fully or partially stabilized. Fully-stabilized zirconia (FSZ) occurs when the dopant level is such that the microstructure contains entirely cubic grains. Partial-stabilization (PSZ) occurs when the dopant concentration is less than the required for full stabilization and so results in a microstructure that consists either of a mixture of tetragonal and cubic phases, such as in partially-stabilized (PSZ), or almost entirely tetragonal phase, such as in tetragonal polycrystal (TZP) ceramics. As monoclinic phase is the stable form, it may be present in these microstructures [19,21].

As mentioned before, different ions can be used to stabilize tetragonal and cubic phases at RT. According to stabilizer valence, different mechanisms were proposed. The replacement of $Zr^{4+}$ by cations with lower valence, usually trivalent cations, results in the generation of oxygen ion vacancies due to charge balance. The oxygen vacancies can be controlled by the dopant amount and both high temperature phases can be stabilized at RT (see Figure 2.4) [22,26].

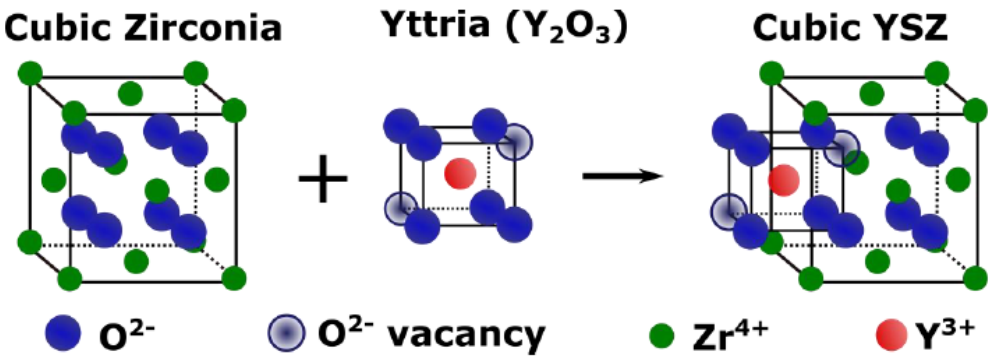


Figure 2.4 – Cubic structure of yttria stabilized zirconia [22].

However, other mechanisms are reported as responsible of cubic and tetragonal phases stabilization, without generating oxygen vacancies. For example, doping the pure zirconia with tetravalent cations such as $Ce^{4+}$, which have the same valence of $Zr^{4+}$ do not generate these defects. In this case, the stabilization is also efficient and is explained by the effect of cation size. The replacement of some $Zr^{4+}$ by cations with a higher ionic radius induces an increase in the ratio between cation and anion radius. Therefore, an higher average distance between the ions is responsible by a decrease in the electrostatic repulsion, inducing more symmetric crystalline structures of zirconia, as is the case of tetragonal and cubic phases [22].

According to the final desired applications, the dopant nature and concentration can be adjusted since the physical, mechanical and thermal properties are strongly influenced by them. Table below summarizes the magnesia partial stabilized zirconia (Mg-PSZ), yttria stabilized tetragonal zirconia polycrystals (3Y-TZP) and yttria fully stabilized zirconia (8Y-FSZ) properties.

Table 2.2 – Properties of different $ZrO_2$ products [22].

| Properties | | Material | | |
|---|---|---|---|---|
| | | Mg-PSZ | 3Y-TZP | 8Y-FSZ |
| **Density** | ($g/cm^3$) | 5.60 | 6.05 | 5.7 |
| **Flexural strength (20 ºC/800 ºC)** | MPa | 545/354 | 1400/270 | 180/270 |
| **Compressive strength** | MPa | 1700 | 2000 | 1500 |
| **Modulus of elasticity** | GPa | 205 | 205 | 160 |
| **Poisson ratio** | | 0.31 | 0.30 | 0.3 |
| **Hardness** | $HV_{0.3}$, MPa | 1120 | 1350 | 700 |
| **Fracture Toughness** | $MPa.m^{0.5}$ | 6.0 | 5 | 3.5 |
| **Thermal expansion coefficient** | $x10^{-6}$ $K^{-1}$ | 10 | 10 | 11 |
| **Thermal conductivity** | W/mK | 2.5 | 2 | 2.5 |
| **Thermal shock resistance** | ∆T ºC | 375 | 250 | 200 |
| **Specific heat capacity** | J/kgK | 400 | 400 | - |

### 2.3.1. Yttria Stabilized Zirconia

Yttria is the most commonly used stabilizer in high-tech applications of zirconia once yttrium solubility in the zirconia lattice is much higher comparatively with the solubility of other ions usually used in the zirconia stabilization. Consequently, comparing the phase diagram of $ZrO_2$-$Y_2O_3$ system with others such as $ZrO_2$-CaO and $ZrO_2$-MgO systems, a much larger tetragonal solid solution field exist [27].

The introduction of $Y_2O_3$ into the $ZrO_2$ lattice gives origin to oxygen vacancies which are one of the mechanisms proposed for the stabilization effect, as mentioned before [23]. An important feature of the $ZrO_2$-$Y_2O_3$ phase equilibrium is the stabilization of high temperature cubic and tetragonal phases at room temperature by the incorporation of $Y^{3+}$ cations into the zirconia matrix. The most attractive compositions for transformation toughening are those with low yttria concentrations (but high enough to prevent spontaneous t-m transformation during cooling), typically 2– 3 mol% $Y_2O_3$ [6].

The partial phase diagram of the system $ZrO_2$-$YO_{1.5}$ is presented in Figure 2.5. As it can be seen, for a low content of $YO_{1.5}$ (0-5 mol.%), a narrow area of two phases (m + t) occurs, in the range of temperatures above the temperature in which monoclinic phase is presented. During heating, for the same range of $YO_{1.5}$ content, this two-phase area is followed by a

tetragonal phase area (t-phase). Subsequently, increasing the yttria content means decreasing t⟶m transformation. This tetragonal phase that exists in a range of $YO_{1.5}$ content between 0-5 mol.% is classically called as transformable tetragonal phase, since during cooling it transforms into monoclinic form. As explained previously, t⟶m can be induced by mechanical loading, once tetragonal is a metastable phase. For higher contents of $YO_{1.5}$ there is two-phase area comprising a mixture of cubic phase (c-phase) and a non-transformable tetragonal phase (t'-phase). The fast cooling starting from temperatures in a range of cubic solid solution, of samples with $YO_{1.5}$ content between 4-13 mol.% undergo a phase transformation to the t'-phase. This untransformable (t'-phase) does not transform into monoclinic phase and the limit of $YO_{1.5}$ contents in each metastable tetragonal and cubic phase that it is possible to retain at RT is specified in red [22, 28].

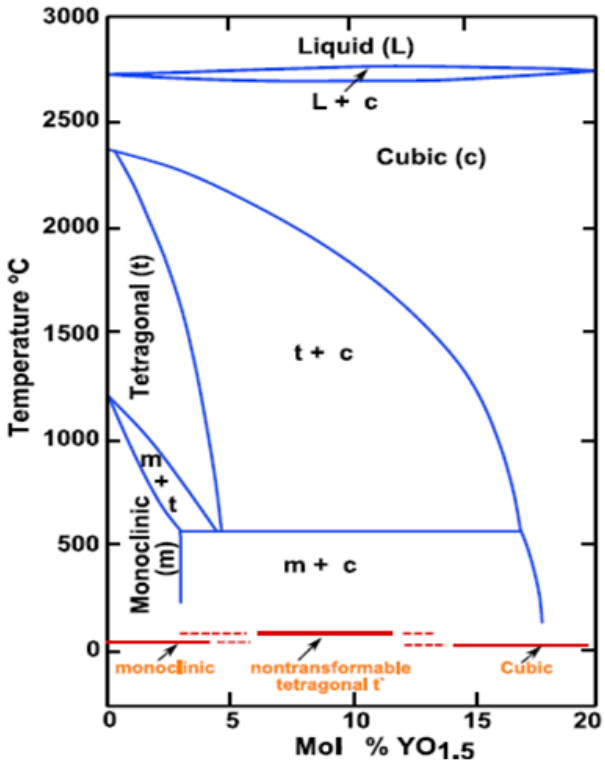


Figure 2.5 - $Y_2O_3$-$ZrO_2$ partial phase diagram. m, t and c denote the monoclinic, tetragonal and cubic phases, respectively [22, 28].

From the thermodynamic point of view, the tetragonal phase can be stabilized by addition of sufficient stabilizing dopants, since its free energy decreases with the increasing dopant content. However, thermodynamically metastable phases (t or c) can also be retained at room temperature if there is insufficient energy to overcome the activation energy barrier of

transformation, ΔG*. Adopting the Kröger-Vink notation, the defect reaction for zirconia doped with yttria can be written as expressed in Equation 2.2:

$$Y_2O_3 \xrightarrow{ZrO_2} 2Y_{Zr}^{'} + 3O_o^x + V_0^{\bullet\bullet} \qquad \textbf{(Equation 2.2)}$$

where $Y_{zr}^{'}$ indicates an *Y* atom occupying a *Zr* lattice site, $O_o^x$ represents an oxygen atom occupying a normal lattice site and $V_o^{\cdot\cdot}$ expresses a vacancy at an oxygen lattice site. An increase in oxygen vacancy concentration increases disorder in the $ZrO_2$-$Y_2O_3$ system and so increases the stability of the tetragonal phase [5].

In the F. Lange study [29], detailed grain-size measurements were made as function of yttria content. Powders containing 0, 1.5, 2.0, 2.5, 3.0 and 3.5 mol % $Y_2O_3$ were cold uniaxially pressed and sintered for 2h at temperatures ranging from 1200-1600 ºC. As expected, the average grain size is strongly affected by sintering temperature, as it can be seen from Figure 2.6 (a). F. Lange [29] attributed a critical grain size where tetragonal retention is superior to 90 %. According to this investigation, for a content of 2 mol% of yttria, the critical grain size is about 0.2 µm while for a content of 3 mol% of yttria, the critical grain size is around 1 µm, as illustrated in Figure 2.6 (b). As it can be seen, the fraction of tetragonal phase retained is dependent on the grain size and on the yttria content.

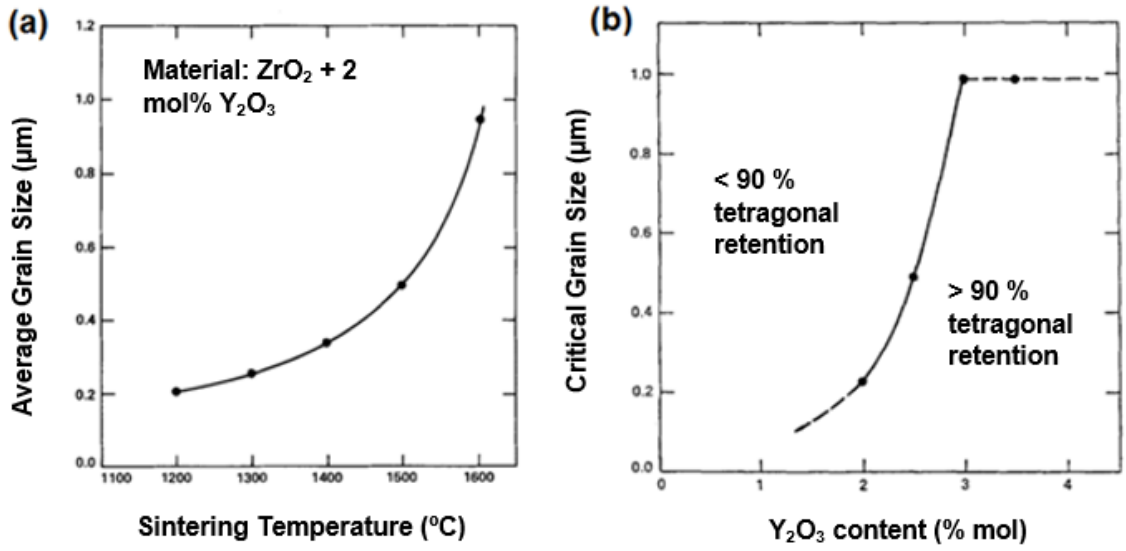


Figure 2.6 – (a) Average grain size as function of sintering temperature determined for 2YSZ composition; (b) Critical grain size versus $Y_2O_3$ content in tetragonal $ZrO_2$ [29].

It is reported [19] that the tetragonal phase in $ZrO_2$ has much slower grain growth kinetics compared to those of the monoclinic and cubic phases. For example, the effect of composition on the crystallographic phase content and grain growth in the $Y_2O_3$ system at 1400 ºC is illustrated in Figure 2.7. As it can be seen, the monoclinic and cubic phases in $ZrO_2$ have much faster grain growth kinetics. Guo *et al.* [12] suggested that grain growth depends on the phase content and that grain growth of cubic phase YSZ is 30-35 times faster than the tetragonal phase.

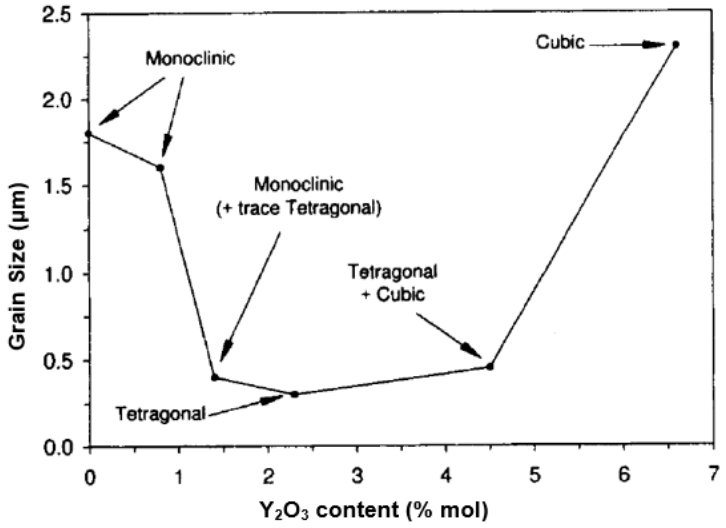


Figure 2.7 -Relationship between grain size, $Y_2O_3$ content and crystallographic phase content in $ZrO_2$ sintered at 1400 ºC for 1 h [19].

This was in concordance with K. Matsui *et al.* [30] study who shows typical scanning electron microscopy (SEM) images of 2YSZ, 3YSZ and 8YSZ sintered at 1500 ºC. The grain size was remarkably larger in 8YSZ material as illustrated in Figure 2.8.

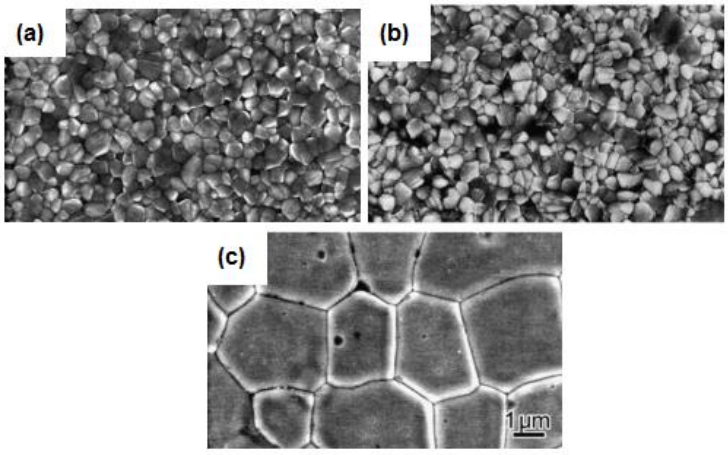


Figure 2.8 – SEM images with same magnification of (a) 2YSZ, (b) 3YSZ and (c) 8YSZ.

Lange *et al.* [19] attributed the relatively slow grain growth in Y-TZP to small variations in yttrium content between adjacent tetragonal grains and within tetragonal grains. As the unit cell size is dependent on composition, variation in composition means to produce a differential in lattice parameters which reflect on lattice strain energy. During sintering, grain boundary movement without composition adjustment produces a continuous strained interface, which inhibits further grain movement. Hence, as the grains become larger, the radius of the curvature of the grain boundaries decreases and the driving force for grain boundary movement also decreases. However, Lee and Chen [19] proposed other alternative mechanism to explain the slower grain growth of tetragonal phase. According to them, this phenomenum is due to a solute drag mechanism arising from the segregation of yttrium at the grain boundaries of the tetragonal grains. Indeed, the solute segregate near the grain boundaries but still remain within the grains. As cation diffusion in $ZrO_2$ is slower than oxygen diffusion, grain boundary mobility can be decreased by a called drag effect by cation solutes.

### 2.3.2. Mechanical Properties of YSZ

One important effect of the zirconia stabilization is the great improvement in the strength of zirconia ceramics. In fact, it is well known that the strength and fracture toughness of structural ceramics are strongly influenced by the particle size, the starting powder chemical composition and the sintering parameters. Since the mid-1990s, several new technologies have been developed envisaging the production of submicron, ultrapure $ZrO_2$ powders with a narrow size distribution. Hydroxide coprecipitation or alkoxide hydrolysis, gel precipitation,

micro emulsion techniques, sol-gel, hydrothermal synthesis and gas phase reaction-plasma coating are examples of some technologies that have been used [31].

Various parameters influence the transformability of t-$ZrO_2$ and the table below summarizes the literature results reporting the toughness of $ZrO_2$ ceramics, stabilized with 2 mol % yttria. It should be noted that the variation in toughness is largely related to the variation in grain size and to the use of different measurement techniques [31]. The reported toughness varying between 5.0 and 11.0 MPa.$m^{0.5}$ is dependent on the sintering parameters and the microstructural variables.

Table 2.3 – Literature results summary of the fracture toughness of 2YSZ [5]. Different processing routes: PS, pressureless sintering; HP, hot pressing. Various toughness measuring techniques: ISB, indentation of strength in bending.

| **Yttria (mol %)** | **Processing** | **Phases** | **Grain Size (μm)** | **$K_{Ic}$ (MPa. $m^{0.5}$)** | **Toughness Measurement** |
|---|---|---|---|---|---|
| **2.0** | PS, 1500 ºC, 1 hour | Monoclinic ~ 10% | 0.51 | 5.0 | ISB |
| | PS, 1500 ºC, 10 hours | Monoclinic ~ 15 % | 0.89 | 6.8 | |
| | PS, 1500 ºC, 80 hours | Monoclinic ~ 20 % | 1.87 | 12.4 | |
| | Presintering, at 1200 ºC. 12 hours | ~ 35 % tetragonal | - | 5.0 | Indentation |
| | Presintering at 1250 ºC, 12 hours | ~ 55 % tetragonal | - | 5.5 | |
| | 1200 ºC, 12 hours and HP 1450 ºC. 2 hours | ~ 99 % tetragonal | - | 11.0 | |
| | 1250 ºC, 12 hours and HP 1450 ºC, 2 hours | ~100 % tetragonal | - | 11.0 | |

Fracture toughness data from the literature are plotted against yttria content in Figure 2.9 (a). In general, toughness increases with decreasing yttria content (related with transformable tetragonal available, see Figure 2.5). The significant scatter in toughness noted at both 3 and 2 mol-%$Y_2O_3$ can be attributed to variation in grain size as well as the use of different measurement techniques. In general, high indentation toughness (>10 MPa.m$^{0.5}$) is measured at yttria contents < 2 mol %.

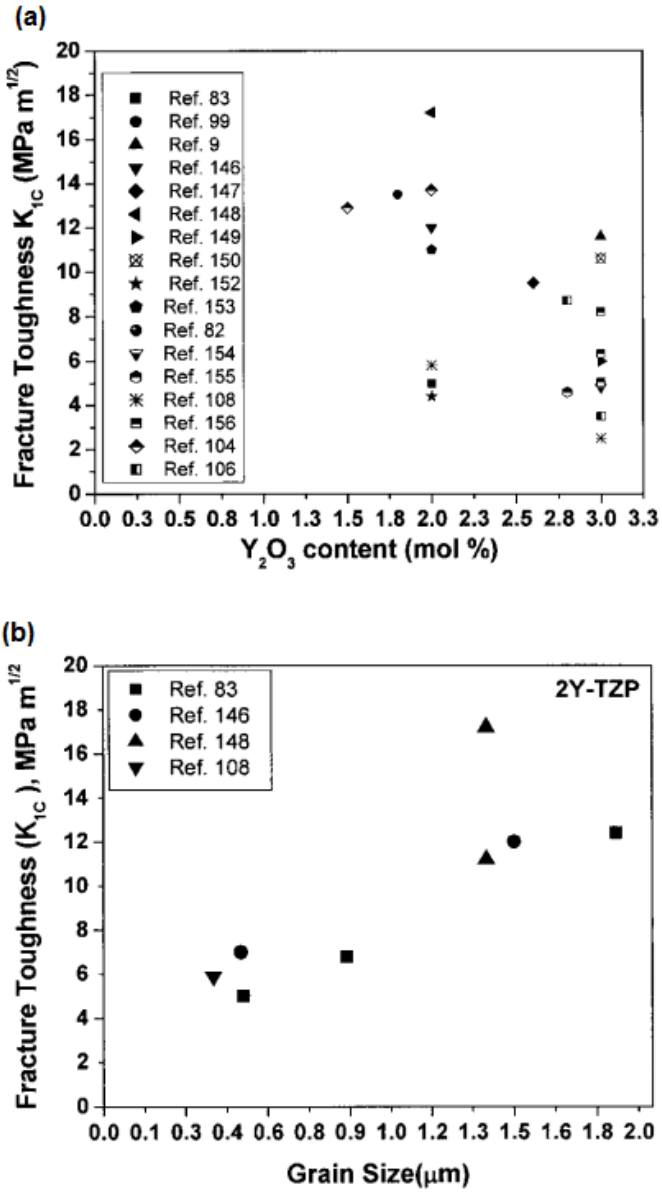


Figure 2.9 – Literature data summary illustrating: (a) fracture toughness versus yttria content and (b) fracture toughness versus grain size of 2Y-TZP [5].

Fracture toughness versus grain size data from the literature is also plotted in Figure 2.9 (b). In general, fracture toughness is observed to increase with grain size. One important observation is that a tremendously high toughness of 17 MPa $m^{1/2}$ (measured by SENB – Single Edge Notch Bending ) was obtained with 2Y-TZP of grain size 1.4 µm .

Table 2.4 shows the typical values of the mechanical/physical properties presented by 2 % mol yttria tetragonal zirconia (2YSZ) produced by INNOVNANO through the EDS method. The powder physical properties are showed as well as the mechanical properties of sintered samples after different stages of pressing, namely, cold isostatic pressing (CIP) and hot isostatic pressing (HIP).

Table 2.4 – Physical/Mechanical properties 2YSZ produced by INNOVNANO (Adapted from [32]).

| **2YSZ produced by INNOVNANO** | | |
|---|---|---|
| **Powder Properties** | | |
| **Primary Particle, $d_{50}$ (nm)** | ~ 50 | |
| **Powder $d_{50}$ (nm)** | < 250 | |
| **Granule $d_{50}$ (nm)** | ~60 | |
| **Specific Surface Area ($m^2/g$)** | 25 ± 3 | |
| **Physical/ Mechanical properties** | **CIP** | **HIP** |
| **Grain Size (nm)** | < 250 | < 250 |
| **Density ($g/cm^3$)** | 6.02 | 6.07 |
| **Hardness (HV10)** | 1250 | 1350 |
| **Biaxial Flexural Strength (MPa)** | 1200 | 1600 |
| **Fracture Toughness HV10 ($MPa.m^{0.5}$)** | 14 | 14 |

These powders produce high quality performance ceramics since EDS production allows to obtain ceramic powders with high chemical purity, high specific surface area and an uniform granular morphology. In fact, this allows to achieve full density at lower sintering temperatures (currently 100-150 °C lower than the ones used for conventional powders) resulting in reduced grain growth and combining high fracture toughness (~14 MPa.m0.5) with biaxial flexural strength (1200-1600 MPa), as it can be seen from Figure 2.10. It is important to refer that 3 mol% yttria-stabilized zirconia (3YSZ) has been widely used in

structural ceramic applications during many years. Although, 2 mol % YSZ (2YSZ) offers all the desired properties of 3YSZ, as well as the added benefit of better fracture toughness that is inherent in lower-yttria-content zirconia ceramics. INNOVNANO produces 2YSZ powders that result in ceramics that maintain good flexural strength and ageing resistance being a promising alternative for structural ceramic applications [33].

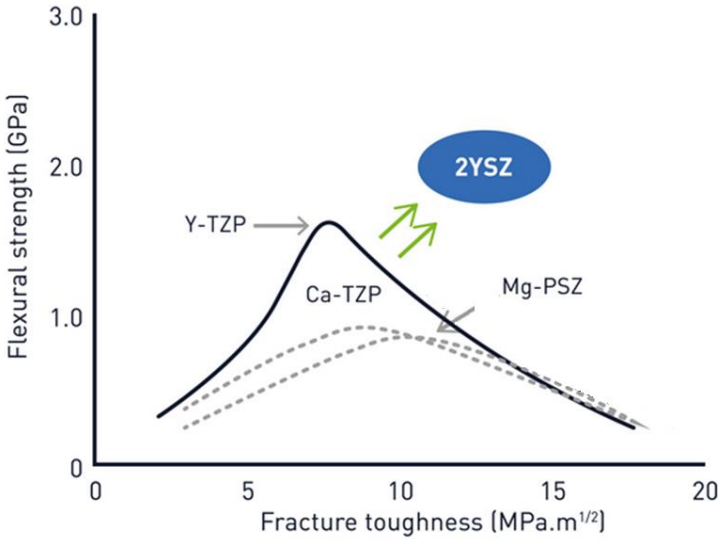


Figure 2.10 - Strength vs toughness curves for different zirconia compositions [34,35].

### 2.3.3. Iron oxide doping YSZ

Coloured zirconia can be obtained by small additions of various metal oxides to the starting powder [9]. Many metal oxides have been use to pigment zirconia, among them $Fe_2O_3$ was considered as having minor adverse effects on the mechanical properties of zirconia [10]. The effect of doping with these oxides in optical properties specifically in the colour and in mechanical properties of yttria stabilized zirconia are discussed in the next topic.

According to Guo and Xiao study [12], $Fe^{3+}$ ion is able to give colour to the solid materials from yellow through dark brown, depending on the concentration and dispersion of $Fe^{3+}$ ion (Figure 2.11). In this work, different contents of dopant were added: 0, 0.5, 1.0 and 1.5 mol % to 3YSZ and 8YSZ.

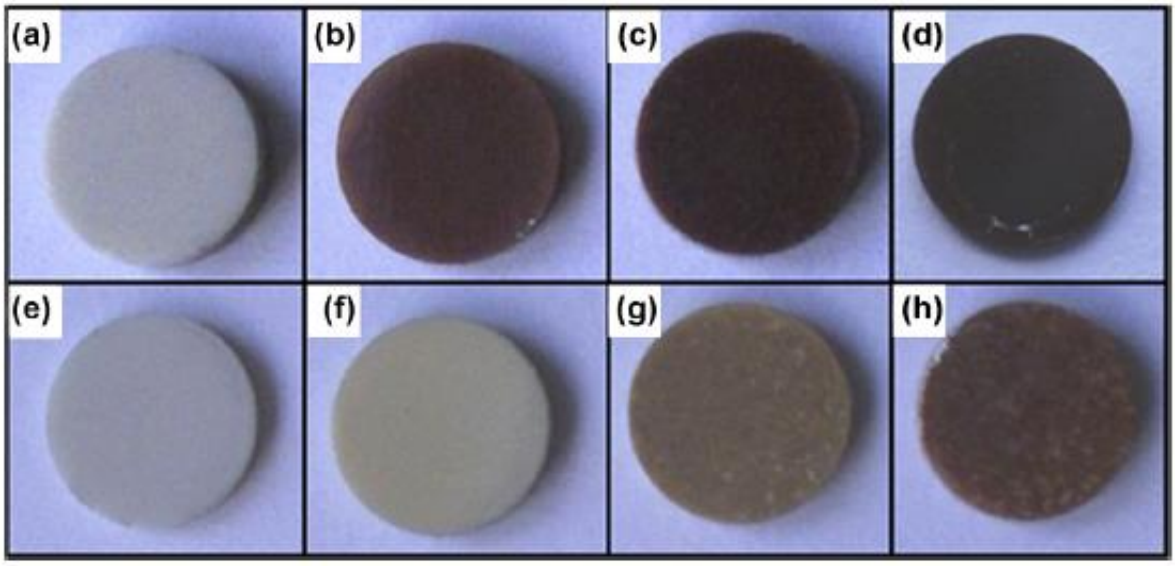


Figure 2.11 - Photographs of $Fe_2O_3$ doped 3YSZ samples sintered at 1400-1500 ºC for 2h: (a) 0 mol %, (b) 0.5 mol %, (c) 1.0 mol %, (d) 1.5 mol % and $Fe_2O_3$ doped 8YSZ samples sintered at 1400-1500 ºC for 2h (e) 0 mol %, (f) 0.5 mol %, (g) 1.0 mol %, (h) 1.5 mol % [12].

Depending on the content of $Fe_2O_3$, the colour of 3YSZ samples ranges from white, Figure 2.11 (a), to black colour, Figure 2.11 (d). According to the authors, the colour is darker with an increase in $Fe_2O_3$ content, suggesting that $Fe^{3+}$ ion started to segregate at grain boundaries of the 3YSZ.

On the other hand, doped 8YSZ samples show lighter colours Figure 2.11 (e), (f) and (d) compared with the $Fe_2O_3$ doped 3YSZ samples within an equal doping oxide content. The colour of 8YSZ samples changed from white to moderate yellowish brown with an increase in $Fe_2O_3$ content. Therefore, the visible colour difference between 3YSZ and 8YSZ can be attributed to different distribution of $Fe^{3+}$ ions in the host crystal lattice.

According to previous studies, the position of $Fe^{3+}$ in YSZ lattice is still an open question. However, Karas *et al.* [12] observed that the unit cell volume slightly increased for 0.5 mol% iron doped 3YSZ compared with undoped 3YSZ. For higher iron concentrations (1.0-2.0 mol%) the unit cell volume decreased again. They suggested that up to 0.5 mol % $Fe^{3+}$ can interstitially dissolve into zirconia lattice, since the $Zr^{4+}$ substitution by undersized dopants ($Fe^{3+}$) led to decreased in the unit cell volume. They concluded that the occupied position by $Fe^{3+}$ ion in the YSZ lattice is dependent on phase nature and oxygen vacancy concentration at room temperature [12]. In the study of Boutz *et al.* [11], the unit cell volume

increased slightly when adding 0.6 mol % of $Fe_2O_3$ and they also concluded that the incorporation of $Fe^{3+}$ ions indicates an interstitial rather than a substitutional mechanism.

Guo and Xiao [12] also investigated the position of $Fe^{3+}$ in the YSZ lattice. They considered that the samples under study are within the range of $Fe_2O_3$ solubility limit at 1150ºC (1.5 % mol) and no experimental details were given by the authors. The $Fe^{3+}$ (0.55-0.78 Å) radius is smaller than that of $Zr^{4+}$ (0.84 Å), $Y^{3+}$ (1.019 Å) and $O^{2-}$ (1.38 Å) radius. This indicates that introduction of $Fe^{3+}$ ions into 3YSZ further distort the crystalline structure. They suggested two types of sites for $Fe^{3+}$ in the zirconia lattice, represented by two defect reactions in Kröger-Vink notation (Equation 2.3 and 2.4). In the case of substitution, the following equation described the mechanism:

$$Fe_2O_3 \xrightarrow{ZrO_2} 2Fe'_{Zr} + V_O^{\bullet\bullet} + 3O_o^x \qquad \textbf{(Equation 2.3)}$$

where $Fe'_{Zr}$ indicates an *Fe* atom occupying a *Zr* lattice site, $O_o^x$ represents an oxygen atom occupying a normal lattice site and $V_o^{\cdot\cdot}$ expresses a vacancy at an oxygen lattice site. As in the $Y^{3+}$ substitution in $ZrO_2$, this reaction generates oxygen vacancies ($V_o^{\cdot\cdot}$) to preserve the electron neutrality of zirconia lattice.

In the case of $Fe^{3+}$ occupying a lattice interstitial site, the equation below represents the doping effect:

$$2Fe_2O_3 \xrightarrow{ZrO_2} 3Fe'_{Zr} + Fe_i^{\bullet\bullet\bullet} + 6O_o^x \qquad \textbf{(Equation 2.4)}$$

where $Fe_i^{\bullet\bullet\bullet}$ indicates a *Fe* atom occupying an interstitial site. Equation 2.4 shows that *2x* mol of $Fe_2O_3$ doping can generate *3x* mol of $Fe^{3+}$ substituents and *1x* mol of $Fe^{3+}$ interstitials, without generating oxygen vacancies.

According to this study, the unit cell volume is determined by $Fe^{3+}$ ion occupation type in YSZ lattice. As mentioned before in the case of $Fe^{3+}$ substitution, the unit cell decreased whereas the $Fe^{3+}$ interstitials give rise to an increase in the unit cell volume [12]. An increase in oxygen vacancy concentration increases disorder in the $ZrO_2$-$Y_2O_3$ system and so increases the stability of the tetragonal phase [5].

S.V. Bechta *et al.* [36] have constructed a pseudobinary phase diagram of the $ZrO_2$-FeO system in an inert atmosphere. According to this study, the FeO solid-solution in $ZrO_2$ have been determined as follow: t-$ZrO_2$ (FeO) exists in the temperature range from 1172 to 2347 ºC; the FeO solubility in t-$ZrO_2$ is 2.2 ± 0.3 mol % at 1332 ºC; c-$ZrO_2$ exists in the

temperature of 1800 ºC (or less) up to 2710 ºC; the solubility limit of FeO in $ZrO_2$ at 1800 ºC is about 13 mol % FeO, as it can be seen from Figure 2.12.

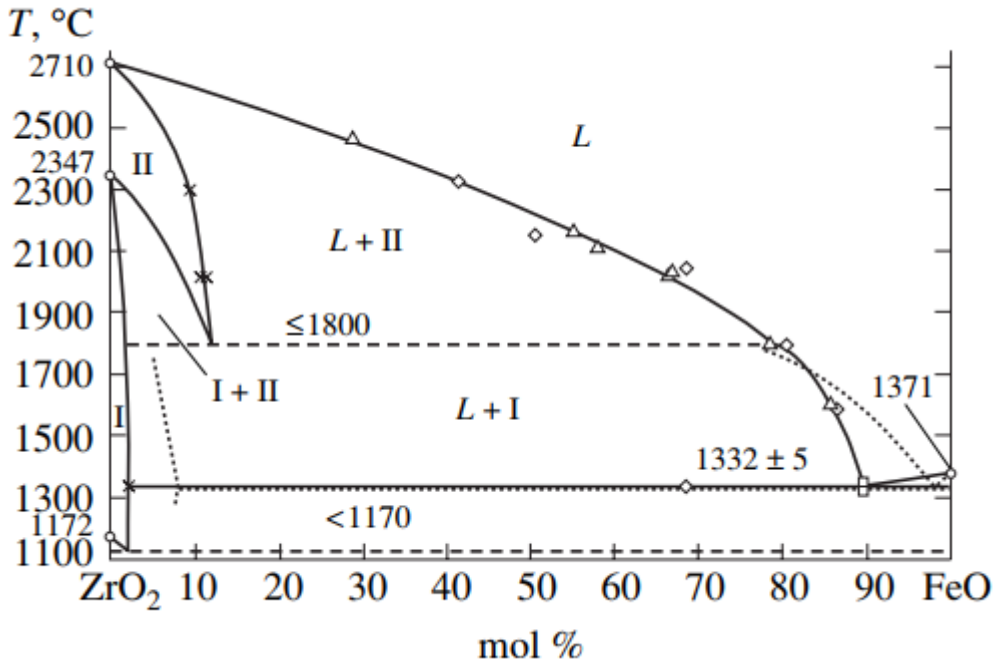


Figure 2.12 – Phase diagram of the $ZrO_2$-FeO system. I and II denote t-$ZrO_2$ (FeO) Solid-solution (SS) and c-$ZrO_2$ (FeO) SS [36].

Considering this system (since no phase diagram of the $ZrO_2$-$Fe_2O_3$ system was found), the dopant contents used during this work are within the solubility limit at 1350 ºC (~2.2 mol % of $Fe_2O_3$) (see Figure 2.12), which was the sintering temperature in the current investigation. However, it should be noted that this system is different comparatively to the system under the present study ($Y_2O_3$ – $ZrO_2$ – $Fe_2O_3$).

## 2.4. Optical properties of YSZ

There are other mechanisms proposed to modify the YSZ colour, without dopant additions. These mechanisms are associated with crystalline lattice defects as oxygen vacancies, called colour or F centers. A colour center is a type of crystallographic defect in which an anionic vacancy in a crystal is filled by one or more unpaired electrons. These electrons in such a vacancy tend to absorb light in the visible spectrum in such way that the material becomes coloured. In other words, colour centers are defects with energy levels lying within the band gap of the host and having characteristic visible absorption, hence colour as well as luminescence [37].

H. Zhang *et al.* [38] found that the yellowish-brown appearance of c-YSZ is usually attributed to colour centers (oxygen vacancies with trapped electrons) which are easily produced in c-YSZ under thermal reduction and electroreduction conditions. In their investigation, they produced cubic zirconia by Spark Plasma Sintering (SPS) providing the reduction conditions to form the colour centers. Figure 2.13 displays the digital photographs of (a) c-YSZ produced by SPS at 1000 to 1200 ºC for 10 minutes under a pressure of 400 MPa and (b) the same samples after annealing treatment at 900 ºC, during for 4h in air.

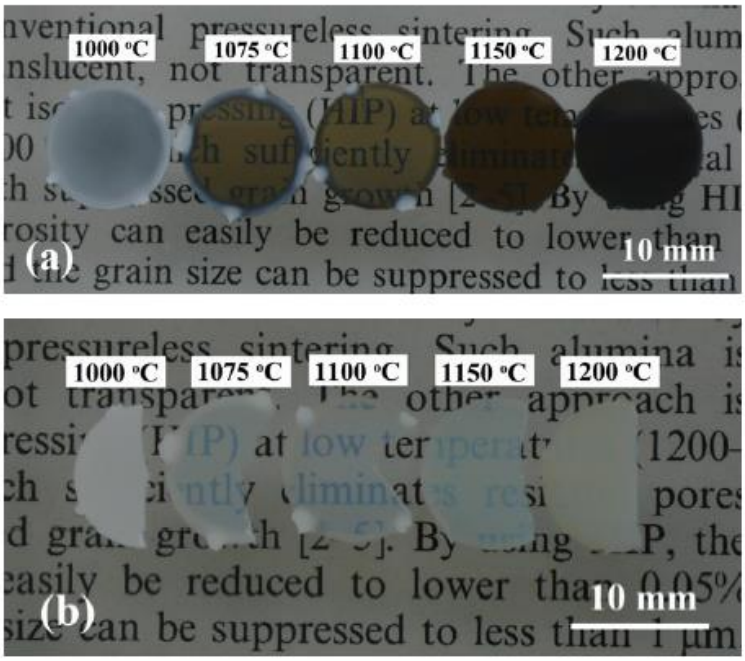


Figure 2.13 – Photographs of (a) YSZ produced by SPS at 1000 to 1200 ºC for 10 minutes under a pressure of 400 MPa and (b) the same samples after annealing treatment in air [38].

The formation of oxygen vacancies in YSZ due to reduction conditions can be expressed as follows:

$$O_o^x = \frac{1}{2}O_2 + V_0^{\bullet\bullet} + 2e^{'} \qquad \textbf{(Equation 2.5)}$$

Indeed, these oxygen vacancies $(V_o^{\bullet\bullet})$ can cause strong light absorption by the association with free electrons to form colour centers. The oxygen vacancies with one trapped electron $(e')$ are called $F^+$ center while the ones with two trapped electrons are F centers, as expressed in Equations 2.6 and 2.7:

$$V_o^{\bullet\bullet} + e' = V_O^{\bullet} \rightarrow (F^{+}) \qquad \textbf{(Equation 2.6)}$$

$$V_O^{\bullet\bullet} + 2e^{'} = V_O^{x} \rightarrow (F) \qquad \textbf{(Equation 2.7)}$$

These colour centers result in strong yellowish colouration. Obviously, the amount of colour centers increases with sintering temperature due to reducing environment resulting in darker samples. On the other hand, annealing in oxidizing atmosphere can diffuse oxygen and decrease colour centers. Hence, as it can be seen, upon annealing the sample colour turns into white (Figure 2.13 (b)) [38].

# CHAPTER 3

## 3. Experimental Procedure

## 3.1. Experimental Procedure

This chapter describes the detailed experimental procedure performed as well as the characterization techniques used in this work. Therefore, it mainly focuses on two aspects: sample preparation and sample characterization (reference material, spray-dried powders and sintered samples) (Figure 3.1). First of all, the reference material was characterized in order to investigate its optical and structural properties to compare to the samples prepared in the present study. After that, samples were produced starting with commercialized powder 2YSZ (2 % mol yttria-stabilized zirconia) produced by INNOVNANO doped with different α-$Fe_2O_3$ contents: 0, 0.1, 0.2 and 0.4 wt %. The characterization is divided into three parts: reference material characterization, spray-dried powders and sintered samples characterization, as summarized in Figure 3.1.

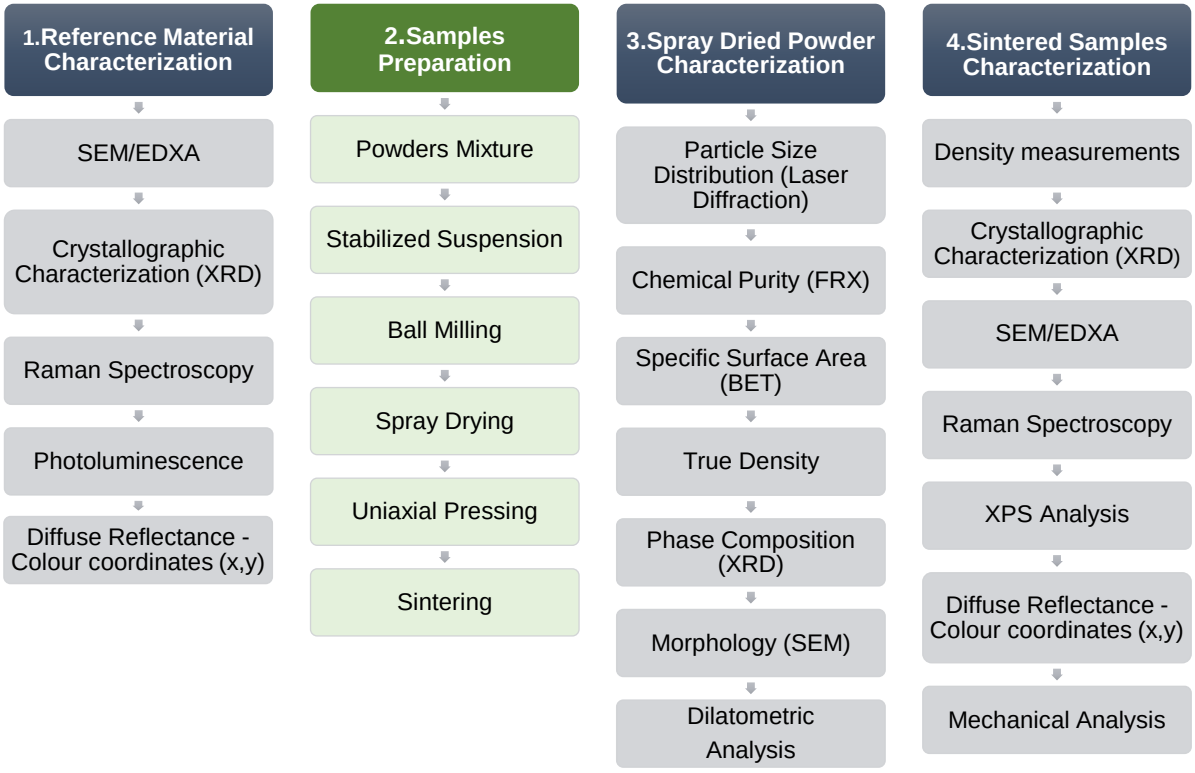


Figure 3.1 - Scheme of the experimental procedure: reference material characterization, powders and sintered samples production and characterization.

Firstly, the structural characterization of the reference sample was assessed using Raman Spectroscopy and X-ray diffraction (XRD). Scanning Electron Microscopy (SEM) was also performed to analyse the microstructure of the samples and Energy Dispersive X-ray Analysis (EDXA) to evaluate the elemental composition.

The photoluminescence (PL) properties of the reference material were investigated. Besides PL study, the diffusive reflectance was also measured and the colours coordinates were determined.

In order to produce samples with similar colour to the reference material and with the desired mechanical properties, several steps were performed starting with 2YSZ doped with iron oxide (α-$Fe_2O_3$): powders mixture, suspension ball milling, spray drying process, uniaxial pressing and sintering.

The particle size distribution of the particles in suspension and of the spray dried powders was determined by laser diffraction. The chemical purity of the spray dried powders was evaluated by X-ray Fluorescence (XFR) while the specific surface area (SSA) was determined using the BET (Brunauer – Emmet – Teller) isotherm method and the true density of the particles was measured by Helium Pycnometry. The morphology and particle size of 2YSZ powder was analysed by SEM while the structural analyses/phase composition was carried out by XRD.

The green density of the samples was determined geometrically while the density of the sintered samples was measured based on Archimedes' principle. The samples surface was polished and thermally etched for SEM observation.

The structural analysis of sintered samples was carried out by XRD and Raman Spectroscopy in order to identify the crystalline phases nature (monoclinic or tetragonal phase in $Fe_2O_3$ doped YSZ). The chemical defect introduced via doping can affect the colour of 'parent materials' and the colours coordinates (x and y) were determined by Diffuse Reflectance. In addition, a XPS (X-ray Photoelectron Spectroscopy) analysis was performed with the purpose of investigating the oxidation state of Fe ions.

Polished samples were used to determine the Vickers hardness (HV10) and fracture toughness ($K_{Ic}$) using Vickers indentation method. The biaxial flexural strength was also determined.

## 3.2. Optical Characterization of reference/sintered samples

As mentioned before, the reference material was characterized from the optical point of view. The study of the luminescence spectroscopy is essential to understand the excitation and emission mechanisms, providing information about the electronic structure and

presence of defects in the material. Simultaneously, the diffuse reflectance was also evaluated and the colour coordinates were determined. This part is dedicated to a brief description of each technique.

### 3.2.1. Photoluminescence

Photoluminescence (PL) spectroscopy is a technique used for the investigation of the electronic structure of semiconducting and semi-insulating materials. It is helpful in the determination of impurity concentrations, identifying defects and measuring the band gap of semiconductors. Zirconia is considered a wide band gap semiconductor, with reported band gap (Eg) energies between 4-6 eV, depending on crystalline phase nature [22] .

When a sample is excited by light with an energy higher than the band gap, an excess of electron-hole pairs is created. These can recombine through various recombination paths available, some emitting a photon of energy, *hv*. If this return process is radiative, it emits a photon whose energy gives the difference between the excited and the initial state energies (Figure 3.2).

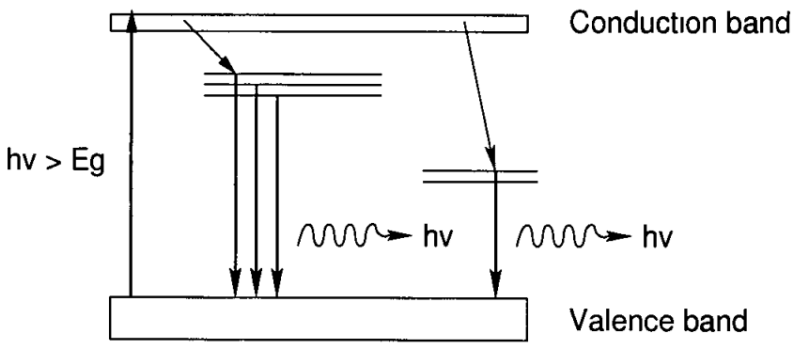


Figure 3.2 - Schematic representation of photon energy (*hv*) emitted by excitation [27].

The emission spectrum shows a fingerprint peak related to the energy of each excited level providing an intensity versus wavelength spectra [39]. For a given excitation energy, it provides information about the optically active defects in a sample, allowing the identification of the electronic energy levels involved in the recombination process. The latter can be related either with band to band recombination, band to defect recombination or even intra-defect transitions [22].

The sample is excited with an excitation source, followed by a monochromator (the excitation monochromator).The emitted light is collected by a focusing lens and analysed by means of a second monochromator (the emission monochromator), followed by a suitable detector connected to a computer, as it can be seen from Figure 3.3 [40].

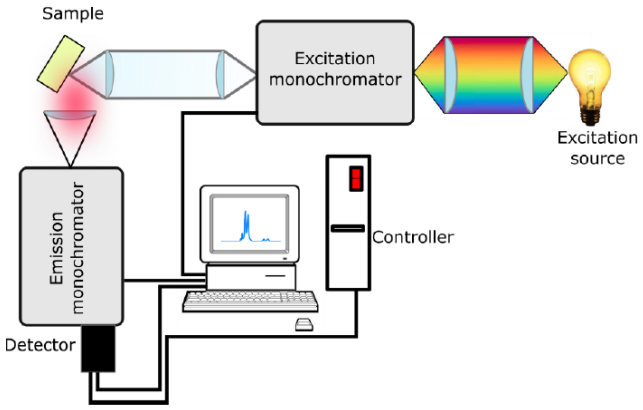


Figure 3.3 – Main system components for measuring PL emission spectra [22].

In this work, a SPEX 1074 emission monochromator to disperse the emitted light and a cooled Hamamatsu R928 photomultiplier detector were used in the acquisition of the reference material PL spectra under 325 nm wavelength (UV) laser excitation source. This system is also equipped with a cold finger of a closed cycle helium cryostat that allows to decrease the sample temperature up to ~14 K which allows to perform the temperature dependence photoluminescence measurements (between 14 K and RT).

In addition, PL spectra of the reference sample and the sintered samples were also recorded on Horiba Jobin Yvon HR800 Raman spectrometer under 442 nm wavelength laser excitation source.

### 3.2.2. Diffuse Reflectance Spectrophotometry and Colour

Colour is the human eye's perception of reflected radiation in the visible region of the electromagnetic spectrum (400–700 nm). Hence, colour can be measured by diffuse reflectance spectrophotometry. Light reflected from the material is collected in an integrating sphere which is fundamentally a hollow sphere coated inside by a white material, highly reflective and diffusive which function is to spatially integrate a radiant flux. When the sample being analysed is placed inside the sphere and connected, the luminous flux

illuminates the inner surface through multiple diffuse reflections as shown in Figure 3.4. [41, 42].

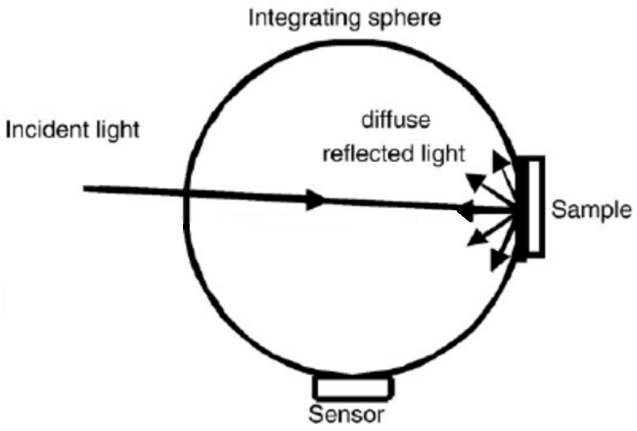


Figure 3.4 - Multiple reflections inside an integrating sphere [43].

In 1931, the CIE- Commission Internationale d'Eclairage - established standards for a series of colour spaces that represent the visible spectrum which are known as tristimulus values (XYZ), based on the visual capabilities of a standard observe. The CIE conducted colour-matching tests on a number of subjects, then used the collective results creating "colour-matching functions" and a "universal colour space" that represents the average human's range of visible colours. The colour matching functions are the values of each primary light (red, green and blue) that must be present in order to the average human visual system will differentiate clearly all the colours of the visible spectrum (Figure 3.5) [44].

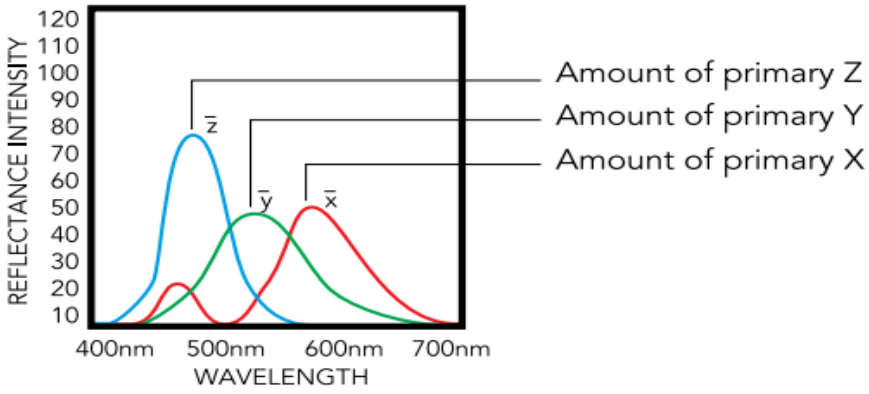


Figure 3.5 - Reflectance intensity as a function of wavelength.

According to CIE 1931 method, tristimulus values result from the colour reflectance spectra as follows [42] :

$$X = K\sum S(\lambda)x(\lambda)R(\lambda) \quad \textbf{(Equation 3.1)}$$

$$Y = K\sum S(\lambda)y(\lambda)R(\lambda) \quad \textbf{(Equation. 3.2)}$$

$$Z = K\sum S(\lambda)z(\lambda)R(\lambda) \quad \textbf{(Equation. 3.3)}$$

$$K = 100/\sum S(\lambda)y(\lambda) \quad \textbf{(Equation. 3.4)}$$

where λ is the wavelength; S(λ) is the relative power distribution of the illuminant; x(λ), y(λ) and z(λ) are colour matching functions and R(λ) is the reflectance spectra of a given sample. The chromaticity of a colour is then specified by the two derived parameters x and y, two of the three normalized values being functions of all three tristimulus values X, Y, and Z [42]:

$$x = \frac{X}{(X+Y+Z)} \quad \textbf{(Equation. 3.5)}$$

$$y = \frac{Y}{(X+Y+Z)} \quad \textbf{(Equation. 3.6)}$$

$$z = \frac{Z}{(X+Y+Z)} = 1-x-y \quad \textbf{(Equation. 3.7)}$$

Indeed, these coordinates (x,y) are used to form the chromaticity diagram showed in Figure 3.6.

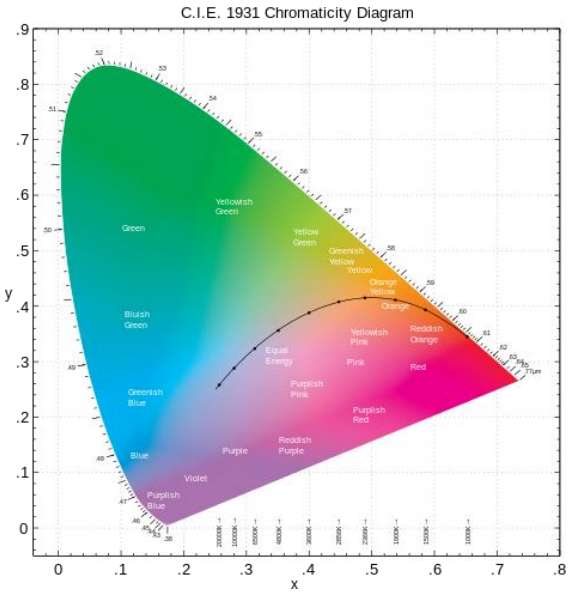


Figure 3.6 - The CIE 1931 colour space chromaticity diagram [45].

In this work, diffuse reflectance measurements were made by using a tungsten light source, an ocean optics spectrophotometer equipped with integrating sphere capable of collecting the reflected light. The reference material and the produced samples spectra were calibrated with the measurement of lamp intensity (100% reflection) and the dark (0% reflection) over the entire wavelength spectrum of visible light (400-700 nm). The spectra were recorded using the *SpectraSuits* software. The tristimulus values (XYZ) were obtained by the reflectance data and therefore the colour coordinates (x,y) using *Matlab* software.

## 3.3. Structural Characterization of reference/sintered samples

The structural analyses of the reference material and of the produced samples was carried out by X-ray diffraction (XRD) and Raman spectroscopy techniques

### 3.3.1. X-ray Diffraction

X-ray diffraction is one of the most powerful and widely used techniques for identification the crystalline phases of a material. When X-ray interacts with an atom, its electrons become a secondary source of the electromagnetic waves with the wavelength *(λ)* of the incident radiation. Therefore, each atom in the periodic array (crystalline material) scatter the electromagnetic waves in all directions. Only the planes described by the Miller indexes

(*hkl*) oriented in the respect to the incident beam will interfere constructively giving rise to an intensity maximum (diffraction spot). This interference is only constructively if the Bragg's law is followed [46] (Equation 3.8):

$$n\lambda = 2d\sin\theta \qquad \textbf{(Equation 3.8)}$$

in which $\lambda$ (Å) is the wavelength of the incident radiation, *d (Å)* is the interplanar distance and $\Theta$ is the angle between the incident beam and the diffraction planes from the crystal lattice and *n* is the diffraction order, which is an integer multiple. Hence, by scanning the diffraction angle, the diffractogram collected by the diffraction maxima associated to each crystalline plane in the crystal can be made. As each material has a unique arrangement and number of atoms, its diffraction pattern is also unique which allows the identification of crystalline phases present in a material [46].

In this work, XRD technique was used to identify the crystalline phases present in the reference material, in the spray dried powders as well as in the produced samples. It must considerer that either the reference or the sintered samples were analysed in bulk in order to avoid phase transformation due to mechanical stresses.

In this work, the measurements were performed in a Bruker D8 Advance X-ray diffractometer system at room temperature on Bragg-Brentano configuration, using the $K_\alpha$ emission line of Cu with 1.54056 Å wavelength. All diffractograms were obtained in the same conditions: 2θ ranging from 5 º to 20 º, with a scan size of 0.01 º, a time per step of 0.9 s and a rotation of 30 rpm

The identification of the crystalline phases using the diffractograms obtained by X-ray diffraction was performed by matching reference diffractograms registered in the International Centre for Diffraction Data (ICDD - PDF card no 00-037-1484 and no 00-050-1089). The XRD patterns were refined by Rietveld method using *TOPA's* software in order to determine the lattice parameters of the unit cell and the weight fraction of each phase.

### 3.3.2. Raman Spectroscopy

Raman spectroscopy is an optical technique based on the phenomenon of inelastic scattering, providing information about the vibrational modes of atoms in a crystalline lattice. Therefore, it can be used to obtain the chemical and structural information about the sample being analysed, since the Raman spectrum is a fingerprint of each substance [47].

In Raman spectroscopy, the sample is illuminated with a monochromatic laser beam that interacts with the molecules of the sample and originates a scattered light. This scattered light, having a different frequency from that of incident light, is used to construct a Raman spectrum since the difference between the frequencies of the incident radiation and the inelastic scattered light corresponds to the energy of the normal vibrational modes of the crystalline lattice [22].

A considerable fraction of this scattered radiation has a frequency equal to the frequency of incident radiation and it is designated by Rayleigh scattering. Only a small fraction of the scattered radiation has a frequency different from the frequency of incident radiation and constitutes the Raman scattering. When the frequency of incident radiation is higher than the frequency of scattered radiation, Stokes lines appear in Raman spectra. On the other hand, when the frequency of incident radiation is lower than the frequency of scattered radiation, anti-Stokes lines appear in Raman spectra as represented in Figure 3.7 [48].

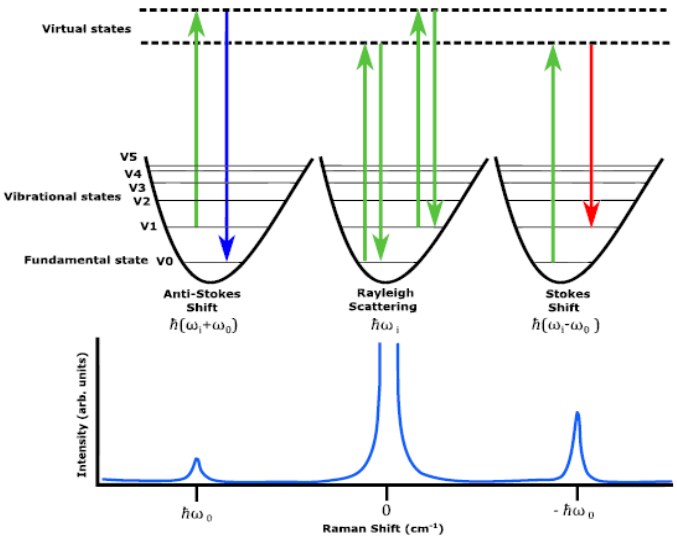


Figure 3.7 - Schematic representation of the phenomena of anti-Stokes shift, Rayleigh scattering and Stokes shift [22].

In contrast to XRD technique, Raman spectroscopy allows to identify and distinguish very clearly the different crystalline phases of zirconia as it is possible to confirm in Figure 3.8, since it is very sensitive to the vibrational modes of zirconia in its different structures [22].

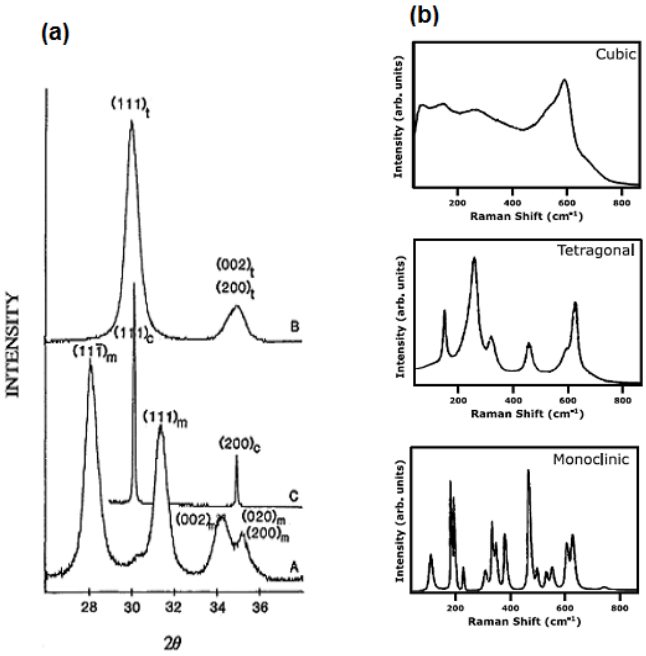


Figure 3.8 - (a) XRD pattern for (A) monoclinic, (B) tetragonal and (C) cubic; (b) Raman spectra of the three allotropes of zirconia [22].

In this work, the spectrometer used was the Jobin Yvon (HORIBA) HR800 that operated on backscattering configuration. The reference material and the produced samples were evaluated from the structural point of view by this technique. The laser 442nm wavelength was used as the excitation source. During the analysis, the laser was focused on the sample to a spot size of ~2 μm using a 100x objective lens.

The main components of the Raman spectrometer are: excitation source (laser), optical components (including filters, lenses, mirrors and beam splitter), microscope, grating and a detector as it can be seen from Figure 3.9. It is important to refer that light with different wavelengths has different penetration depths on the material and, consequently, it is possible to study the material at different penetration depths [22]. In the case of Zirconia, a wavelength of 442 nm has a Raman penetration depth around 0.2 μm [49].

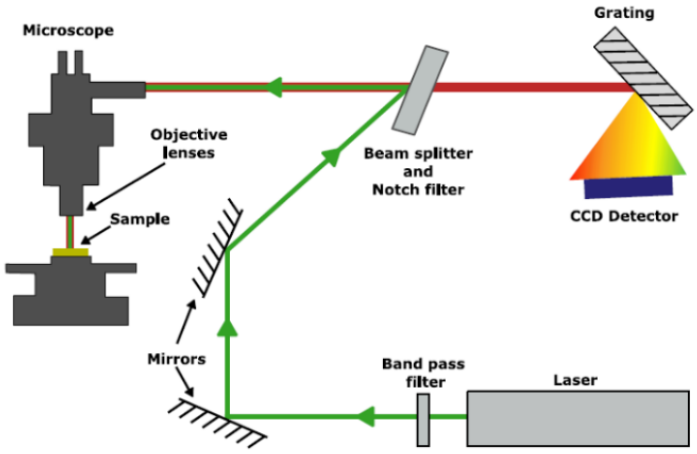


Figure 3.9 - Main components of Raman spectrometer in backscattering configuration [22].

## 3.4. Sample Preparation

In order to prepare samples with similar colour to the reference material and with the specified mechanical properties, several steps were performed. This part is dedicated to a brief description of sample preparation procedure and therefore the characterization techniques used.

### 3.4.1. Materials

In this work, two materials were used: 2 mol % Yttria Stabilized Zirconia (2YSZ) commercialized powders produced by EDS with $d_{50}$ (mean value of the particle size distribution) of single particle size close to 50 nm, mixed with different amounts (0, 0.1, 0.2 and 0.4 wt %) of iron oxide ($\alpha$-$Fe_2O_3$ - Iron oxide III, Sigma Aldrich, 99.99 %) as dopant, aiming to colour the 2YSZ. The established compositions are presented in Table 3.1. In order to deagglomerate the suspension, Dolapix CE 64 was used as a dispersing agent/deflocculant.

Table 3.1 - Established compositions.

| Material | Dopant | Dopant Content (wt. %) |
|---|---|---|
| **2YSZ produced by INNOVNANO** | None | 0 |
| | $Fe_2O_3$ | 0.1 |
| | | 0.2 |
| | | 0.4 |

### 3.4.2. Suspensions Preparation

The content of each powder (2YSZ and $Fe_2O_3$) was weighed on a precision lab scale balance (± 0.1 mg) regarding the preparation of the right amount of each material according with the preliminary established compositions (see Table 3.1). Distilled water was added to the powders to achieve the right composition as also as Dolapix CE 64 as deflocculant agent. The suspensions were milled on a nano bead mill (bead size <1µm), Dispermat® - SL 12 at 3500 rpm for ~15 minutes each. During this process, a high flow circulation was attained with an independent pumping system attached to the milling chamber. The dispersed product passes through the mill base separation and is recovered either in a vessel or flows back into the supply vessel (re–circulation method) (Figure 3.10) [50].

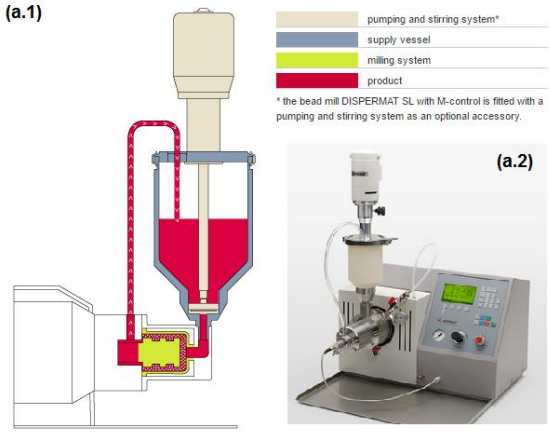


Figure 3.10 - Nano bead mil Dispermat SL12 (a.1) schematic representation of the equipment and (a.2) equipment apparatus available at INNOVNANO.

### 3.4.3. Spray Drying

The suspensions were dried using a laboratorial spray drying, Büchi Mini Spray Dryer B-191 with a 73 µm nozzle and the parameters adjusted for spray drying process are presented in Figure 3.11.

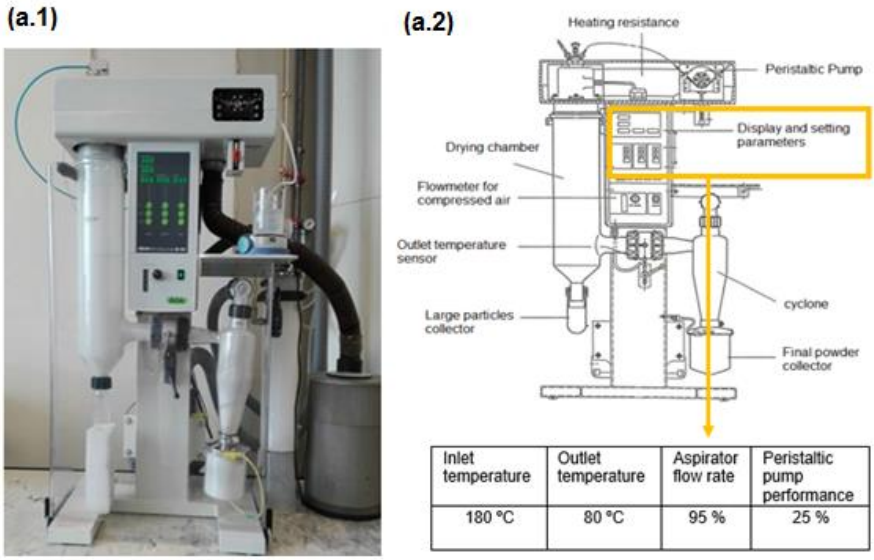


Figure 3.11 - (a.1) Mini Büchi Spray Dryer B-191 available at University of Aveiro and (a.2) schematic representation of the equipment. Yellow arrow indicates the operating parameters used for spray drying process in this work (adapted from [51]).

This technique allows the transformation of feed from a fluid state into dried particulate form by spraying the feed into a hot drying medium [52]. The main controlled operating parameters are the air temperature at the entry (inlet temperature) and at the exit (outlet temperature), the atomizing nozzle design, the air and suspension flow rates (performance of aspirator and peristaltic pump). These parameters were adjusted according to INNOVNANO's conditions, specially, the difference between the inlet and outlet temperature (~100 ºC).

### 3.4.4. Powder Shaping and Sintering

The spray dried powders were pressed uniaxially (~94 MPa) using a hydraulic press Specac's Atlas™ Series Autotouch. A stainless-steel pellet die with 20 mm of diameter was used for compacting powdered samples.

After pressing and before sintering, the compacted green samples were subjected to a dilatometric analysis in order to record their thermal behaviour with the temperature. The

dilatometric analysis was performed on a vertical dilatometer Linseis L-75 Platinum series in air with a heating rate of 5 ºC/min, maximum temperature of 1600 ºC and with a cooling rate of 10 ºC/min.

Dilatometry is a technique in which a dimension of a specimen under negligible load (0.1 N) is measured (e.g. expansion or shrinkage measurement) as a function of temperature, while the sample is subjected to a controlled temperature cycle in a specified atmosphere. An accurate understanding of this behaviour can provide insights of sintering conditions. A curve of the linear shrinkage ($L$-$L_o/L_o$, where $L$ is the final length and $L_o$ the initial length) against temperature or time is recorded.

According to the dilatometric analysis and INNOVNANO's sintering conditions, the sintering cycle was defined. The sintering was performed in air on an electric furnace (Termolab MFL032) with a heating rate of 2 ºC/min, maximum temperature of 1350 ºC, 2 hours of dwell time and a cooling rate of 5 ºC/min (see Figure 3.12). In this work, all samples were sintered in the same furnace at the same conditions.

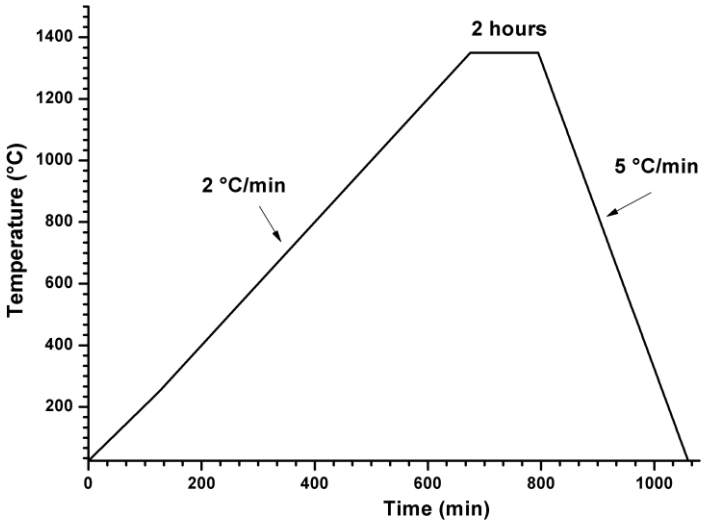


Figure 3.12 – Defined sintering cycle.

## 3.5. Powder Characterization Techniques

In order to fully characterize the spray dried powders, several techniques were assessed. This part is dedicated to a brief description of each one.

### 3.5.1. Particle Size Distribution

Laser diffraction measures the particle size distribution by determining the angular variation in intensity of the light scattered when a laser beam passes through a dispersed particulate sample. Large particles scatter the light at small angles relative to the laser beam and small particles scatter light at large angles. The angular scattering intensity data is then analysed to calculate the size of the particles responsible for creating the scattering pattern [53].

In this work, the particle size distribution of the particles in suspension and of spray dried powders was measured by Laser Diffraction using a Mastersize Malvern 2000.

### 3.5.2. X-ray Fluorescence

The spray dried powders were submitted to X-ray fluorescence analysis to evaluate the chemical purity. XRF spectrometry is an elemental analysis technique with wide-ranging application in science and industry. It is based on the principle that individual atoms, when excited by an external energy source, emit X-ray photons of a characteristic energy or wavelength which are detected by a specific detector. By counting the number of photons of each energy emitted from a sample, the elements present may be identified and quantified [54].

In this work, the chemical composition of the spray dried powders was evaluated by a Bruker-ACS S4 Pioneer X-ray Fluorescence Spectrometer with a rhodium X-ray source. The powders were firstly uniaxial pressed using the Hydraulic Press (25 tons) using a stainless-steel press die with 40 mm of diameter. Wax was added on the right proportion (1g wax for 10 g of powder) and one of compacted powder surface was covered with boric acid.

### 3.5.3. Specific Surface Area

The specific surface area (SSA) ($m^2/g$) of the spray dried powders produced was evaluated by BET isotherm (Brunauer, Emmett and Teller) method. It is determined by the physical adsorption of a gas on the surface of the solid and by calculating the amount of adsorbed gas corresponding to the formation of a monomolecular layer on the surface. This physical adsorption results from relatively weak forces (van der Waals forces) between the adsorbed gas molecules and the adsorbent surface area of the powder. In order to determine the SSA, the equation 3.9 was applied:

$$\frac{P}{V(P_0 - P)} = \frac{1}{V'C} + \left(\frac{C-1}{V'C}\right) \times \left(\frac{P}{P_0}\right) \qquad \textbf{(Equation 3.9)}$$

where $P$ is the equilibrium pressure and $P_0$ the saturation pressure of the gas at the temperature of adsorption, $V$ corresponds to the adsorbed gas volume, $C$ is the BET constant, $V'$ is the volume of an absorbed gas monolayer.

The determination of SSA was carried out using the multipoint Brunauer-Emmett-Tellerum (BET) isotherm in a Quantachrome Nova 1000e Series System, equipped with *NovaWin* software, and the adsorbed gas was nitrogen ($N_2$), available at INNOVNANO.

### 3.5.4. Density Measurements

Gas pycnometry is a technique used to measure the true density of particles in a powder. A sample of known mass is placed in one of two chambers of known volume, maintained at a constant temperature. Helium is then added to the system due its inertness and high diffusivity penetrating the finest pores. The true density (g/cm$^3$) of the spray dried powders was determined in vacuum, using helium (He) as measurement gas with a Micrometrics - AccuPyc II 1340 pycnometer, available at INNOVNANO.

The geometric apparent density (g/cm$^3$) of the green samples after uniaxial pressing was geometrically determined using the following equation:

$$\rho_g = \frac{m}{v} = \frac{m}{\pi\left(\frac{d}{2}\right)^2 \times h} \qquad \textbf{(Equation 3.10)}$$

where $m$ is the mass in grams, $d$ *is* the diameter in cm, and $h$ is the height in cm of the samples pressed uniaxially (~94 MPa). In this work, the final apparent green density was achieved by measured three green samples.

The apparent density (g/cm$^3$) of the samples after sintering was estimated based on Archimede's principle, using the following equation:

$$\rho = \frac{m_d}{m_s - m_i} \times \rho_{liq} \quad \textbf{(Equation 3.11)}$$

where $m_d$ is the dried sample mass, $m_s$ is soaked sample mass, $m_i$ is the immersed sample mass and $\rho_{liq}$ is the density of the immersion liquid (distilled water - 1 g/cm$^3$). The final value was calculated by measuring ten different sintered samples and the average value was considered as the final density.

The theoretical density ($\rho_{th}$) of the tetragonal structure was determined using the lattice parameters obtained by Rietveld refinement and it was given by:

$$\rho_{th} = \frac{nA}{V_c N_A} \quad \textbf{(Equation 3.12)}$$

where $n$ is the number of formula units per unit cell (for tetragonal zirconia n=2), $A$ is the atomic weight, $V_c$ is the volume of the unit cell and $N_A$ is Avogadro's number (6.022 x 10$^{23}$ atoms /mol). The theoretical density of monoclinic phase considered was a constant value of 5.817 g/cm$^3$ while the theoretical density of the tetragonal phase was estimated through Equation 3.12. As 2YSZ is a multiphase material, the mixture rule was applied to determine its density:

$$\frac{1}{\rho_{th}} = \frac{w_m}{\rho_m} + \frac{w_t}{\rho_t} \quad \textbf{(Equation 3.13)}$$

where $w_m$ and $\rho_m$ are the weight fraction and the theoretical density of monoclinic phase, respectively, whereas, the $w_t$ and $\rho_t$ are the weigh fraction and the theoretical density of tetragonal phase. The weigh fraction of each phase was estimated based on XRD Rietveld Refinement.

## 3.6. Microstructural/ Compositional Characterization of reference/sintered samples

### 3.6.1. Scanning Electron Microscopy and Energy Dispersive X-ray Spectroscopy

Electron microscopy is a very powerful and versatile tool available for the microstructural, morphological and chemical composition characterization. It produces images of a sample by scanning the surface with a focused beam of electrons. From the interaction between the material and the electron beam, a higher number of different signals are generated (Figure 3.13).

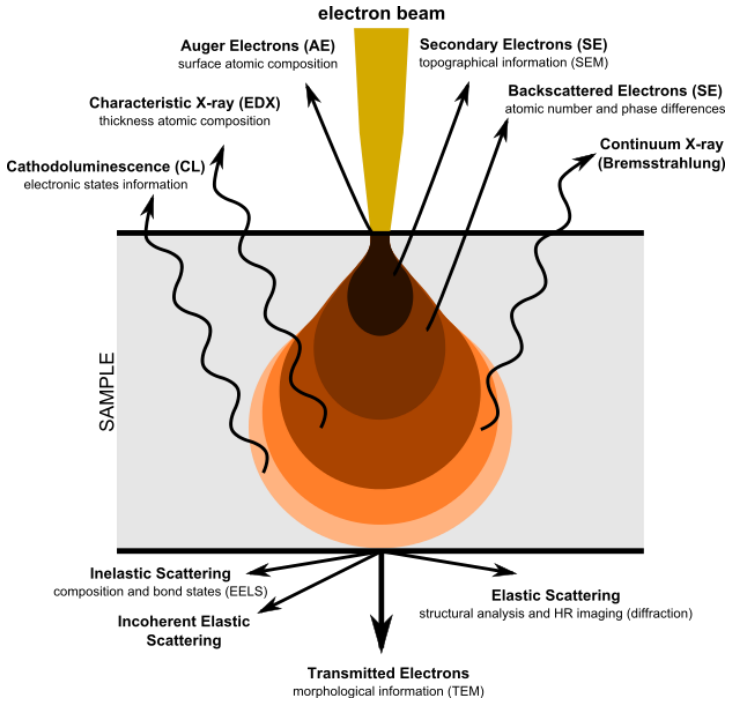


Figure 3.13 - Different signals generated from the interaction of the electron beam and the sample [22].

Each one of these signals can give different type of information: chemical composition, surface topography, crystallography, atomic number distribution and others. Electron image can be combined with other characterization techniques in order to get more information from a specific and localized region of the sample. In fact, energy dispersive X-ray analysis (EDXA) is typically related with electron microscopy regarding the identification of specific chemical elements in the sample by the analysis of the emitted X-ray radiation [22]. This technique is very useful to investigate the distribution of specific element by mapping a region of the sample [55]. In this work, EDXA-map were used to try to understand the dopant distribution on the zirconia matrix.

Two SEM equipments were used: S4100 Hitachi and a Hitachi SU-70, with an acceleration voltage of 15 kV and 25 kV. For such analysis, due to zirconia insulator character, it was essential to deposit a thin carbon film on the surface of the sample in order to avoid charge effect. For that, the produced samples were placed on an aluminium sample holder, with carbon tape and then, as said before, covered with a carbon thin film, on a EMITECH K950 carbon sputter equipment in vacuum (9 $x10^{-3}$ mbar). The same procedure was made to observe the reference material. The spray dried powders were also covered with gold-palladium for such analysis.

For SEM observation, and before carbon deposition, it was necessary to polish the samples surface. The polishing procedure performed to achieve the desired surface finishing is presented in Table 3.2. In order to reveal the grain boundaries and observe the microstructure properly, a thermal etched was performed on an electric furnace: heating rate of 5 ºC/min, temperature of 1200 ºC, dwell time of 30 minutes and cooling rate of 5 ºC/min. Both, reference material and the samples produced were etched on the same conditions.

Table 3.2 - Polishing procedure performed on a Struers TegraPol-25 at INNOVNANO.

| | **Grinding** | | **Polishing** | | |
|---|---|---|---|---|---|
| **Step** | 1 | 2 | 3 | 4 | 5 |
| **Abrasive sand paper** | MS- Piano 220 | MD-Piano 1200 | MD-Largo + 9 µm DP* | MD-Dac + 6 µm DP* | MD-Nap + 1 µm DP* |
| **Speed (rpm)** | 300 | 150 | 150 | 150 | 150 |
| **Force (N)** | 300 | 210 | 180 | 150 | 150 |
| **Time (min)** | ~ 8 | 2 | 8 | 6 | 1 |

* DP – Diamond Paste

The grain size was measured using *ImageJ* software. The interception method line was used by measuring the length of a crossing grain with the horizontal lines (in blue), presented in Figure 3.14. The length measurement started from a grain boundary and finished when another grain boundary appeared. In order to record a mean grain size value, three SEM micrographs of each composition were measured.

It was assumed that the grains were spherical and the equation 3.14 was applied:

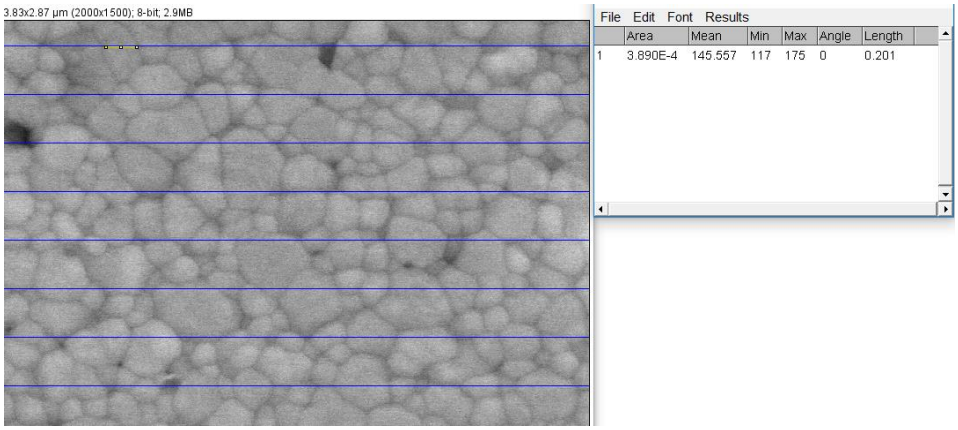


Figure 3.14 - Grain size measurement by line interception method, on *ImageJ* software.

$$\bar{G} = K\frac{\Sigma L}{N} \qquad \textbf{(Equation 3.14)}$$

Where $\bar{G}$ is the mean grain size, *K* corrects the position effect of the cutting plane on the interception line length (1.5 for spherical grains), *L* is the length of line interception and *N* is total number of interceptions.

### 3.6.2. X-ray Photoelectron Spectroscopy (XPS)

X-ray photoelectron spectroscopy is a surface technique that uses the photoelectrons emitted from the sample surface due to the interaction with an X-ray beam. It is an elemental analysis and the XPS peaks are marked as an element symbol and a shell symbol from where the photoelectron was emitted [56] .

XPS spectra were acquired in an Ultra High Vacuum (UHV) system with a base pressure of $2x10^{-10}$ mbar. The system is equipped with a hemispherical electron energy analyser (SPECS Phoibos 150), a delay-line detector and a monochromatic AlKα (1486.74 eV) X-ray source. High resolution spectra were recorded at normal emission take-off angle and with a pass-energy of 20 eV, which provides an overall instrumental peak broadening of 0.5 eV.

Only the sample with more dopant content (0.4 wt %) was measured, using an electron gun for charge compensation, due to sample insulator character, with the purpose of investigate the oxidation state of Fe ions. The spectrum of Fe2p region was fitted using *XPSPEAK* software.

## 3.7. Mechanical Characterization of sintered samples

In order to evaluate the mechanical behaviour of the sintered samples, Vickers hardness (HV10), fracture toughness ($K_{IC}$) and biaxial flexural strength ($\sigma_{flexural}$) were determined. This section is dedicated to a brief description of each method used.

### 3.7.1. Flexural Strength

The biaxial flexural strength (piston-on-three ball arrangement) of sintered samples was determined using a Testing Machine Zwick/Roell Z020. Piston-on-three-ball tests have been selected by the International Organization for Standardization to establish ISO 6872 for the evaluation of the biaxial strength of zirconia ceramics. The samples were polished according to Table 3.2, however one of the samples surface was completely polished while the other was just grinded. Each sample (diameter ~15 mm) was placed centrally on top of three hardened steel balls. In order to record an average value of flexural strength ten samples of each composition were evaluated. The flexural strength, $\sigma_{flexural}$, was calculated from equation 3.15:

$$\sigma = -0.2387 P(X - Y)/b^2 \qquad \textbf{(Equation 3.15)}$$

where *P* is the total load causing fracture (N), *b* is the specimen thickness (mm), *X* and *Y* are given by the following equations:

$$X = (1+\upsilon)\ln(r_2/r_3)^2 + [(1-\upsilon)/2](r_2/r_3)^2 \qquad \textbf{(Equation 3.16)}$$

$$Y = (1+\upsilon)[1+\ln(r_1/r_2)^2] + (1-\upsilon)(r_1/r_3)^2 \qquad \textbf{(Equation 3.17)}$$

where $\upsilon$ is the Poisson's ratio which was a constant value of 0.25, $r_1$ is the radius of the support circles (5 mm), $r_2$ is the radius of the loaded area (0.75 mm) and the $r_3$ is the radius of the specimen (~7.5 mm).

### 3.7.2. Vickers Hardness (HV10)

Hardness is often defined as the resistance of a material to penetration. A Vickers hardness is a test in which a square-based sharp pyramidal diamond indenter, having specified face angles (136 º) is load on the sample surface under a defined force, held for a defined

duration and removed, as it can be seen from Figure 3.15 [57]. The indentation diagonal lengths are measured, the mean result calculated, and this value then employed to calculate the hardness value which is equivalent to the mean force per actual unit area of indenter surface contacting the test surface given by:

$$HV = \frac{F}{A_{ind}} \qquad \textbf{(Equation 3.18)}$$

where $F$ is the applied force (kgf) and $A_{ind}$ is the indentation surface area ($mm^2$) that is expressed as:

$$A_{ind} = \frac{d^2}{2\sin\left(\frac{136^o}{2}\right)} \approx \frac{d^2}{1.8544} \qquad \textbf{(Equation 3.19)}$$

where $d$ is the average length in millimetres of the diagonal caused by indentation.

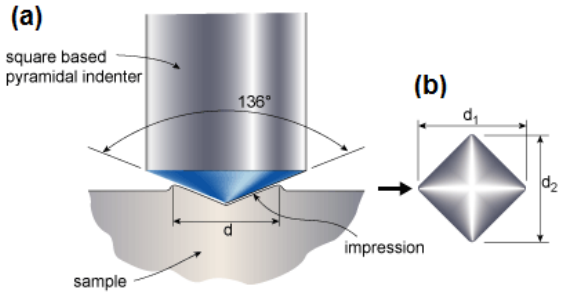


Figure 3.15-(a) Vickers indentation and (b) length of the diagonal caused by indentation ($d_1$ and $d_2$) [57].

In this work, the hardness of the sintered samples was determined using a WIKI 100B equipped with *Affri Fully Automatic System* software (Figure 3.16). Ten Vickers indentations, using a load of 10 kgf, were performed in different points of each sample. The load was kept constant during 15 seconds in each indentation. The values were recorded by the software used, and the average value was calculated from the ten different measurements. As in the flexural strength test, the samples were polished according to Table 3.2, however one of the sample surface was completely polished while the other was just grinded.

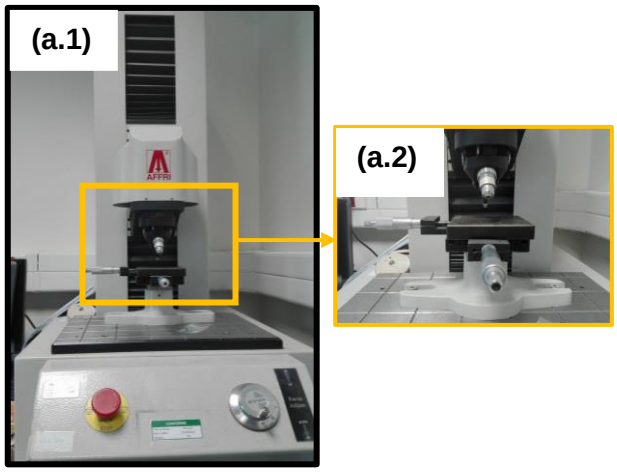


Figure 3.16 - (a.1) Vickers Hardness Equipment WIKI 100B and (a.2) pyramidal diamond indenter and optical microscopy.

### 3.7.3. Fracture Toughness

The fracture toughness, $K_{IC}$, is a measure of the resistance to crack extension in a brittle material. In this work, the fracture toughness was estimated by the Vickers indentation technique. Cracks are formed in the corners of indent and this type of indentation is designated Palmqvist [58]. The following equation is designated by Niihara equation [58] and is the one that is used in INNOVNANO for fracture toughness determination:

$$K_{IC} = 0.0357 \times HV^{\frac{3}{5}} \times E^{\frac{2}{5}} \times a_{ind} \times c_{ind}^{-\frac{1}{2}} \qquad \textbf{(Equation 3.20)}$$

where *HV* is the Vickers Hardness, *E* is the Young's Modulus which was a constant value of 210 GPa, $a_{ind}$ is the half distance of indent diagonal, and $c_{ind}$ is the crack length formed on the indentation corners, as it can be seen from Figure 3.17, which was measured by optical microscopy. In order to determine an average value, ten measurements were performed on polished surfaces (see table 3.2).

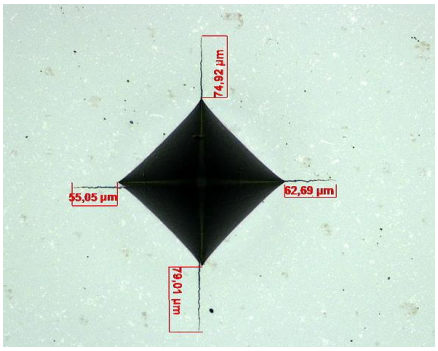


Figure 3.17 - Measurement of the crack lengths formed on the corners of the indentation [59].

# CHAPTER 4

## 4. Results and Discussion

In this chapter, the most relevant results obtained through morphological, structural, optical and mechanical characterization of the reference material and the produced samples will be presented and discussed.

## 4.1. Reference Material Characterization

First of all, the reference material was characterized from the microstructural, structural and optical point of view, in order to go through a deep investigation of a reference sample collecting hints to overcome a zirconia formulation which physical properties meet the reference material. The only provided information regarding the reference material was that it was based on 3YSZ formulation which chemical composition and processing were unknown.

### 4.1.1. Microstructure and Composition

The microstructural characterization of the reference material was assessed by SEM and the elemental composition by EDXA. The thermal etching did not reveal the grain boundaries, therefore a cross sectional observation was performed.

By the analysis of SEM micrographs, showed in Figure 4.1**,** the crystals seem to have a prismatic habit in a homogenous and dense structure. The correlated EDXA analysis is presented in Figure 4.2 and the elemental composition was determined. EDXA-SEM revealed the presence of elements such as zirconium (Zr), hafnium (Hf) and yttrium (Y). The presence of hafnium in zirconia based materials is commonly reported due to their chemical structure similarity ($HfO_2$ and $ZrO_2$ are isomorphs) [60]. Besides that, $HfO_2$ is normally described as an impurity which is commonly present in zirconia raw materials. However, the presence of other elements that could be responsible for the *beige* colour were not detected.

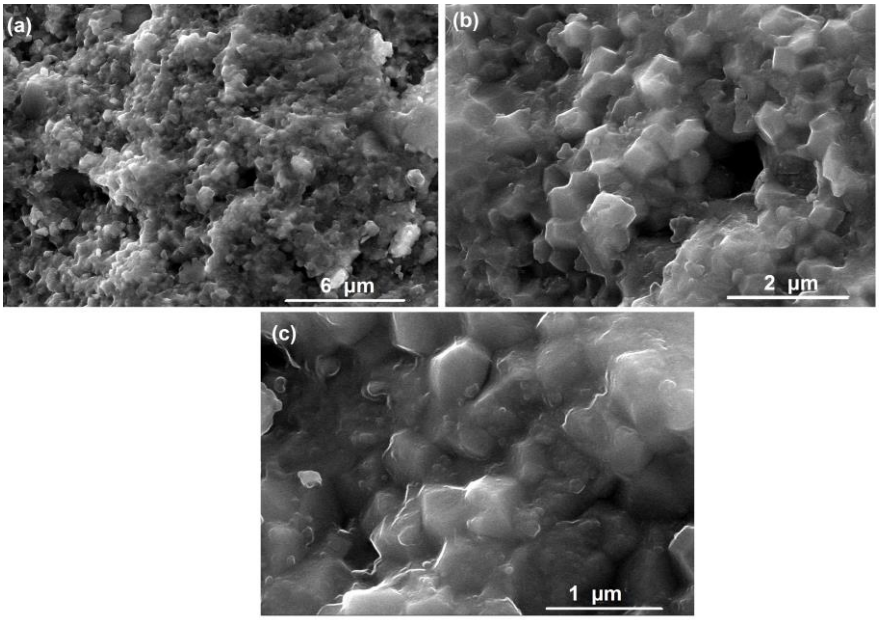


Figure 4.1 - Cross-section SEM micrographs of the reference material before thermal treatment with magnifications of (a) 5000x, (b) 15000x and (c) 30000x. Acceleration of electron beam of 25.0 kV

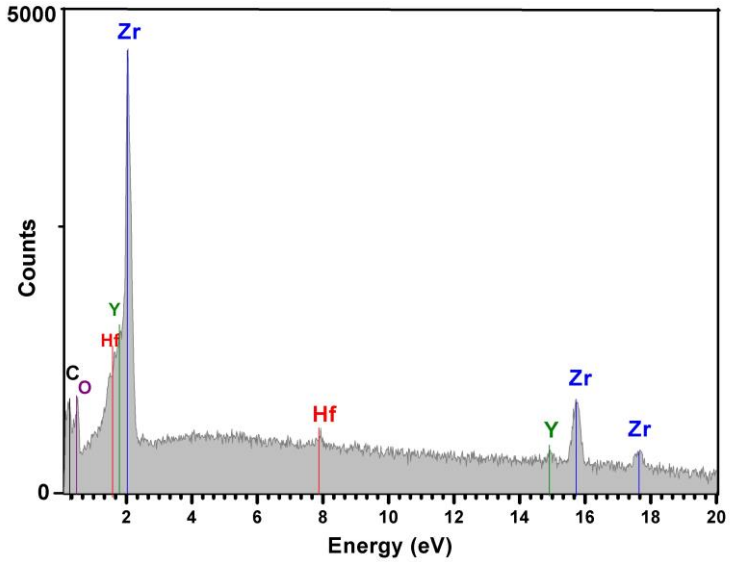


Figure 4.2 - SEM-EDXA of reference material.

It is important to refer that it was attempted to determine the reference material chemical composition through ICP (Inductively Coupled Plasma), but it was not possible due to the difficulty of dissolving the sample.

### 4.1.2. Structural Characterization

The structural characterization of the reference material was accomplished by X-ray diffraction and Raman Spectroscopy. It should be noted that the reference material after a thermal treatment in air (heating rate 5 ºC/min, maximum temperature of 1200 ºC, 30 min of dwell time and cooling rate of 5 ºC/min on an electric furnace) lost its *beige* colour and became colourless (white), as presented in the Figure 4.3. Accordingly, the samples (non-thermally treated and thermally treated) were subjected to several studies, in order to get more information to evaluate the mechanism behind the colour. Furthermore, the thermally treated (in air) sample was then subjected to a thermal treatment in a reducing atmosphere (heating rate of 5 ºC/min, in atmosphere of 10 % $H_2$ – 90% $N_2$, maximum temperature of 1200 ºC, dwell time of 4 hours, oxygen partial pressure ($pO_2$= $10^{-21}$ atm) and a cooling rate of 5 ºC/min) in order to investigate the colour stability in these conditions. As it can be seen from Figure 4.3 (c), the material recovered its *beige* colour, however the colour intensity is lower comparatively to the original reference material colour (Figure 4.3 (a)).

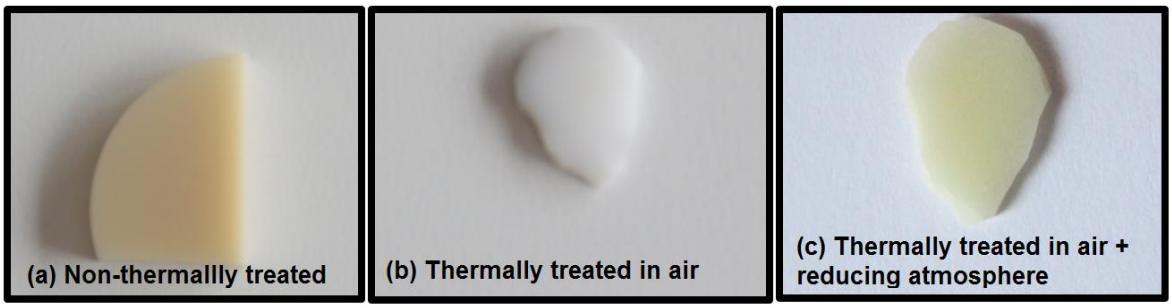


Figure 4.3 – Digital photographs of non-thermally (a) and thermally (b) treated reference samples and (c) thermally treated in air followed by an annealing in a reducing atmosphere.

To evaluate the crystallographic phases composition, the samples were examined by XRD. Figure 4.4 displays the XRD patterns and these results were collected in the same diffraction conditions. The samples were firstly polished and the analysis was performed in the bulk samples since milling can induce phase transition during mechanical loading.

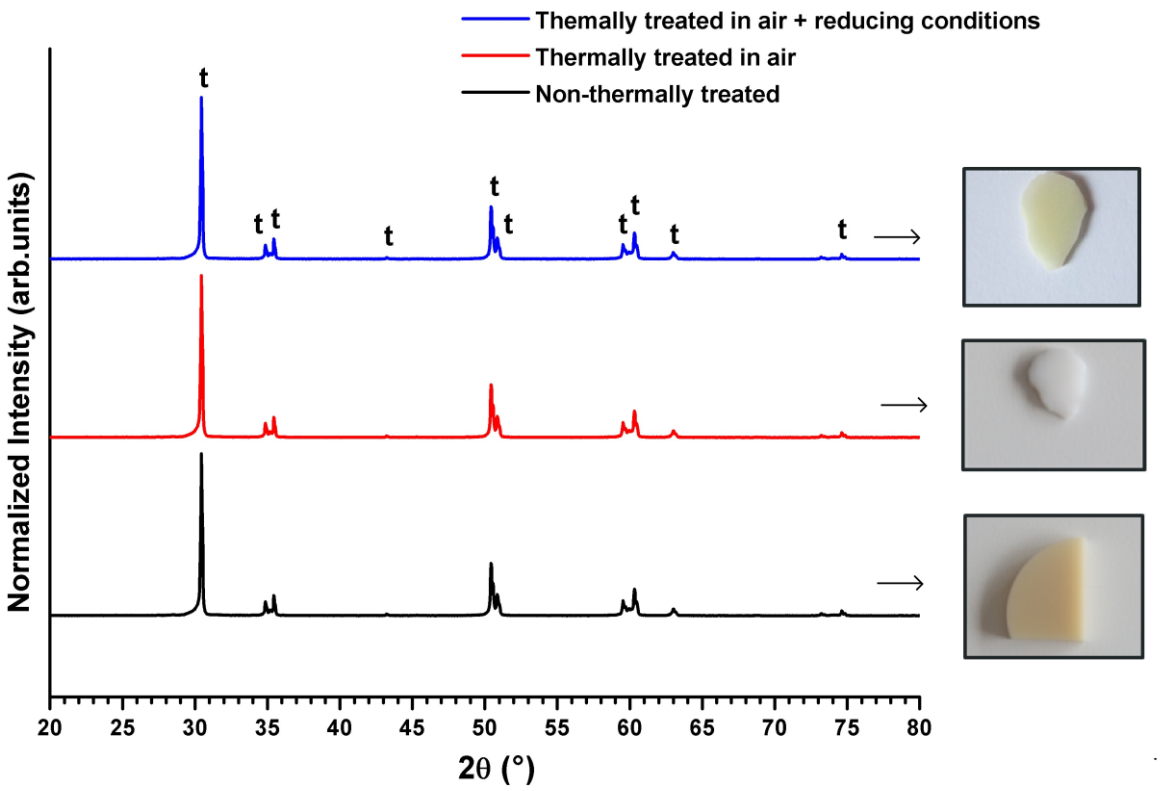


Figure 4.4 - XRD patterns of the reference material samples: non-thermally treated, thermally treated in air and thermally treated in air followed by a thermal treatment in reducing atmosphere. t denotes zirconia tetragonal phase.

As it can be seen from Figure 4.4, no significant differences in the diffraction patterns of the samples, before and after thermal treatments, were observed. In fact, only zirconia tetragonal phase was detected in all the XRD patterns since all the peaks were identified as zirconia tetragonal phase and thereby no second phases were found. According to this result, we can assume that the thermal treatment either in air or in a reducing atmosphere did not promote phase transition from the metastable tetragonal to monoclinic phase. Besides that, further information about crystallographic phases that could be responsible for the original reference material colour was not found.

Micro Raman analysis under a 442 nm wavelength excitation source has been exploited since this technique allows to distinguish very clearly the different allotropes of zirconia comparatively to XRD. It should be noted that tetragonal phase is a metastable phase, and in micro-Raman analysis the penetration depth of 442 nm wavelength in zirconia is close to 0.2 μm. The samples were firstly polished and Figure 4.5 displays the Raman spectra obtained in all samples.

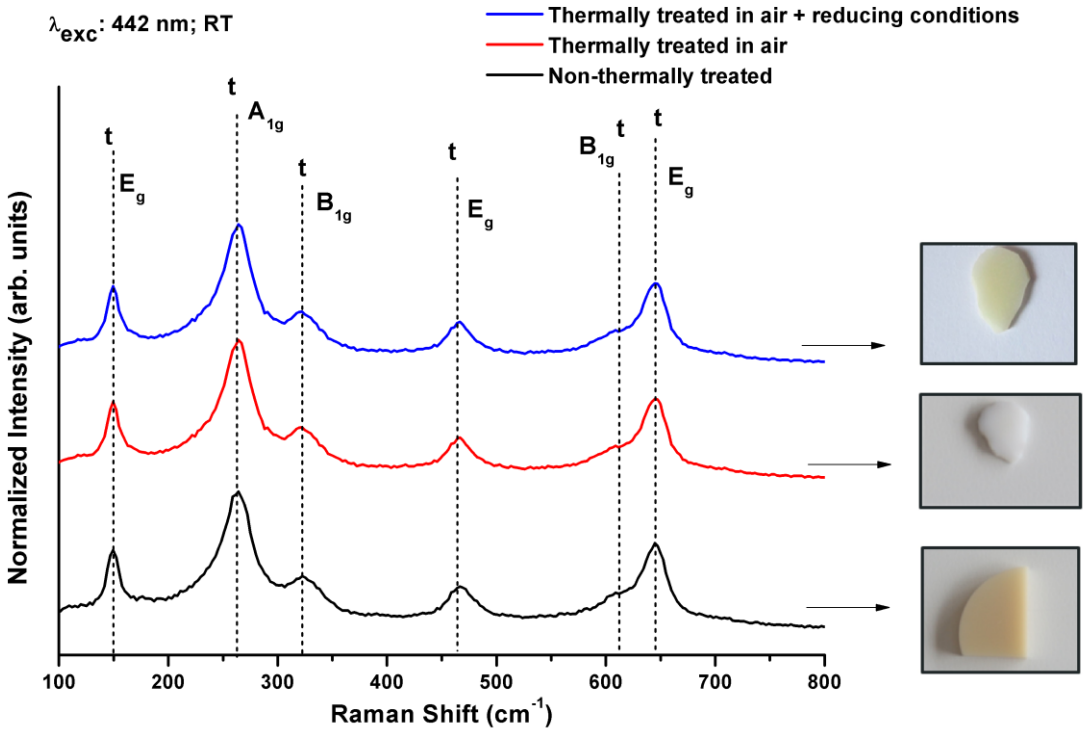


Figure 4.5 – Raman spectra under 442 nm wavelength excitation of the reference material samples: non-thermally treated, thermally treated in air and thermally treated in air followed by an annealing in a reducing atmosphere. t denotes zirconia tetragonal phase.

The characteristic Raman active modes of the t-phase were clearly seen in all spectra being identified around 149, 264, 323, 466, 611, and 646 $cm^{-1}$ assigned to $E_g$, $A_{1g}$, $B_{1g}$, $E_g$, $B_{1g}$, $E_g$ symmetries, respectively. No significant differences were observed in the collected Raman spectra and no second phases were detected, in accordance with XRD patterns previously presented.

Furthermore, the reference sample was analysed before polishing, in order to evaluate the effect of superficial treatments as polishing on the surface phase distribution of the non-thermally treated sample, using Raman mapping. The green and red regions were defined by vertical lines between 163 to 197 $cm^{-1}$ and 364 to 390 $cm^{-1}$, respectively, whose bands correspond to the monoclinic Raman active modes. On the other hand, the blue region was defined in a range of 227 to 288 $cm^{-1}$ associated to tetragonal peak of zirconia, as it can be seen from Figure 4.6.

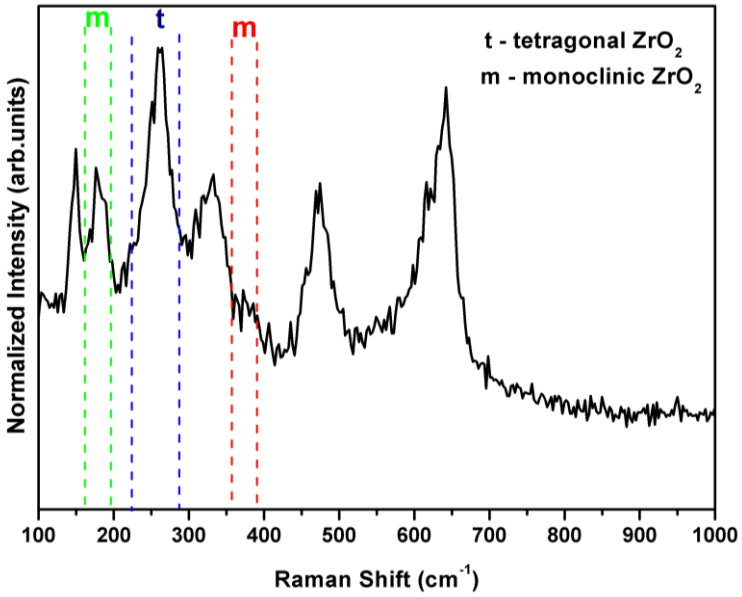


Figure 4.6 – Defined monoclinic and tetragonal regions for Raman mapping of non-polished reference sample surface.

Initially, the sample surface was investigated by optical microscopy, Figure 4.7 (a), where different areas were observed. On that region, a scan mode of 20x20 μm was defined and Raman data was acquired resulting in the maps presented on Figure 4.7 (b.1-b.4). The construction of the Raman images was based on the peaks intensity corresponding to each phase, namely Figure 4.7 (b.1 -b.2) monoclinic, (b.3) tetragonal. In order to better observe the phase distribution on the material surface, a composed image generated by the ratio of the monoclinic/tetragonal peaks intensity is presented (Figure 4.7 (b.4). As it can be seen, both phases are coexistent on the sample surface, however, tetragonal phase is the most predominant. Optical observation allowed to clearly identify a region where the monoclinic phase is present, usually, in a depressed area. The presence of monoclinic phase on the surface of zirconia materials is commonly reported since surface metastable tetragonal grains are not constrained by the matrix and can transform to monoclinic spontaneously [1]. Besides that, according to Deville and co-workers [61], when a defect is created at the surface, it leaves a homogeneous stress state in its surroundings and the areas affected by these stresses will later transform into zirconia stable polymorph. The presence of these defects, has, consequently, an extremely damaging influence on the ageing sensitivity, as they act as nucleating agents and accelerate surface degradation. From their experiments,

monoclinic spots nucleate preferentially along these defects/scratches. In fact, this was also clearly observed during this work, as it can be seen from Figure 4.7.

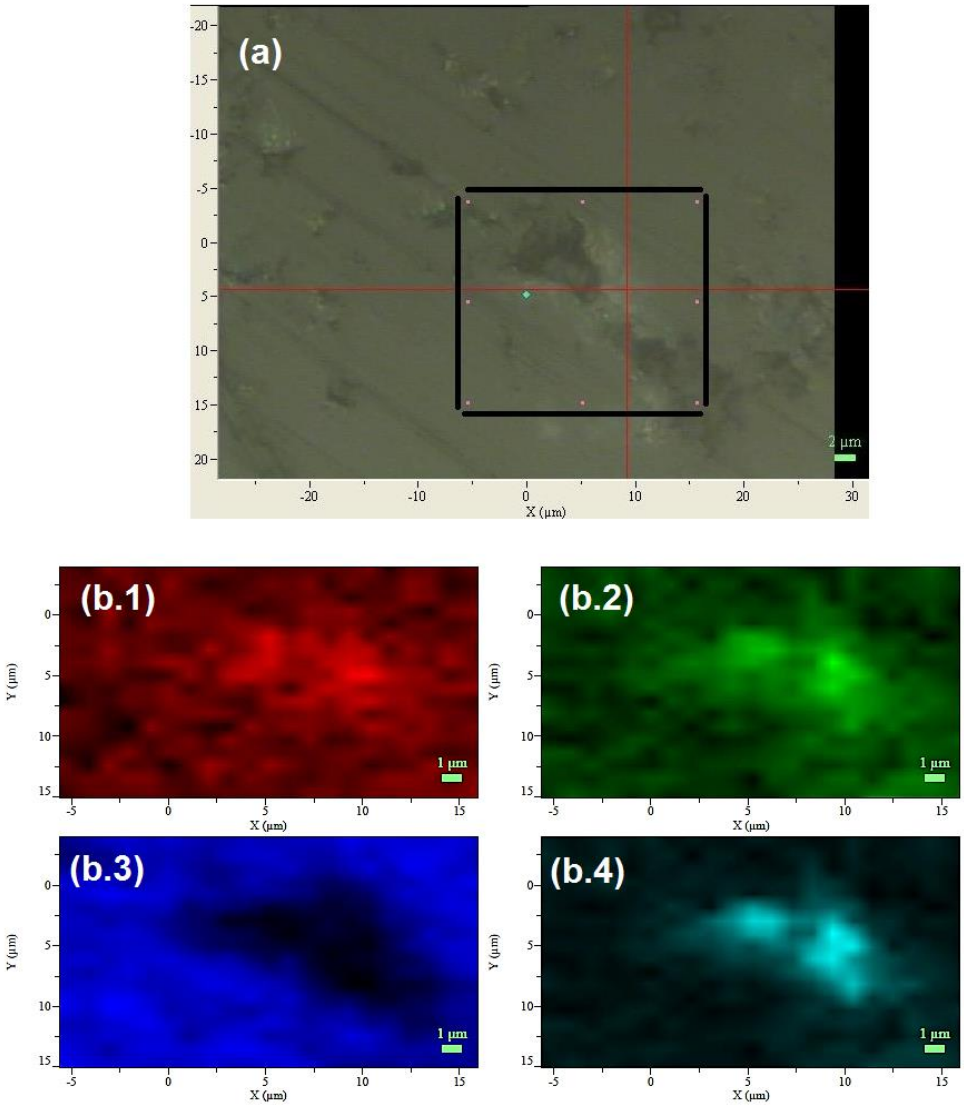


Figure 4.7 – (a) Optical micrograph of the non-thermally treated sample surface under study. Raman maps of (b.1) – (b.2) monoclinic peaks, (b.3) tetragonal peak and (b.4) monoclinic/tetragonal peak intensity ratio.

### 4.1.3. Optical Characterization

The photoluminescence (PL) was used regarding the investigation about the presence of specific ions on the 2YSZ matrix responsible for the *beige* colour in the reference material. This study was made at room temperature,12K (Figure 4.8 (a)) and also as a function of

temperature (Figure 4.8 (b)) under a 325 nm (UV) wavelength excitation laser source. Both samples, non-thermally treated (Figure 4.8) and thermally treated in air (Figure 4.9) were analysed. The used excitation energy (3.81 eV) is below the tetragonal zirconia band gap which was predicted by theoretical models as 6.4 eV for the tetragonal phase [22]. PL measurements permit to visualize a large band centered within the yellow-orange visible spectrum region at ~627 nm and ~688 nm at RT and 12K, respectively.

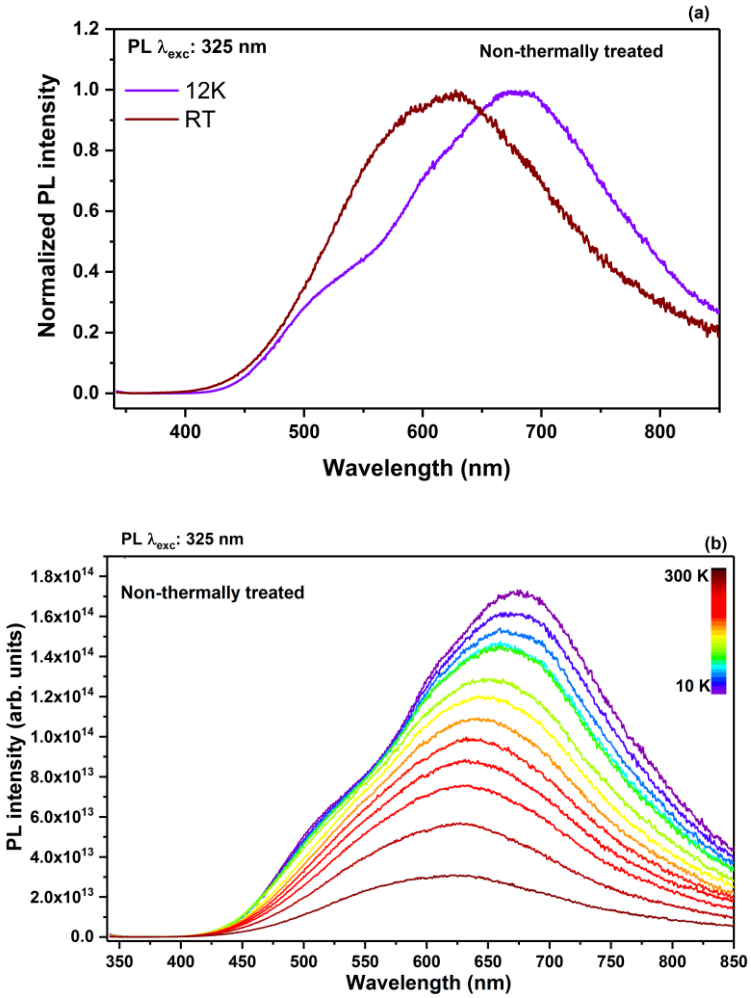


Figure 4.8 - (a) RT and 12 K photoluminescence emission spectra under 325 nm wavelength excitation and (b) temperature dependence spectrum of non-thermally treated sample.

Several studies [37, 62, 63] have been published regarding the origin of this broad emission band that is commonly attributed to intrinsic defects such as oxygen vacancies in the zirconia structure. For each mole of yttria introduced, one mole of oxygen vacancy is created in order to maintain the crystal lattice neutrality. This way, the yellow colour may be due to

the presence of these structural defects which are generated during zirconia stabilization, since there is no trace of other elements once there are no other emissions. In fact, the yellowish-brown appearance of YSZ is commonly attributed to colour centers (oxygen vacancies with trapped electrons) which are easily produced, for instance, in reducing conditions [38]. These defects have energy levels lying within the band gap of the host and thereby can cause strong light absorption and, consequently, produce colouring along with photoluminescence phenomena. Actually, a thermal treatment in an oxidizing atmosphere can promote oxygen diffusion, reducing colour centers [38] thus favouring colour loss, as it was observed (Figure 4.3 (b)). However, the same emission broad band centered in the yellow region (~627 nm) was observed on the PL spectra of the sample thermally treated in air, as it can be seen from Figure 4.9. However, the absolute intensity of this emission is strongly attenuated. According to these results, we can assume that the thermal treatment in an oxidizing atmosphere reduce the intrinsic defects responsible for the colour centers, resulting in decreased emission. It is important to mention that the absolute intensities can be quantitatively compared, once the experimental conditions were kept the same.

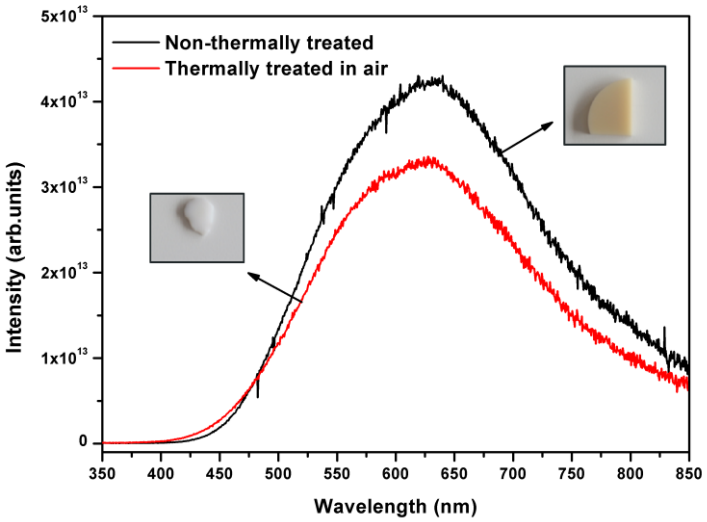


Figure 4.9 - RT PL emission spectrum under 325 nm wavelength excitation of non-thermally and thermally treated in air sample.

In addition to the broad bands observed under the 325 nm excitation, a structured PL emission with two sharp peaks taking place at about 693 and 694 nm was detected in the spectra of all samples when a 442 nm wavelength excitation source was used (Figure 4.10 ). This was observed while using the micro-Raman instrument in the photoluminescence mode.

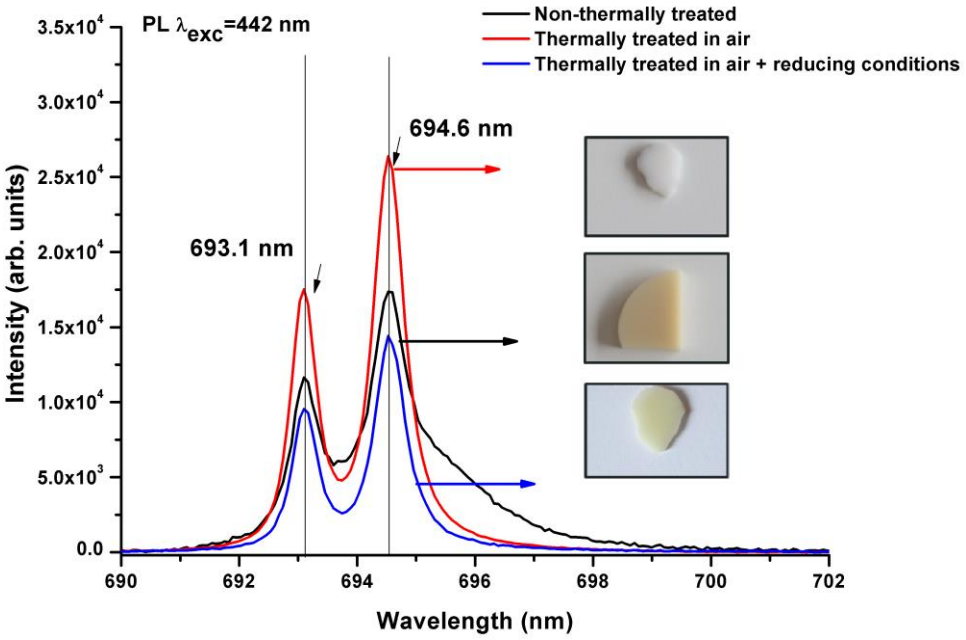


Figure 4.10 – Micro-PL spectra under 442 nm wavelength excitation of non-thermally and thermally treated samples.

In fact, this emission is commonly attributed to the characteristic luminescence of $Cr^{3+}$ doped α-$Al_2O_3$ [64,65] and it is clearly present in the PL spectra of all samples. This way, one can infer that the photoluminescence analysis revealed the presence of $Cr^{3+}$in $Al_2O_3$ in the chemical composition of the reference material. However, since the presence of these PL peaks was detected on the colourless sample (white), we can assume that the presence of $Cr^{3+}$ is not the agent responsible for the reference material original colour. In order to compare the absolute emission intensities of the different PL spectra, the data were normalized to the maximum intensity in the Raman region. As it can be seen, the PL emission of $Cr^{3+}$ is more intense on the sample that has been thermally treated on an oxidizing atmosphere. As previously discussed, this thermal treatment decreased the defects concentration on the material structure due to oxygen diffusion, promoting the passivation of the oxygen vacancies, and thus decreasing the probability of intra-gap transitions. Therefore, the internal absorption of the chromium related emission also decreases, resulting in an overall increase of the $Cr^{3+}$ in $Al_2O_3$ PL emission intensity, overcoming the defect induced emission masking mechanism. Considering the colour loss after heating in air, it can be then assumed that the thermal treatment promoted a structural rearrangement, in which intrinsic defects such as colour centers were suppressed by the oxygen diffusion, and the sample turned colourless (white). On the other hand, the thermal

treatment in a reduced atmosphere provided the conditions for these colour centers reformation, producing the colour recovery. In fact, as mentioned before, Wachsman *et al.* [63] reported that polycrystalline YSZ darkens upon reduction due to the creation of F-center type defects and the intensity of coloration is dependent on the annealing time.

The reflectance spectrum and the colour coordinates of the non-thermally treated sample were also recorded which will be discussed later on, Chapter 4.2, where the results are compared with the produced samples.

Summarizing the results of this section, the reference material colour (non-thermally treated) seems to be attributed to intrinsic defects (colour centers). This means that this way of colouring the samples, besides being non-permanent (temperature sensitive), is not very controllable since it is difficult to reproduce the same degree of intrinsic defects. Hence, in the current work, the dopant addition was the chosen strategy to reproduce the *beige* colour.

## 4.2. Spray Dried Powder Characterization

The physical properties of the starting powder, including particle size, particle size distribution, specific surface area and morphology have a strong influence on the ceramic compaction behaviour and subsequent densification. The influence of the powder properties in the sintering ceramics has been studied by Yan [19]. According to his study, the production of high-quality controlled microstructures requires starting powders that have the following characteristics:

- Sub-micron particle size;
- Narrow particle size distribution;
- Uniform particle shape;
- Presence of soft agglomerates that are broken down easily;
- High purity;
- Precise amount of stabilizing oxide.

Since the final properties are largely dependent on the quality of the starting powders, this section is dedicated to a full characterization of the spray dried powders used for sample synthesis following the INNOVNANO's quality control procedure.

### 4.2.1. Particle Size Distribution

The particle size distribution of the particles in suspension with different amounts of dopant, after ball milling stage, was measured by laser diffraction and it is presented in Figure 4.11

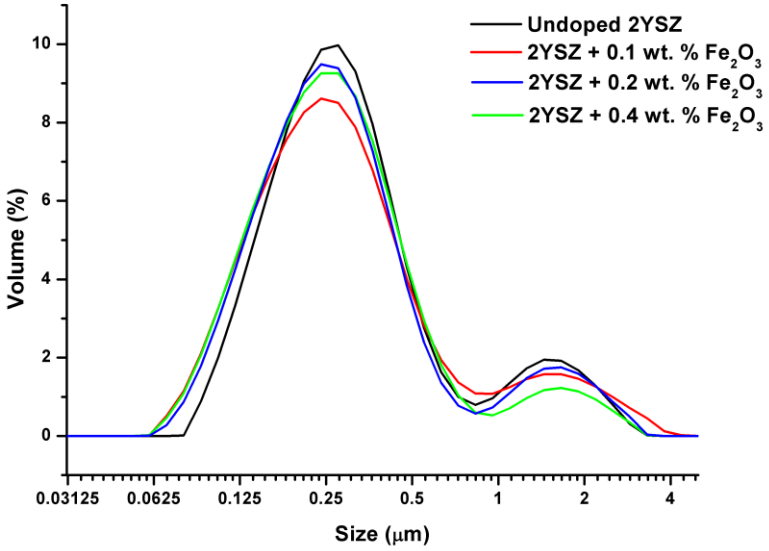


Figure 4.11- Particle size distribution of the particles in suspension containing different contents of dopant.

From the Figure 4.11 analysis it is possible to confirm a bimodal distribution with particles size ranging from 0.06 to ~3 μm. As it can be seen from Table 4.1, the particles have a $d_{50}$ value close to 0.250 μm which indicates that the ball milling process deagglomerated successfully the particles. The particle size distribution must be controlled in order to avoid a heterogeneous particle size after spray drying. Indeed, the suspensions were spray dried with a starting particle size close to 0.250 μm.

After spray drying process, the particle size distribution was also measured by the same technique and the results are displayed in Figure 4.12. The suspensions were dried containing ~20 wt. % of solids and the spray dried parameters as inlet and outlet temperature were previously defined as 180 ºC and 80 ºC, respectively. Almost all compositions exhibit a bimodal distribution size ranging from 0.5 to 60 μm with a $d_{50}$ of ~4 μm, as it can be seen from Table 4.1. However, the powder with 0.2 wt. % of dopant presented a broad size distribution with the particle size ranging from ~0.4 to ~ 130 μm, with a $d_{50}$ of ~9 μm. This difference can be attributed to spray drying process parameters,

namely, the pumping pressure which was not controllable. The morphology of the powders was also evaluated and it will be present later on.

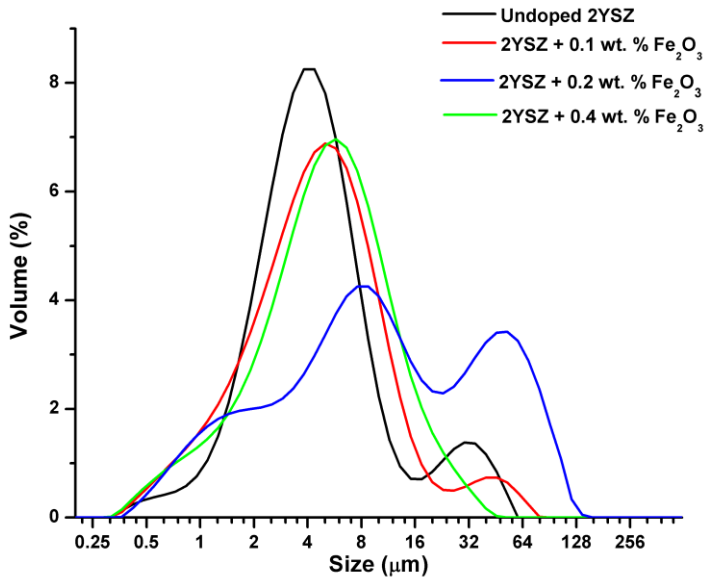


Figure 4.12 – Particle size distribution of the spray dried powders measured by laser diffraction.

Table 4.1 - Mean diameter of the particles in the suspension and of the spray dried powders with different dopant contents.

| Particle Size Distribution (μm) | | |
|---|---|---|
| **Composition** | **Suspension** | **Spray dried powders** |
| **Undoped 2YSZ** | 0.260 | 3.86 |
| **2YSZ +0.1 wt. % $Fe_2O_3$** | 0.247 | 4.23 |
| **2YSZ + 0.2 wt. % $Fe_2O_3$** | 0.243 | 8.96 |
| **2YSZ + 0.4 wt.% $Fe_2O_3$** | 0.240 | 4.79 |

The particle size should provide maximum particle packing and uniformity during shaping. The densification rate for a system composed by uniformly compacted fine powders is higher than for a similar system with heterogeneous packing. A wider particle size distribution results in abnormal grain growth during sintering, which is extremely detrimental to successful consolidation into bulk ceramics [31]. Furthermore, if the particle size distribution is narrow, the driving force for grain growth due to the curvature of the boundary is small [66].

In fact, some degree of agglomeration was noticed after spray drying process, which may affect negatively the final mechanical properties, discussed later on Chapter 4.3.2.

### 4.2.2. Morphology

The morphology of the spray dried powders was evaluated by SEM. From SEM micrographs observation (Figure 4.13), it was possible to confirm the presence of some particles aggregation but also some agglomerates with spherical shape (granules), consequence of spray-drying process. In fact, most ceramic powders are composed of small particles which have a very high specific surface area and therefore a high surface energy. In order to reduce this surface free energy, the particles tend to agglomerate forming granules [67].

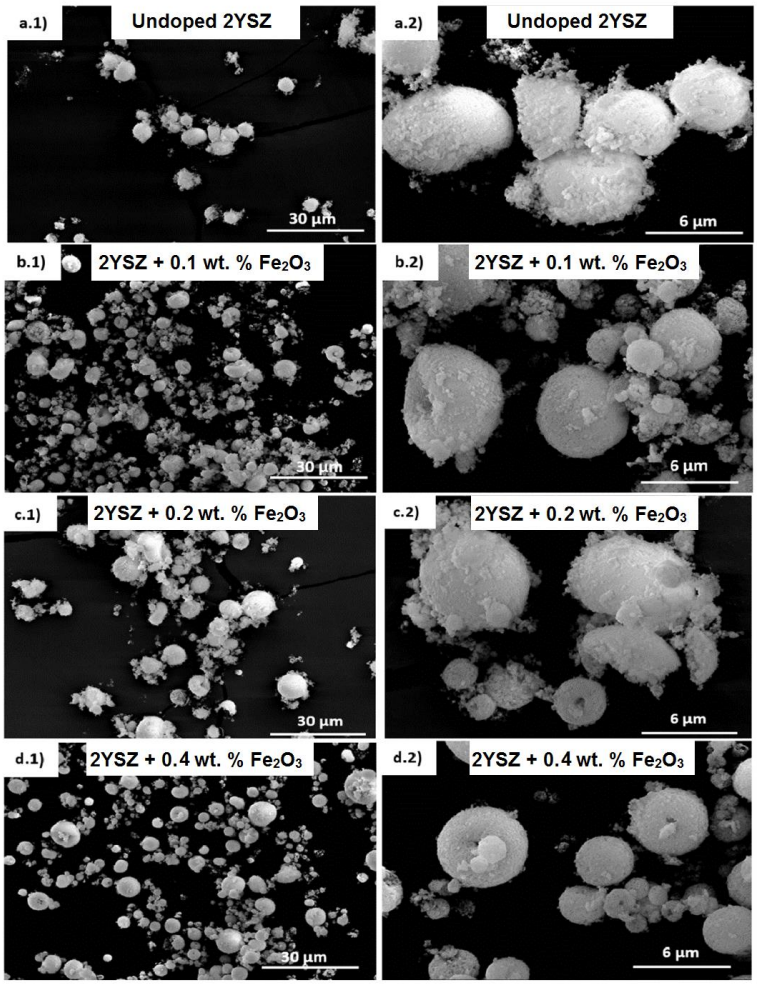


Figure 4.13 - SEM micrographs of 2YSZ spray dried powders (a.1- a.2) undoped; (b.1 - b.2) doped with 0.1 wt. %; (c.1- c.2) doped with 0.2 wt. %; (d.1- d.2) doped with 0.4 wt. % of $Fe_2O_3$. The magnifications were 1000x and 5000x, respectively. Acceleration of electron beam of 25 kV.

### 4.2.3. Specific Surface Area

The specific surface area ($m^2/g$) was measured by BET isotherm method and Table 4.2 exhibits the results obtained.

Table 4.2 - Specific surface area ($m^2/g$) of the spray dried powders measured by BET isotherm method.

| Composition | Specific surface area ($m^2/g$) |
|---|---|
| **Undoped 2YSZ** | 19.07 |
| **2YSZ + 0.1 wt. % $Fe_2O_3$** | 19.99 |
| **2YSZ + 0.2 wt. % $Fe_2O_3$** | 19.56 |
| **2YSZ + 0.4 wt. % $Fe_2O_3$** | 19.48 |

All compositions present nearly identical values of SSA. Comparing these values with the SSA value presented (~25 $m^2/g$) on 2YSZ INNOVNANO's technical data sheet), the SSA values obtained are lower, indicating that the particle size is higher. In fact, this in agreement with the particle size distribution of the spray dried powders (see Figure 4.12) as well as with the powders morphology observed by SEM (see Figure 4.13).

### 4.2.4. Chemical Purity

The chemical composition of the spray dried powders was evaluated by X-ray fluorescence and the results are showed in Table 4.3. This technique was used to evaluate the chemical purity but also to detect the presence of $Fe_2O_3$ that was added intentionally. As expected, the chemical composition of the powders is typically: ~94 wt. % of $ZrO_2$, ~3.6 wt. % of $Y_2O_3$ (~2 mol %) and ~1.7 wt. % of $HfO_2$. The presence of ~4000 ppm of $Al_2O_3$ was detected and in fact, this oxide is always intentionally added to the zirconia powders during milling process at INNOVNANO. The chemical composition of the different powders is quite similar. As predictable, the higher content of $Fe_2O_3$ (3569 ppm) was detected for the powder that was intentionally doped with more content of this oxide. In the case of the powder doped with 0.2 wt. % of $Fe_2O_3$, a smaller quantity of this oxide was found (~1591 ppm) comparatively to the initial dopant added. Furthermore, the chemical composition of the powder doped with 0.1 wt. % of $Fe_2O_3$ revealed a higher concentration of $Fe_2O_3$ (~1341 ppm) in comparison with the initial content used for doping. Other minority elements such as $SiO_2$, $MgO_2$, CaO, CuO and ZnO are presented in a very low content (< 200 ppm).

Table 4.3 - Chemical composition of spray dried powders (undoped and doped) analysed by XRF.

| Composition | Undoped 2YSZ | 2YSZ- 0.1 wt. % $Fe_2O_3$ | 2YSZ-0.2 wt. % $Fe_2O_3$ | 2YSZ-0.4 wt. % $Fe_2O_3$ |
|---|---|---|---|---|
| | | wt % | | |
| **$ZrO_2$** | 94.2 | 94.1 | 94.1 | 93.9 |
| **$HfO_2$** | 1.7 | 1.7 | 1.7 | 1.6 |
| **$Y_2O_3$** | 3.6 | 3.6 | 3.7 | 3.6 |
| | | **ppm** | | |
| **$Al_2O_3$** | 4250 | 4096 | 4058 | 3993 |
| **$SiO_2$** | 42 | 44 | 36 | 34 |
| **$MgO_2$** | 140 | 135 | 128 | 134 |
| **CaO** | 117 | 106 | 101 | 98 |
| **$Fe_2O_3$** | 175 | 1341 | 1591 | 3569 |
| **CuO** | 35 | 24 | 25 | 24 |
| **ZnO** | 16 | 25 | 24 | 26 |

### 4.2.5. True Density

The true density of the powders was measured by Helium pycnometer and the Table 4.4 displays the results. The true density of the powder was not affected by the addition of $Fe_2O_3$ and the values are nearly identical for all doped powders (~5.7 g/cm$^3$).

Table 4.4 - True density of spray dried powders measured by Helium Pycnometer.

| Composition | True Density (g/cm$^3$) |
|---|---|
| **Undoped 2YSZ** | 5.62 |
| **2YSZ + 0.1 wt. % $Fe_2O_3$** | 5.68 |
| **2YSZ + 0.2 wt. % $Fe_2O_3$** | 5.68 |
| **2YSZ + 0.4 wt. % $Fe_2O_3$** | 5.67 |

### 4.2.6. Crystallographic Phases Composition

The crystallographic phases of the spray dried powders were evaluated by X-ray diffraction analysis. The Figure 4.14 shows the diffraction patterns obtained.

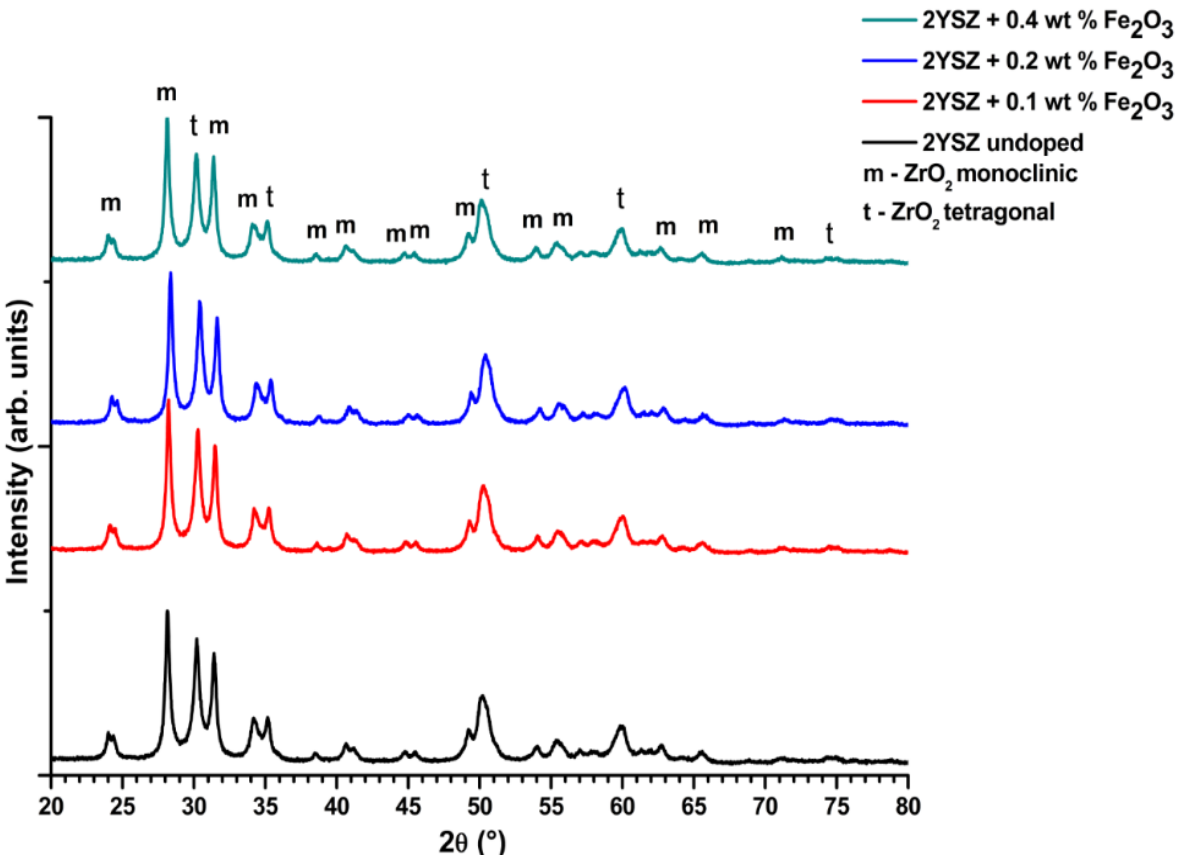


Figure 4.14 - XRD patterns of undoped and doped 2YSZ spray dried powders. m and t denotes monoclinic and tetragonal phases, respectively.

The diffraction patterns revealed that both phases, tetragonal and monoclinic, were detected in all different compositions. The most intense peak detected from tetragonal phase appears at 2Θ ~30.18º while from monoclinic phase appears at ~28.2 º. In fact, the monoclinic phase is the most predominant phase present in all the powders. Considering that the powders were milled before spray-drying process, the mechanical loading produced during milling induced phase transition to the stable form of zirconia, namely, monoclinic phase [68]. Moreover, only after sintering, the monoclinic phase will be transformed to the metastable tetragonal phase, since yttria helps t-ZrO2 stabilization by formation of a solid solution (see Figure 2.5).

### 4.2.7. Dilatometric Analysis

The dilatometric analysis is a very important step to be performed in order to predict and understand the linear expansion or shrinkage of a material when submitted to a thermal cycle. All the compositions (compacted powder) were subjected to a thermal cycle (a heating rate of 5 ºC/min, maximum temperature of 1600 ºC and a cooling rate of 10 ºC/min). The linear shrinkage (%) as function of temperature was recorded as well as the shrinkage rate as shown in Figure 4.15. The compacted powders start to shrink at around ~1000 ºC and a linear shrinkage of ~18 % is achieved at 1300 ºC (Figure 4.15 (a)). In general, linear shrinkage of the samples with different dopant concentration exhibits an identical curve behaviour. However, Zhao *et al*. [69] reported that the addition of a small amount of $Fe_2O_3$ act as a sintering aid, since it reduces the sintering temperature. However, no linear correlation was found between the dilatometric curve behaviour and the dopant concentration. The highest shrinkage rate, which was calculated by the derivative of the linear shrinkage (Figure 4.15 (b) was achieved at nearly identical temperatures (~ 1200 ºC) and no significant differences were observed.

The sintering temperature must be carefully selected in order to avoid an excessive grain growth and microstructural defects such as porosity which can result in mechanical failure or zirconia degradation. Zirconia ceramics are commonly sintered at temperatures ranging from 1300 ºC to 1500 ºC for 2 hours. At these temperatures, all open porosity is removed, the grain grows slowly and high densifications values are attained [68].

In the current work and based on the dilatometric behaviour, the sintering cycle was defined as: heating rate of 2 ºC/min, maximum temperature of 1350 ºC, 2 hours of dwell time and a cooling rate of 5 ºC/min for all compositions.

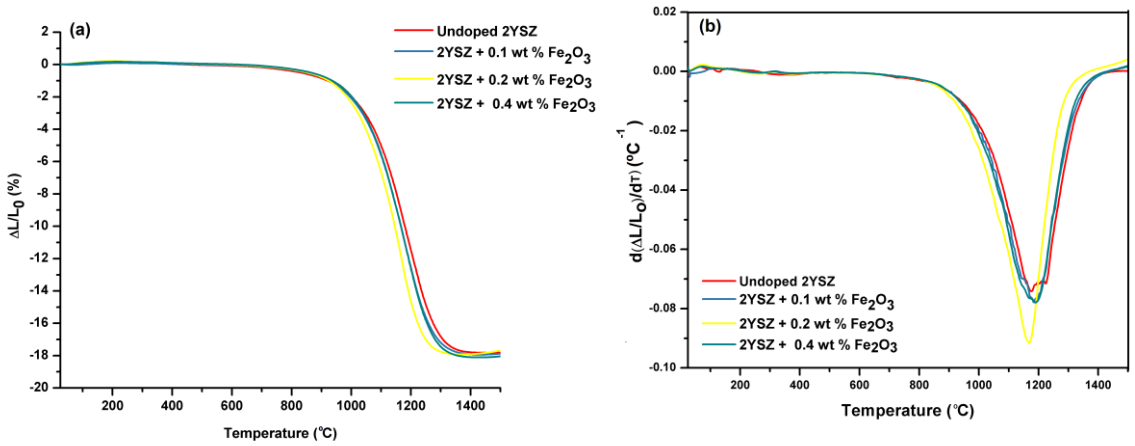


Figure 4.15 – (a) Dilatometric behaviour of undoped 2YSZ and doped with different contents of $Fe_2O_3$ and (b) correlated shrinkage rate.

## 4.3. Characterization of sintered samples

Microstructural, structural and optical analysis, specifically the colour, were performed in order to fully characterized the sintered samples. Figure 4.16 shows the digital photographs of the samples produced with different dopant concentration. The colour was succesufly changed by the dopant addition, becoming darker as the dopant content increases.

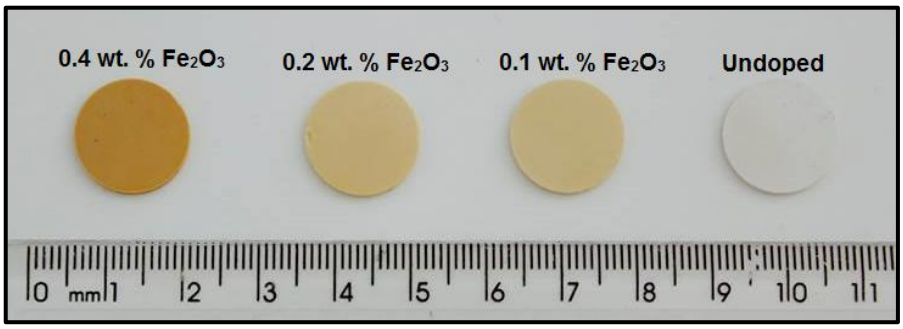


Figure 4.16 - Digital photographs of the produced samples with different contents of $Fe_2O_3$ sintered at 1350 ºC for 2 hours.

### 4.3.1. Crystallographic Phase Composition

XRD was used to determine the crystalline phases presented in the sintered samples and to evaluate dopant effect on the crystalline structure. Figure 4.17(a) shows the XRD patterns obtained and Figure 4.17(b) puts in evidence the shift in the peak position. It must be mentioned that the diffraction data was collected in the same diffraction conditions.

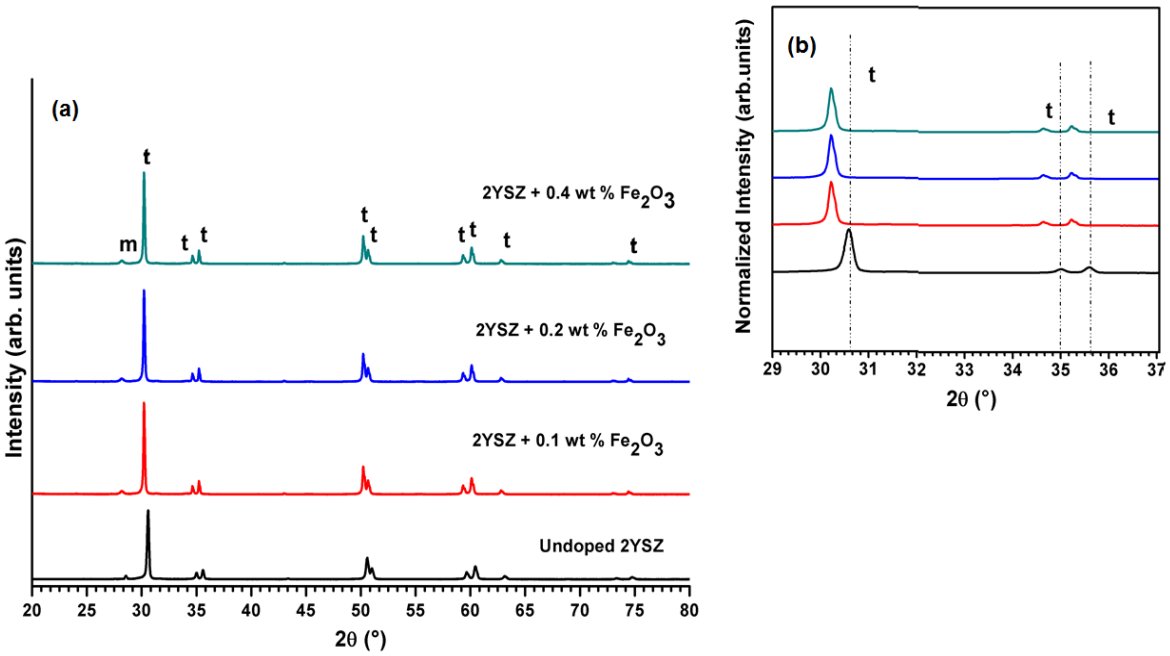


Figure 4.17 – (a) XRD patterns of the sintered samples with different dopant concentration. (b) Shift in the peak position. m and t denote monoclinic and tetragonal phases, respectively.

Analysing the XRD patterns of the sintered samples with different contents of $Fe_2O_3$ it is possible to observe that both phases, monoclinic and tetragonal, coexist. In fact, the samples sintered at 1350 ºC are mostly constituted by tetragonal zirconia phase. At this sintering temperature, most part of the monoclinic zirconia detected in 2YSZ spray dried powders has been successfully transformed to the beneficial tetragonal zirconia (as mentioned before, tetragonal zirconia has better mechanical properties). As a stabilizer, yttria helps t-$ZrO_2$ stabilization by formation of a solid solution (see Figure 2.5). However, when its content is less than 2.5 mol%, yttria cannot stabilize all the zirconia and that is the reason why a small amount of monoclinic zirconia was detected, as verified in Figure 4.17.

The peak position was affected by the dopant addition as it can be seen Figure 4.17(b). The peaks are shifted towards lower diffraction angles which can be attributed to an increase in the lattice parameters.

A standard pattern was used to refine the diffraction results by Rietveld method and the weight fraction of each phase was determined. Additionally, the lattice parameters (*a,b,c)* and the unit cell volume of tetragonal phase were recorded. An excellent fit was achieved for tetragonal peaks, however, only a poor fit was possible for monoclinic phase, resulting in an increase of Rwp value, which works as a quality indicator of the refinement

(theoretically, it should be lower than 10). Hence, the lattice parameters of monoclinic phase were not assumed due to this high error. The obtained results can be observed in Table 4.5. In all compositions, through this refinement, both phases were detected as previously verified in the diffraction patterns presented in Figure 4.17.

The effect of $Fe_2O_3$ addition on the lattice parameters and consequently on the tetragonal unit cell volume is also shown in Table 4.5. There was a slight increase in the unit cell volume as it can be seen from Figure 4.18. According to previous studies[12], the position of $Fe^{3+}$ in the YSZ lattice is still an open question. However, when $Fe^{3+}$ (undersized ion) occupies interstitials positions the unit cell increases. In the current work, the unit cell volume of tetragonal phase increased with the dopant addition suggesting that $Fe^{3+}$ occupies interstitials positions in the tetragonal lattice. However, in order to determine precisely the position of the dopant in the 2YSZ lattice more detailed studies must be performed (for example, the synthesis of samples with a higher concentration of $Fe_2O_3$).

Table 4.5 puts in evidence a higher fraction of monoclinic phase in the doped samples. It seems that $Fe_2O_3$ destabilizes tetragonal phase. However, these values are not linear with the increase of dopant. As mentioned before, the dopant content is very low and the effect of this dopant in zirconia stabilization is unclear.

Table 4.5 – Rietveld refinement results.

| Composition | Monoclinic phase (%) | Tetragonal phase (%) | Tetragonal cell parameters (Å) | Tetragonal unit cell volume (Å$^3$) | Rwp |
|---|---|---|---|---|---|
| **Undoped 2YSZ** | 3.26 | 96.74 | a=b=3.592<br>c=5.160 | 66.57 | 15 |
| **2YSZ + 0.1 wt.% $Fe_2O_3$** | 7.58 | 92.42 | a=b=3.602<br>c=5.177 | 67.17 | 10 |
| **2YSZ + 0.2 wt. % $Fe_2O_3$** | 6.82 | 93.18 | a=b=3.610<br>c=5.1921 | 67.66 | 16 |
| **2YSZ + 0.4 wt. % $Fe_2O_3$** | 5.80 | 94.20 | a=b=3.615<br>c=5.1952 | 67.89 | 25 |

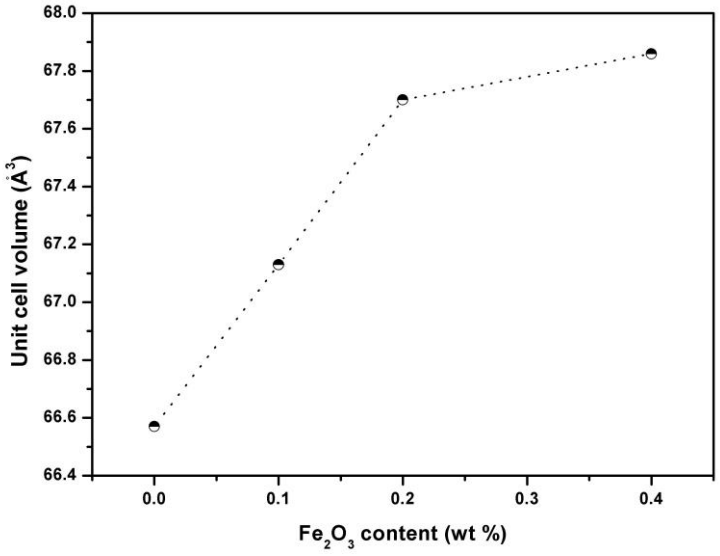


Figure 4.18 – Tetragonal unit cell volume versus $Fe_2O_3$ content (wt %).

### 4.3.2. Microstructural Analysis

The microstructure of a sintering ceramic plays an important role in determining its physical and mechanical properties. The control of the microstructure is therefore fundamental to successful ceramic fabrication. Figure 4.19 shows the SEM micrographs of sintered samples, after a surface polishing (see Table 3.2) and thermal etching. By the analysis of Figure 4.19, it is possible to visualize an uniform microstructure whereas some residual porosity is still present. No second phase of $Fe_2O_3$ was observed and the dark zones are caused by the presence of $Al_2O_3$, which was proved by EDXA analysis (discussed later on).

The grain size was measured by the stereology's interception line method. The Figure 4.20 shows the grain size as function of $Fe_2O_3$. As it can be seen, there is a slight tendency for a decrease in grain size with dopant addition, despite the values are within the measurement error .These results are in agreement with Guo and Xiao study [12] that reported that the $Fe_2O_3$ doping did not affect the grain size of tetragonal zirconia.

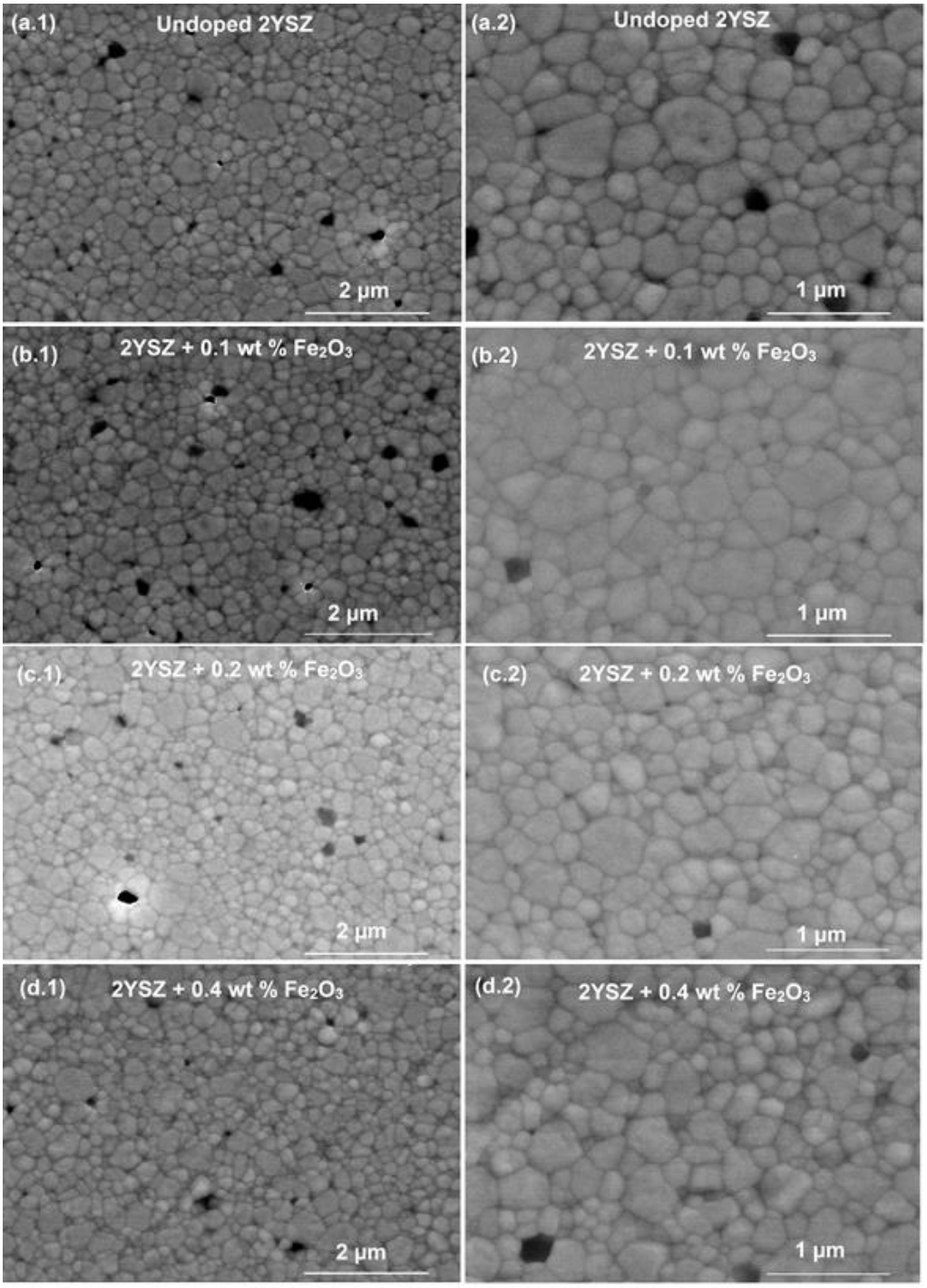


Figure 4.19 - SEM micrographs of (a.1- a.2) undoped 2YSZ, (b.1 - b2) 2YSZ + 0.1 wt. % of $Fe_2O_3$, (c.1 -c.2) 2YSZ + 0.2 wt. % of $Fe_2O_3$ and (d.1 - d.2) 2YSZ + 0.4. wt % of $Fe_2O_3$. Magnifications of 30000 and 15000, respectively. 15 kV of acceleration electron beam.

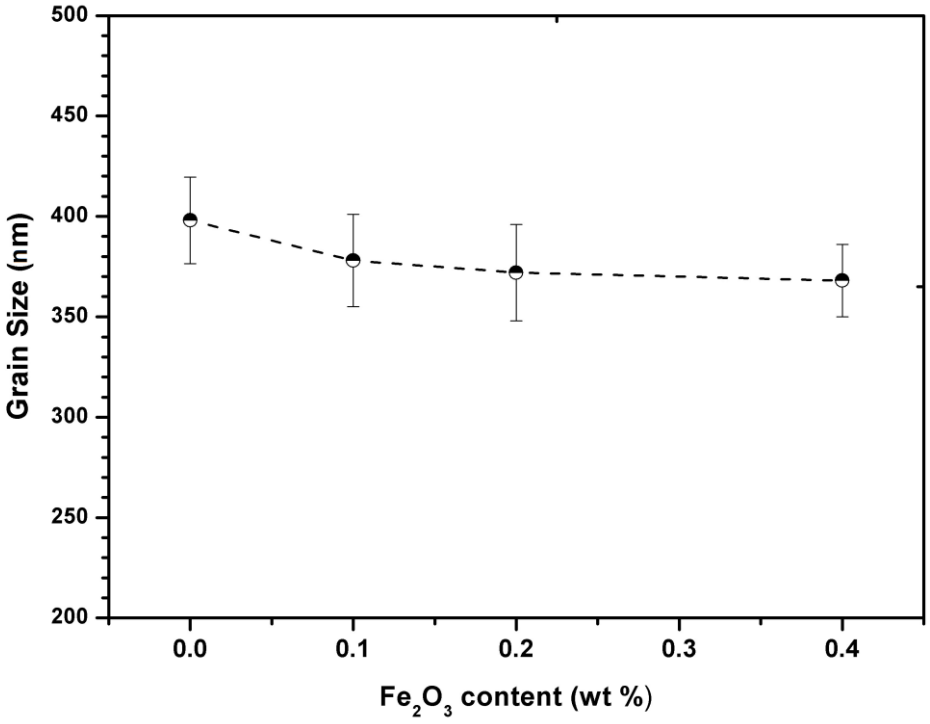


Figure 4.20 – Grain size versus dopant content.

The density before and after sintering was recorded as it can be seen from Table 4.6. The green density of all samples is nearly identical ~2.70 g/cm$^3$ as well as the sintered density ~5.99 g/cm$^3$ measured by Archimedes' principle.

The theoretical density of the monoclinic phase was considered as a constant value of 5.817 g/cm$^3$ since no lattice parameters were determined. The theoretical density of the tetragonal phase was determined using the lattice parameters calculated by Rietveld Refinement, as explained on the Chapter 3. It must be referred that the final theoretical density of each sample was calculated using the mixture rule.

High values of relative density were achieved (> 96 %) and these results are very important since higher densification lead to better mechanical properties, as it will be discussed in detail later on Section 4.3.6. Furthermore, the powders were compacted by uniaxial pressing, without organic binders addition which can result in defects during pressing stage, reflecting in lower values of density. Besides that, the theoretical density was calculated not assuming the content of $Al_2O_3$ detected by FRX which theoretical density is lower (~3.94 g/cm$^3$). It must be mentioned that one of INNOVNANO's requirements to be fulfilled was the sintered density (>6.00 g/cm$^3$). Indeed, the values obtained are slightly lower.

Nevertheless, these values can be improved by additional pressing stages, such as Cold Isostatic Pressing (CIP) or Hot Isostatic Pressing (HIP).

Table 4.6 – Density values of all compositions. STD denotes standard deviation.

| **Composition** | **Green density ($g/cm^3$) ± STD** | **Sintered density ($g/cm^3$) ± STD** | **Theoretical density ($g/cm^3$)** | **Relative density (%)** |
|---|---|---|---|---|
| **Undoped 2YSZ** | 2.67 ± 0.04 | 5.99 ± 0.01 | 6.23 | 96.15 |
| **2YSZ + 0.1 wt. % $Fe_2O_3$** | 2.70 ± 0.03 | 5.99 ± 0.02 | 6.16 | 97.24 |
| **2YSZ + 0.2 wt. % $Fe_2O_3$** | 2.71 ± 0.07 | 5.96 ± 0.01 | 6.13 | 97.88 |
| **2YSZ + 0.4 wt. % $Fe_2O_3$** | 2.73 ± 0.06 | 5.97 ± 0.03 | 6.11 | 97.71 |

SEM-EDXA elemental mapping in the surface of 2YSZ + 0.4 wt. % of $Fe_2O_3$ sample was performed in order to investigate the composition and the spatial distribution of the elements in the zirconia matrix. The Figure 4.21 shows the SEM micrograph of the area under study (a), the overlaid SEM-EDXA maps (b) and the individual maps of zirconium (c), aluminium (d), iron (e), yttrium (f) and hafnium (g). All the elements are well dispersed, except aluminium, since strong intensity points (in blue) were found. The absence of dark blue, green and purple strong intense points in the individual maps indicates that the other elements as yttrium, iron and hafnium are well dispersed in zirconia lattice. Attached to the semi-quantitative EDXA mapping, the chemical composition is also presented. It must be emphasized that despite this sample contains the higher dopant concentration, only a small quantity (0.13 wt. %) of iron was given by the semi-quantitative EDXA analysis. However, it must be noted that the same analysis was also performed on an undoped sample and the presence of iron was not detected.

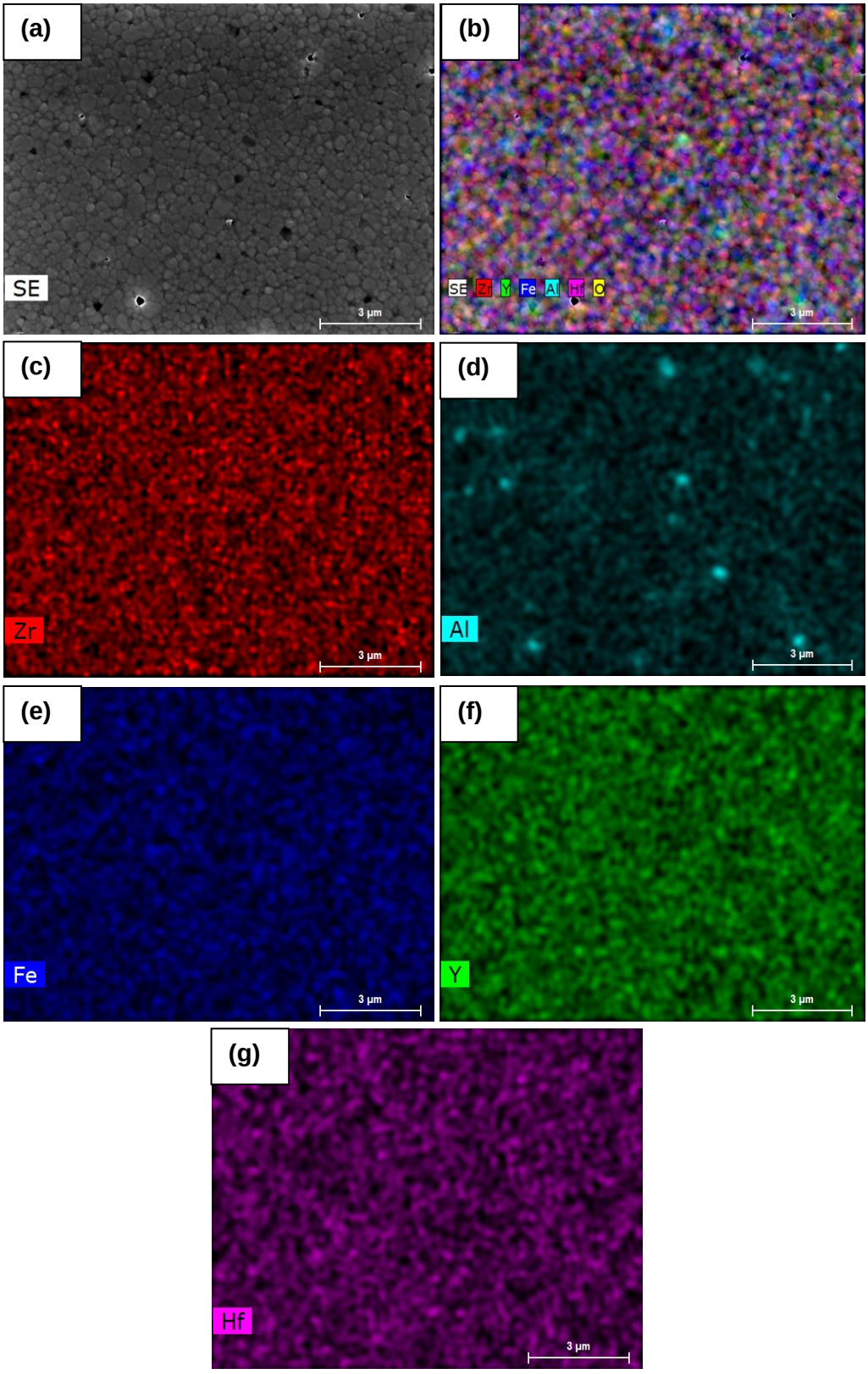


Figure 4.21 - SEM – EDXA maps of the sample 2YSZ + 0.4 wt % of $Fe_2O_3$ and the analysed area micrograph.

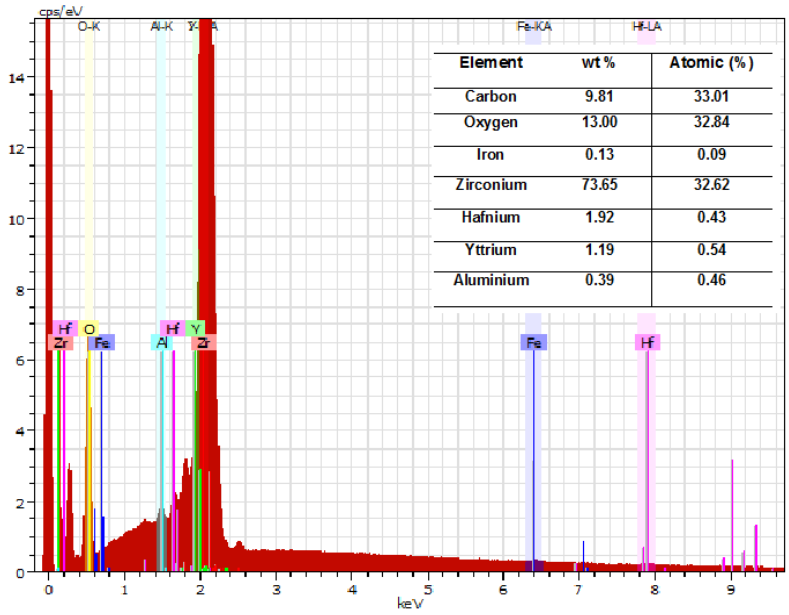


Figure 4.22 - EDXA spectra performed on the 2YSZ doped with 0.4 wt. % of $Fe_2O_3$ and the corresponding semi-quantitative EDXA analysis.

### 4.3.3. Micro Raman Spectroscopy

In order to fully characterize the sintered samples from the structural point of view, Micro Raman Spectroscopy was performed simultaneously with XRD diffraction technique. The Raman spectra were recorded under 442 nm wavelength laser excitation source on the surface of unpolished and polished samples. Besides that, the cross-section of samples that were subjected to flexural strength test was also evaluated.

The Figure 4.23 exhibits the spectra obtained on polished surfaces of 2YSZ with different dopant contents. Raman active modes follow the expected behaviour for the tetragonal crystalline phase around 148, 260, 324, 464, 606, and 637 $cm^{-1}$ assigned to the $E_g$, $A_{1g}$, $B_{1g}$, $E_g$, $B_{1g}$ and $E_g$ symmetries, respectively. Only tetragonal phase was detected on polished surfaces and no significant differences were observed in the Raman spectra with an increase of $Fe_2O_3$.

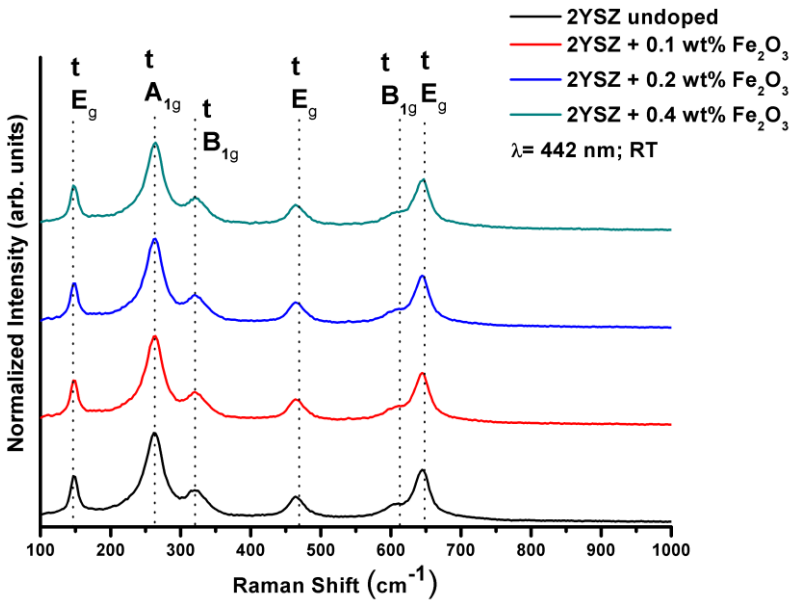


Figure 4.23 - Raman spectra obtained in backscattering configuration of sintered samples polished surface under 442 nm laser excitation source. t denotes tetragonal phase.

Analysing the spectra recorded on the cross-section of the samples that were fractured (Figure 4.24), the monoclinic phase was detected by Raman spectroscopy. The samples were found to exhibit a multiphasic nature comprising the monoclinic and tetragonal zirconia polymorphs once the same tetragonal bands identified above were found in the cross-section region. Furthermore, Raman actives modes of the monoclinic phase around 177 and 381 $cm^{-1}$ assigned to $A_g$ and $B_g$ symmetries were detected. The appearance of these monoclinic bands in the spectra is attributed to the phase transformation during mechanical loading that occurs during fracture process, as explained on the Chapter 2. Tetragonal grains start to transform in the presence of a stress and this can justify the monoclinic signal obtained.

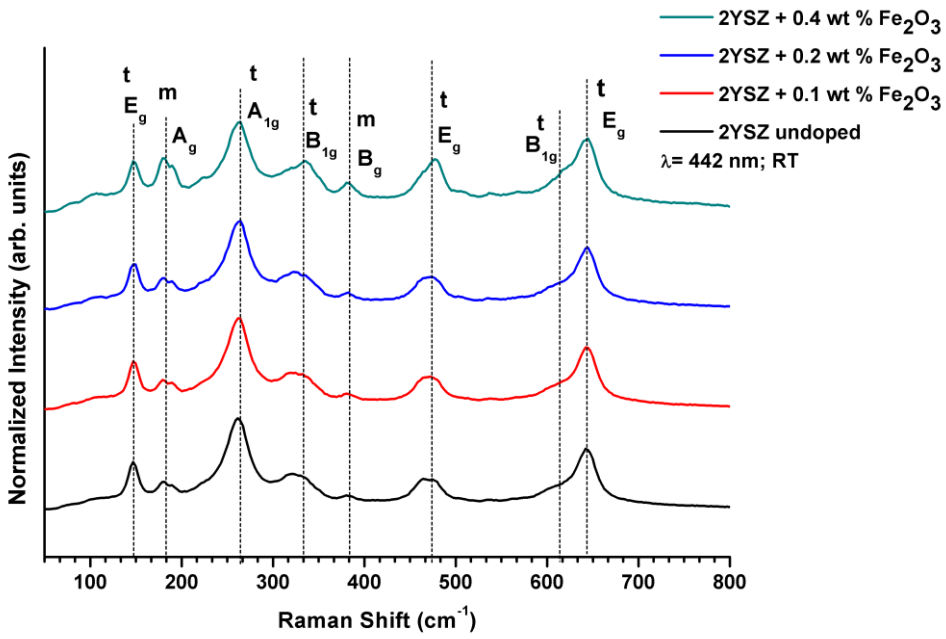


Figure 4.24 - Raman spectra obtained in backscattering configuration on the cross-section produced samples with different contents of dopant under 442 nm laser excitation source. Note: m-monoclinic and t-tetragonal.

Figure 4.25 displays the Raman spectra recorded on polished, unpolished and cross-section surfaces of a sintered sample. The monoclinic phase was detected notoriously on cross-section surface and only a scarcity on the unpolished surface. As previously explained, the presence of the monoclinic phase on the cross-section surface indicates that the tetragonal zirconia, due to its metastability, has been transformed to the more stable phase caused by a mechanical stress. Moreover, the presence of monoclinic phase on the unpolished surfaces was already verified in the reference material characterization and, as explained previously, its presence is commonly reported since surface metastable tetragonal grains are not constrained by the matrix and can transform to monoclinic spontaneously on the surface [1]. Besides that and as explained before, according to Deville and co-workers [61], when a defect is created at the surface, it leaves a homogeneous stress state in its surroundings. The areas affected by these stresses will later transform into zirconia stable polymorph. The presence of these defects, has, therefore, an extremely damaging influence on the ageing sensitivity, as they act as nucleating agents and accelerate surface degradation. According to their study, monoclinic spots nucleates preferentially along these defects/scratches. In fact, during polishing, surface defects, where monoclinic phase is predominantly presented, are eliminated due to abrasive

stresses [61]. Indeed, only tetragonal Raman active modes of tetragonal phase were detected on the polished surfaces meaning that polishing did not induce phase transformation from metastable tetragonal to monoclinic phase.

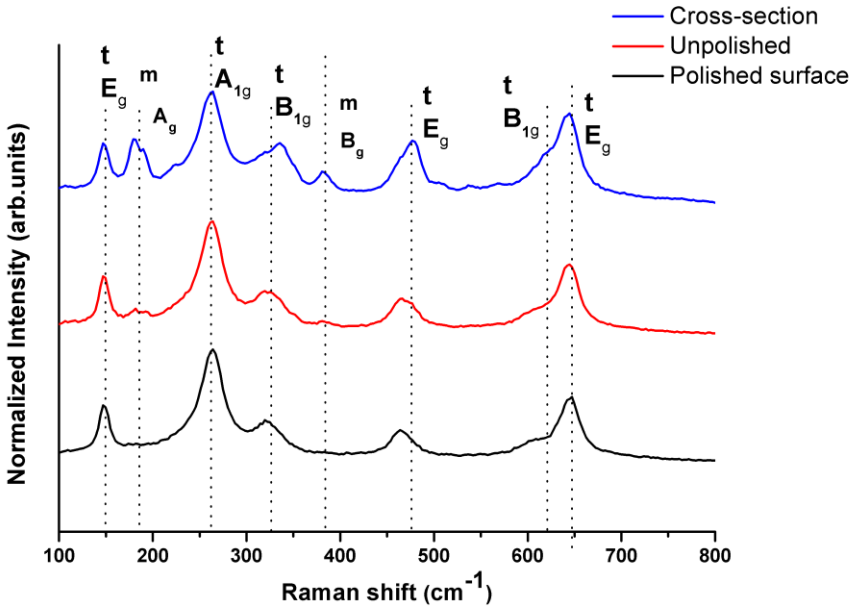


Figure 4.25 - Raman spectra obtained in backscattering configuration of the cross-section, polished and unpolished surfaces of the sample 2YSZ + 0.4 wt % $Fe_2O_3$ under 442 nm laser excitation source. m and t denote monoclinic and tetragonal phase, respectively.

An unpolished surface of 2YSZ doped with 0.4 wt. % $Fe_2O_3$ was studied using Raman mapping in order to investigate the phase distribution on the sample surface, before polishing. The construction of the Raman map (Figure 4.26) followed the same procedure explained on the Chapter of reference material characterization (see Chapter 4.1). For the formation of these Raman images were used the peaks intensity corresponding to each phase, getting the images in Figure 4.26 (b.1) and (b.2) monoclinic phase and (b.3) for the tetragonal. These results are in agreement with the previously visualized on the reference material surface, since both phases are coexistent, despite the tetragonal phase being the most predominant. Optical observation (Figure 4.26 (a)) allowed to clearly identify a monoclinic region, usually presented as a depressed area. Again, the surface detects are extremely favourable for phase transformation, thereby monoclinic spots nucleates preferentially along these defects/scratches, as verified previously.

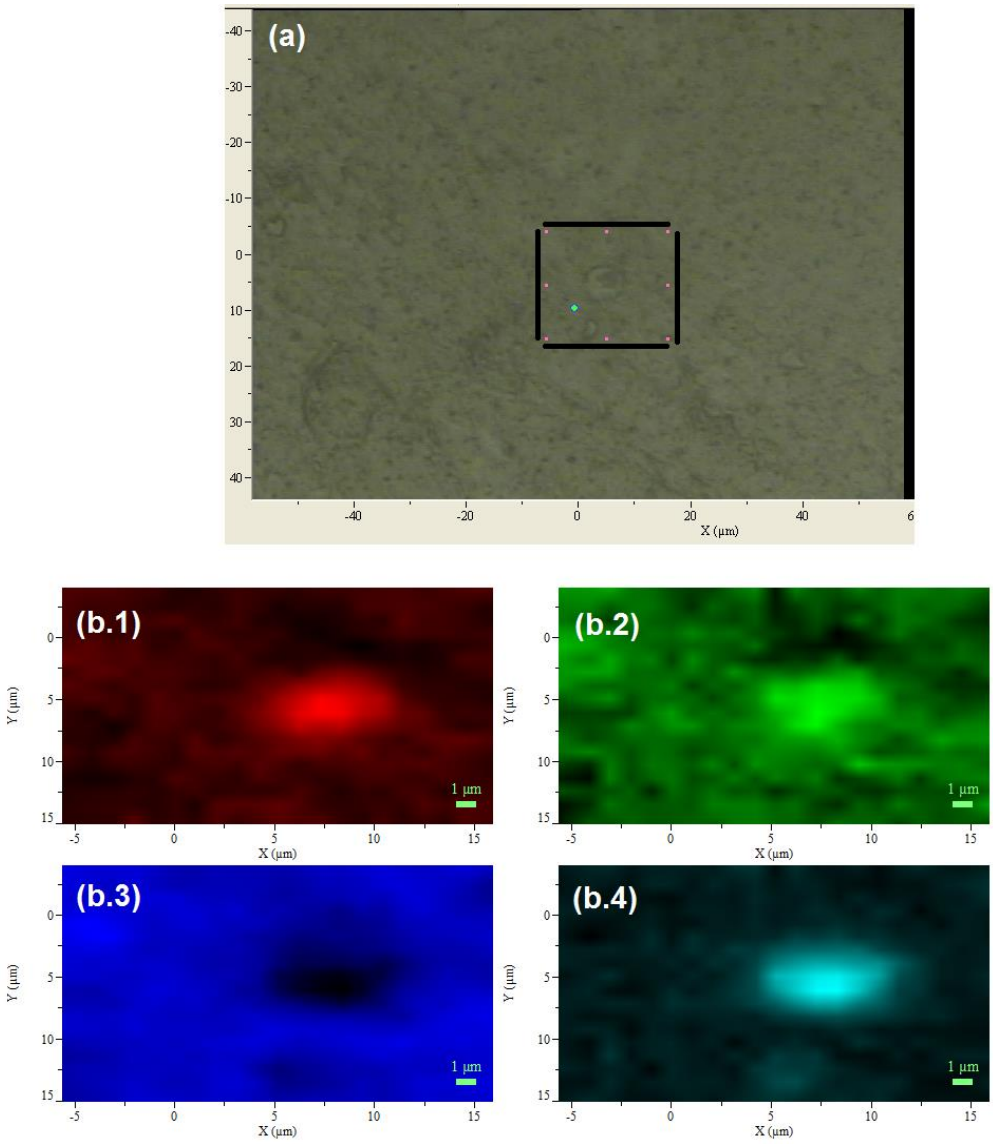


Figure 4.26 - (a) Optical image of the sample surface region under study. Raman maps of (b.1) – (b.2) monoclinic peaks, (b.3) tetragonal peak and (b.4) monoclinic/tetragonal peak intensity ratio.

### 4.3.4. X-ray Photoelectron Spectroscopy (XPS)

XPS is a surface analysis technique (~4nm of analysis depth) that was used to investigate the ionic states of iron on the sample of 2YSZ doped with 0.4 wt.% of $Fe_2O_3$. The wide range spectrum is presented in Figure 4.27, where zirconium, yttrium and iron were detected as well as some contaminants as carbon, silicon, nitrogen and sodium.

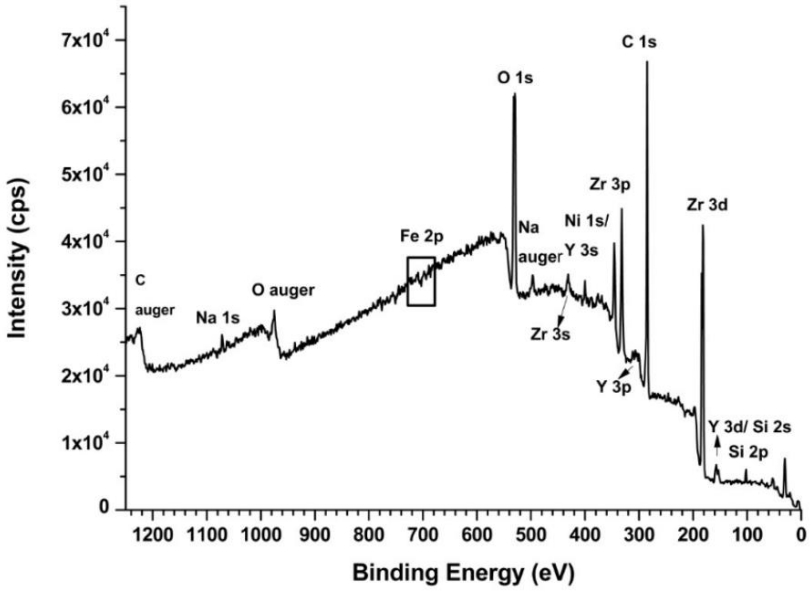


Figure 4.27 – XPS overview spectrum of 2YSZ + 0.4 wt % $Fe_2O_3$ sample.

Focusing now on the electronic state of Fe, a high-resolution spectrum was recorded. The Fe2p signal was splitted into 2 main components, $Fe2p_{3/2}$ (710 eV) and $Fe2p_{1/2}$ (723 eV) as illustrated in Figure 4.28. The Fe2p spectrum was fitted and the fitting parameters are summarized in Table 4.7, based on XPS database [70]. The presence of a mixed valence state of iron cations ($Fe^{2+}/Fe^{3+}$) was detected. However, the Fe2p spectrum revealed that the trivalent iron ($Fe^{3+}$) is predominant whereas only a small quantity of $Fe^{2+}$ was detected.

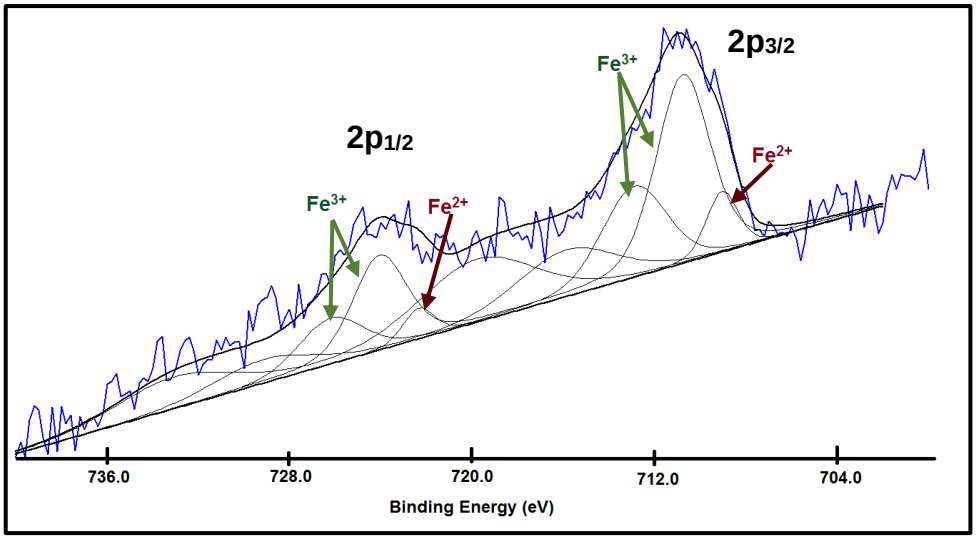


Figure 4.28 – XPS spectrum of Fe2p region.

Table 4.7 – The fitting parameters for the Fe2p part of the XPS Fe signal.

| Component | BE (eV) | FWHM | L/G %* |
|---|---|---|---|
| 1 | 710.76 | 2.80 | 30 |
| 2 | 712.90 | 3.34 | 20 |
| 3 | 715.80 | 5.09 | 20 |
| 4 | 719.78 | 6.00 | 20 |
| 5 | 709.05 | 1.62 | 20 |

***** The L/G denotes the Lorentzian – Gaussian function (%) used to fit the spectra

### 4.3.5. Diffuse Reflectance and Colour

The light reflected of a colour indicates the amount of visible light that a colour will reflect. Therefore, the reflectance spectra of the reference material (non-thermally treated) as well as of the produced samples were measured as illustrated in Figure 4.29.

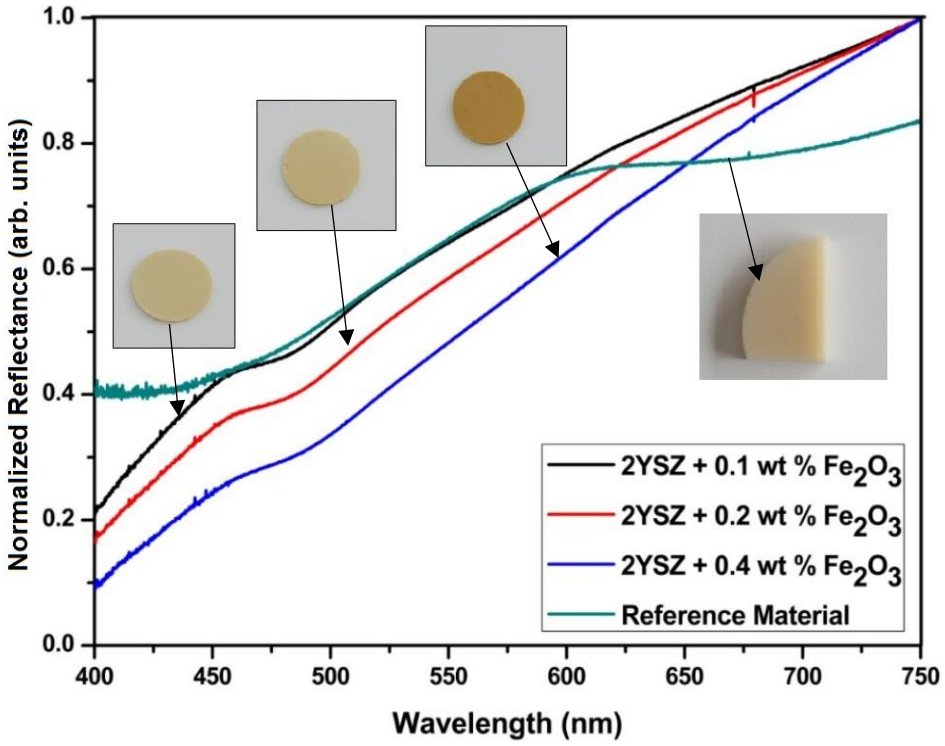


Figure 4.29 - Normalized reflectance versus wavelength (nm) for the reference material and the sintered samples with different contents of $Fe_2O_3$.

Based on X, Y and Z tristimulus values determined from the reflectance spectra, the chromaticity coordinates (x,y) were determined and represented in the CIE 1931 colour space (Figure 4.30). The addition of $Fe_2O_3$ successfully changed the material colour from white to yellowish-brown, as it can be seen from the colour chromaticity diagram. The colour is darker with an increase of $Fe_2O_3$ content, in agreement with the results of reflectance spectra and therefore, with the colour coordinates assessed. The results showed that the colour of the sample doped with 0.1 wt. % of $Fe_2O_3$ was almost identical to the reference material colour.

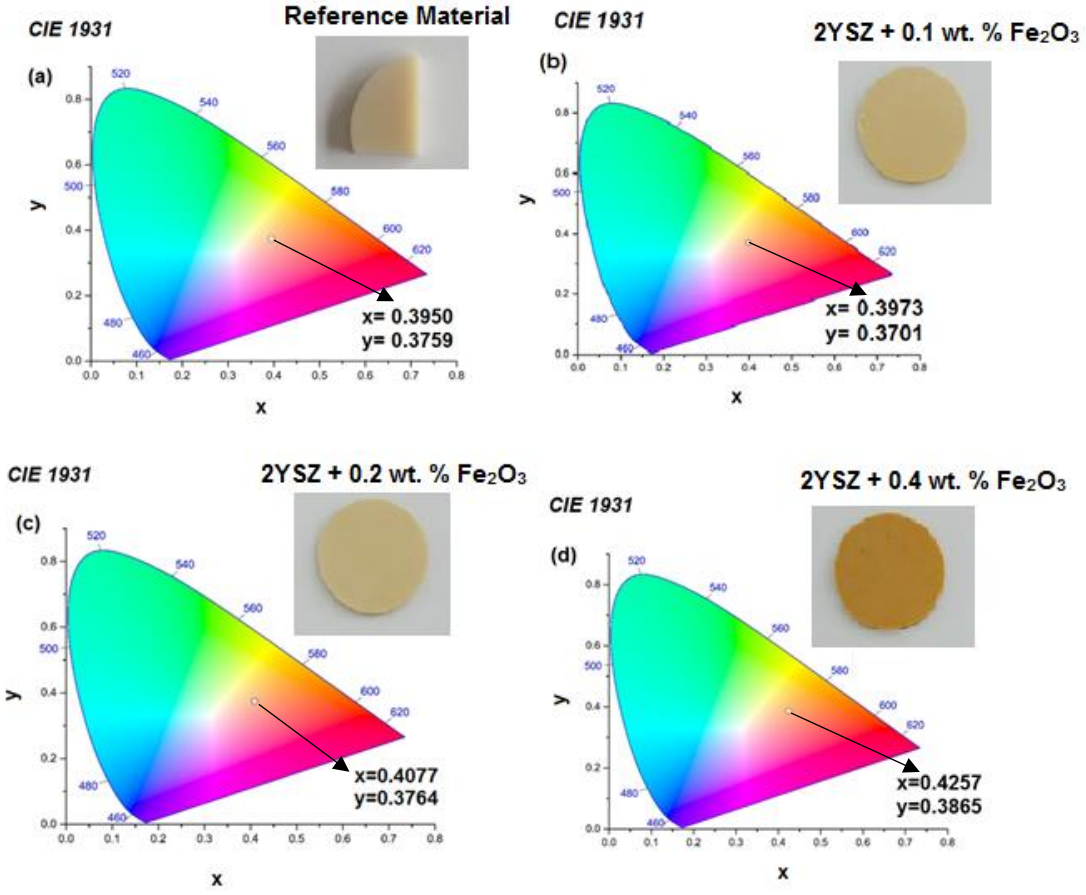


Figure 4.30 - Colour chromaticity diagram of the (a) reference material, (b) 2YSZ + 0.1 wt. % $Fe_2O_3$, (c) 2YSZ + 0.2 wt. % $Fe_2O_3$, (d) 2YSZ + 0.4 wt. % $Fe_2O_3$.

In order to guarantee that colour induced by the addition of iron oxide does not change after annealing, as it was observed in the reference material, the same thermal treatment in air performed to the reference material was made in the sintered samples. Figure 4.31 (a-b)

shows the digital photographs of the doped samples before and after thermal treatment. As it can be seen, no significant changes in the samples colour was observed. Hence, the colour is not compromised when the samples are thermally treated in an oxidizing atmosphere, in opposition to the one observed in the reference material.

In addition, in order to investigate the colour stability in reducing conditions an annealing in a reduced atmosphere (10 % $H_2$ – 90 % $N_2$, maximum temperature of 1200 ºC, dwell time of 4 hours, oxygen partial pressure ($pO_2$= $10^{-21}$ atm)) was also performed. No changes were observed in colour (Figure 4.31) after annealing, revealing the chromatic stability of this mechanism of colouring zirconia under a reduced atmosphere.

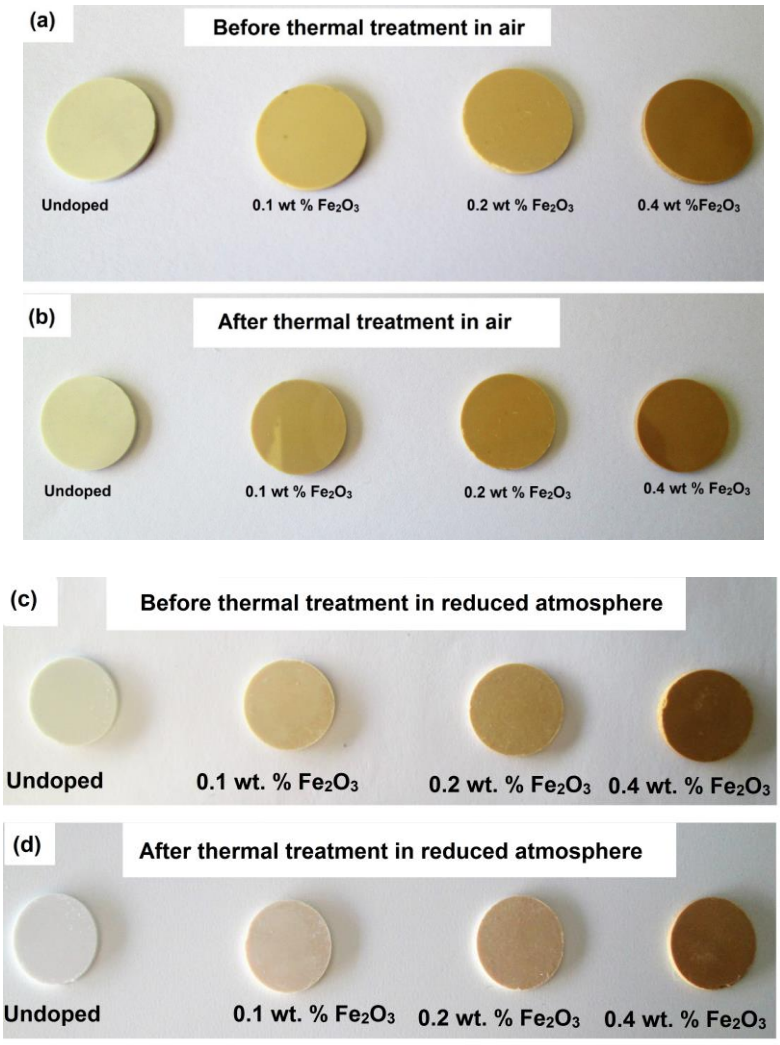


Figure 4.31- Digital photographs of the sintered samples after and before annealing in: (a-b) oxidizing atmosphere (air) and (c-d) in reduced atmosphere.

From these results, we can assume that $Fe_2O_3$ doping is a controllable and irreversible way of colouring zirconia, allowing to work under more extremely conditions and under different range of temperatures, being favourable for prospective high-temperature applications.

### 4.3.6. Photoluminescence

The photoluminescence study @ 442 nm on sintered samples revealed the same emission bands at 693 and 694 nm observed on the reference material, as illustrated on Figure 4.32. As mentioned before, these bands can be assigned to trace amounts of $Cr^{3+}$ once this emission is attributed to the characteristic luminescence of $Cr^{3+}$ in α-$Al_2O_3$ [64]. In fact, the presence of $Al_2O_3$ was also detected on the FRX analysis, as previously presented.

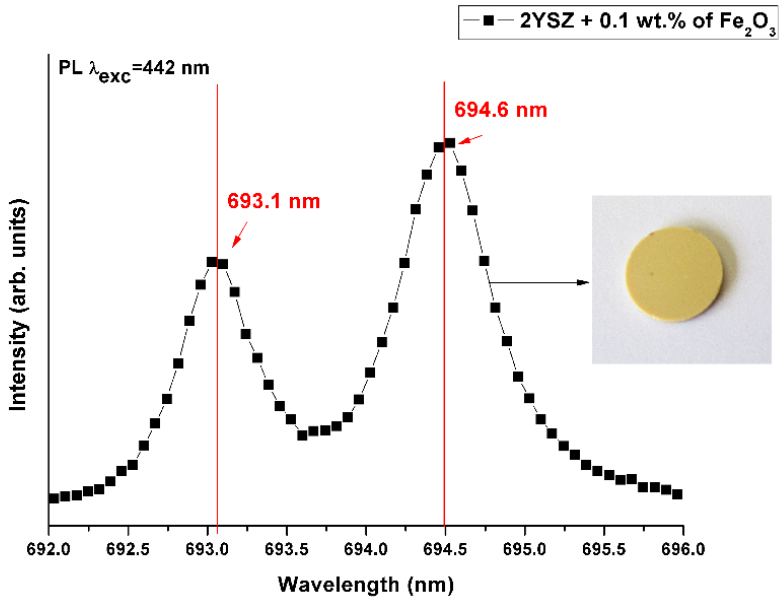


Figure 4.32 – PL emission spectra under 442 nm of reference material before and after thermal treatment and of a sintered sample of 2YSZ + 0.1 wt % $Fe_2O_3$.

These results suggested that *beige* colour can be achieved on 2YSZ materials by different mechanisms including intrinsic defect such as colours centers and extrinsic defects ($Fe_2O_3$ doping).

### 4.3.7. Mechanical Analysis

Zirconia ceramic is noteworthy for its high strength and fracture toughness, and therefore is used in several applications that require excellent mechanical behaviour. In the previous section, it has been unequivocally demonstrated that the addition of iron oxide allows to confer the desired *beige* colour. However, it is now necessary to prove that the addition of iron oxide did not affect its mechanical properties. That way, the mechanical properties could not be neglected and minimum requirements were defined to be fulfilled, such as:

- Biaxial flexural strength (MPa): 1000-1200
- Fracture toughness (MPa.$m^{0.5}$): > 8
- Hardness, HV10 (MPa): > 1200

To assess the mechanical properties of the sintered samples, fracture toughness (Palmqvist method) and hardness (HV10) were calculated using a micro-indentation system with a Vickers tip as well as flexural strength (piston-on-three-ball arrangement).

The effect of $Fe_2O_3$ addition and grain size on the fracture toughness of 2YSZ samples sintered at 1350 ºC is shown in Table 4.8. This table also contains the amount of tetragonal phase present in the samples that were subjected to fracture toughness measurements. The measurements were performed on the polished surfaces since tetragonal phase is the major constituent irrespective of the original surface conditions (samples as sintered). As seen in the table, all the samples are mostly constituted by tetragonal phase (>92 %) and the higher value of fracture toughness (9.8 MPa.$m^{0.5}$) was found in the undoped samples. In fact, the transformation toughening mechanism is influenced by the phase stability of the t-grains and the fracture toughness can be used as an indicator of tetragonal phase stability in the zirconia matrix. If a higher amount of metastable tetragonal phase is presented and the material is subjected to a mechanical stress, more tetragonal grains will transform into monoclinic phase. This transition is followed by a volumetric expansion (~5 %) which generate a compressive stress field around the crack, resulting in an improvement of fracture toughness. In general, to maximize material toughness, the fraction of transformable tetragonal phase should be optimized. In case of doped samples, the fracture toughness is lower (7.8 MPa. $m^{0.5}$), suggesting that $Fe^{3+}$ stabilizes the tetragonal phase reducing the fraction of transformable tetragonal phase and consequently results in a decrease of fracture toughness. However, it was previously suggested by the XRD analysis, that $Fe^{3+}$ occupies interstitials positions in the tetragonal lattice. Indeed, in the current work, the position of $Fe^{3+}$ is still an open question. As mentioned before, the dopant content is very low and the effect of this dopant in zirconia stabilization is unclear.

Additional factors can affect the fracture toughness such as the grain size. Basu [5] reported that the fracture toughness increases along with grain size. However, since minor variations were observed in the grain size it is unclear its effect on the fracture toughness. Moreover, slightly lower values of fracture toughness were attained in the doped samples (< 8 MPa.m$^{0.5}$) where the grain size and the amount of tetragonal phase are slightly lower than in the undoped one.

The values of hardness (HV10) achieved are also shown in the Table 4.8. As previously mentioned, a higher amount of tetragonal phase contributed to a higher mechanical strength. The surface phase transition and the consequent surface hardening have a relevant role on the mechanical properties. The highest value of HV10 was found for the undoped sample which contained a higher amount of tetragonal phase (~97 %), as determined by X-ray analysis. Furthermore, no linear correlation was found between the hardness and the dopant content, but the values of hardness obtained for all composition (> 1200 MPa) are superior to the one required by INNOVNANO.

Table 4.8 – Physical and mechanical properties of the sintered samples. STD denotes standard deviation.

| **Composition** | **Grain Size ± STD (nm)** | **t-phase (%)** | **Relative density (%)** | **$K_{IC}$ (MPa.m$^{0.5}$) ± STD** | **HV10 (MPa) ± STD** | **$\sigma_{flexural}$ (MPa) ± STD** |
|---|---|---|---|---|---|---|
| **Undoped 2YSZ** | 398 ± 19 | 96.74 | 96.15 | 9.8 ± 0.87 | 1235 ± 18 | 1050 ±125 |
| **2YSZ + 0.1 wt. % $Fe_2O_3$** | 378 ± 23 | 92.42 | 97.24 | 7.78 ± 0.45 | 1225 ±10 | 1070 ± 118 |
| **2YSZ + 0.2 wt. % $Fe_2O_3$** | 372 ± 24 | 93.18 | 97.88 | 7.71 ± 0.51 | 1226 ± 11 | 853 ± 131 |
| **2YSZ + 0.4 wt. % $Fe_2O_3$** | 368 ± 18 | 94.20 | 97.71 | 7.88 ± 0.62 | 1213 ± 18 | 1136 ± 97 |

The flexural strength ($\sigma_{flexural}$) values are also shown in the Table 4.8. High values of flexural strength were achieved (>1000 MPa) for all samples except for the one containing 0.2 wt. % of $Fe_2O_3$. As previous discussed, the powder of this composition presented a broad particle size distribution which can justify the lower value of flexural strength obtained (853 MPa). Besides that, it should be also noted that some defects were created during pressing stage and these defects also negatively affect ceramic density and consequently the flexural strength. Nevertheless, the addition of organics binders during powders manufacturing could be an alternative to improve the final mechanical properties of sintered zirconia ceramics. However, it is important to highlight that the other compositions presented high values of flexural strength (> 1000 MPa) in agreement with literature data and with INNOVNANO's standards.

In general, according to these results we can assume that the hardness (HV10) and the biaxial flexure strength were not significantly affected by dopant addition and high values were attained in accordance with the high amount of tetragonal phase (>92 %) and high relative density (>96 %). Although, it was found that $Fe_2O_3$ doping slightly decreased the fracture toughness of 2YSZ ceramics. However, these mechanical properties could be still improved by additional pressing stages, namely, CIP (cold isostatic pressing) or using sintering routes different from traditional ones, like HIP (hot isostatic pressing). Nevertheless, the mechanical properties of the investigated samples fulfilled the INNOVNANO's standard requirements.

# CHAPTER 5

## 5. Conclusion and Future Work

## 5.1. Conclusions

The conclusions and the main findings of this work are summarized in the next topics:

- The reference material provided by a INNOVNANO's client was mostly constituted by tetragonal zirconia and only monoclinic phase was detected before polishing meaning that the zirconia phase distribution on the surface is dependent on the superficial treatments such as polishing. Raman spectroscopy allowed to conclude that metastable tetragonal zirconia transformed to monoclinic phase preferentially on the surface defects due to surroundings stresses;

- The results suggest that the original *beige* colour of the reference material was due to intrinsic defects, namely, colour centers produced under reduced conditions. This way of colouring zirconia, besides being non-permanent (temperature sensitive), is not very controllable since it is difficult to reproduce the same degree of intrinsic defects;

- The addition of $Fe_2O_3$ successfully changed the material colour from white to *beige* and the colour of the sample doped with 0.1 wt. % of $Fe_2O_3$ was almost identical to the reference material colour. This result allow to conclude that doping with $Fe_2O_3$ is a controllable method to tune zirconia ceramics colour;

- Tetragonal lattice parameters were determined by Rietveld refinement, which indicated that the tetragonal unit cell volume increased along dopant content. This result suggests that the $Fe^{3+}$ occupied interstitials positions in 2YSZ structure;

- The same thermal treatments in air as well as in a reducing atmosphere performed on the reference material were made in the produced samples and the colour did not change, demonstrating that $Fe_2O_3$ doping is a suitable, reproducible and irreversible mechanism for colouring zirconia, being favourable for prospective high-temperature applications;

- The effect of low concentrations of $Fe_2O_3$ on the mechanical properties has been investigated. Vickers hardness (HV10) and biaxial flexure strength were not significantly affected by dopant addition and high values were attained in accordance with the high amount of tetragonal phase (>92 %) and high relative density (>96 %). Although, it was found that $Fe_2O_3$ doping slightly decreased the

fracture toughness of 2YSZ ceramics. However, these mechanical properties could still be improved by additional pressing stages such as CIP and HIP. Besides that, the addition of organics binders during powders manufacturing could be an alternative to improve the final mechanical properties of sintered zirconia ceramics. Nevertheless, the mechanical properties of the investigated samples fulfilled the INNOVNANO's standard requirements.

## 5.2. Further Work

The results obtained in this study suggest few aspects for the continuation of this work:

- Low temperature degradation studies to evaluate the long-term stability of tetragonal zirconia doped with iron oxide;
- Development and study of 2YSZ doped with others colourants such as $CeO_2$ and $Bi_2O_3$ for mechanical assessment and possible comparison;
- Study the effect of sintering under inert and reducing atmospheres on the colour centers formation and consequently on the samples colour;
- Perform additional pressing stages as CIP and HIP in order to improve the final mechanical properties as well as the use of the organic binders to reduced defects during pressing stage and consequently improve of mechanical properties.

# REFERENCES


1. Piconi, C. & Maccauro, G. Zirconia as a ceramic biomaterial. *Biomaterials* **20,** 1–25 (1997).

2. Garvie, R. C., Hannink, R. H. & Pascoe, R. T. Ceramic steel? *Nature* **258,** 703–704 (1975).

3. Manicone, P. F., Rossi Iommetti, P. & Raffaelli, L. An overview of zirconia ceramics: Basic properties and clinical applications. *Journal of Dentistry* **35,** 819–826 (2007).

4. F.O.Milovich *et al.* Study of the Structure and Mechanical Properties of PSZ (Partially Stabilized Zirconia) after Heat tratament at 1600ºC. *Proceedings of the International Conference Nanomaterials: Applications and Properties* **2,** 6–9 (2013).

5. Basu, B. Toughening of yttria-stabilised tetragonal zirconia ceramics. *International Materials Reviews* **50,** 239–256 (2005).

6. Chevalier, J. & Gremillard, L. The Tetragonal-Monoclinic Transformation in Zirconia: Lessons Learned and Future Trends. *J. Am. Ceram. Soc.* **1920,** 1901–1920 (2009).

7. Chevalier, J., Gremillard, L. & Deville, S. Low-Temperature Degradation of Zirconia and Implications for Biomedical Implants. *Annu. Rev. Mater. Res.* **37,** 1–32 (2007).

8. Chevalier, J. What future for zirconia as a biomaterial? *Biomaterials* **27,** 535–543 (2006).

9. Denry, I. & Kelly, J. R. State of the art of zirconia for dental applications. *Dent. Mater.* **24,** 299–307 (2008).

10. Wen, N. *et al.* The Color of $Fe_2O_3$ and $Bi_2O_3$ Pigmented Dental Zirconia Ceramic. *Key Eng. Mater.* **435,** 582–585 (2010).

11. Boutz, M. M. R., Winnubst A. J. A., Hartgers F., B. A. J. Effect of additives on densification and deformation of tetragonal zirconia. *J. Mater. Sci.* **29,** (1994).

12. Guo, F. & Xiao, P. Effect of $Fe_2O_3$ doping on sintering of yttria-stabilized zirconia. *J. Eur. Ceram. Soc.* **32,** 4157–4164 (2012).

13. http://www.innovnano.pt/our-powders/. (Accessed: 16th February 2017)

14. http://www.innovnano.pt/our-technology/. (Accessed: 16th February 2017)

15. Materials, A. Creating the Next-Generation of Ceramic Powders – Introducing Emulsion Detonation Synthesis (EDS). http://www.azom.com/article.aspx?ArticleID=13589 (2017).

16. Shah, K., Holloway, J. A. & Denry, I. L. Effect of Coloring with Various Metal Oxides on the Microstructure, Color, and Flexural Strength of 3Y-TZP. *J. Biomed. Mater. Res. - Part B Appl. Biomater.* **87,** 329–337 (2008).

17. Ikeno, H., Krause, M., Thomas, H. & Patzig, C. Variation of Zr-L 2 , 3 XANES in tetravalent zirconium oxides. *J. Phys. Cpndensed Matter* **165505,** (2013).

18. Kisi, E. H. & Howard, C. J. Crystal Structures of Zirconia Phases and their Inter-Relation. *Key Eng.*

*Mater.* **153–154,** 1–36 (1998).

19. Standard, O. C. & Sorrell, C. C. Densification of Zirconia - Conventional Methods. *Key Eng. Mater.* **153–154,** 251–300 (1998).

20. Hjerppe, J. the Influence of Certain Processing Factors on the Durability of Yttrium Stabilized Zirconia Used As Dental Biomaterial. (University of Turku, Finland, 2010).

21. Reckziegel, A. & Ag, F. Technical paper properties and apllications of high-performance ceramics made of zirconia. (2015).

22. Nunes Soares, R. M. Phd Thesis - Development of Zirconia based phospors for application in ligthting and as luminescent bioprobes. (University of Aveiro, 2013).

23. Matsui, K., Nakamura, K., Kumamoto, A., Yoshida, H. & Ikuhara, Y. Low-temperature degradation in yttria-stabilized tetragonal zirconia polycrystal doped with small amounts of alumina: Effect of grain-boundary energy. *J. Eur. Ceram. Soc.* **36,** 155–162 (2016).

24. Kohorst, P. *et al.* Low-temperature degradation of different zirconia ceramics for dental applications. *Acta Biomater.* **8,** 1213–1220 (2012).

25. Fabris, S., Paxton, A. T. & Finnis, M. W. A stabilization mechanism of zirconia based on oxygen vacancies only. *Acta Mater.* **50,** 5171–5178 (2002).

26. Shukla, S. & Seal, S. Mechanisms of room temperature metastable tetragonal phase stabilisation in zirconia. *Int. Mater. Rev.* **50,** 45–64 (2005).

27. Swable, J. J. *Role of Oxide Additives in Stabilizing Zirconia for Coating Applications*. (2001).

28. Scott, H. G. Phase relationships in the zirconia-yttria system. *J. Mater. Sci.* **10,** 1527–1535 (1975).

29. Lange, F. . Transformation toughening - Part 3 - Experimental observations in the $ZrO_2$-$Y_2O_3$ system. *J. Mater. Sci.* **17,** 240–246 (1982).

30. Matsui, K., Yoshida, H. & Ikuhara, Y. Grain-boundary structure and microstructure development mechanism in 2 – 8 mol % yttria-stabilized zirconia polycrystals. *Acta Mater.* **56,** 1315–1325 (2008).

31. Basu, B. & Kantesh, B. *Advanced Structural Ceramics*. 180 (2011).

32. INNOVNANO. Technical Data Sheet Enhanced material properties for physically demanding applications.

33. http://www.ceramicindustry.com/articles/96326-synthesizing-yttria-stabilized-zirconia. (Accessed on 15th April 2017)

34. http://www.innovnano.pt/our-powders-applications-2ysz/.(Accessed on 20th on April)

35. Kelly, J. R. & Denry, I. Stabilized zirconia as a structural ceramic: An overview. *Dent. Mater.* **24,** 289–298 (2008).

36. Bechta, S. V. *et al.* Phase diagram of the $ZrO_2$-FeO system. *J. Nucl. Mater.* **348,** 114–121 (2006).

37. S.E, P. & J, L. Photoluminescence-Spectra Study of Yttria-Stabilized Zirconia. *Applied Physics A* **228,** 225–228 (1993).

38. Zhang, H., Kim, B. & Morita, K. Effect of sintering temperature on optical properties and microstructure of translucent zirconia prepared by high-pressure spark plasma sintering. *Sci. Technol. Adv Mater.* **55003,** (2011).

39. Dermot, G. Photoluminescence and Excitation Studies of Semiconductors School of Physical Sciences. (Dublin University, 2001).

40. García Solé, J, Bausá L.E, J. D. *An Introduction to the Optical Spectroscopy*. **6,** (2005).

41. Torrent, J. & Barrón, V. Diffuse reflectance spectroscopy. *Soil Sci. Soc. Am.* 367–385 (2008).

42. Blum, P. *Reflectance Spectrophotometry and colorimetry*. **10,** (1997).

43. Vigário, C. Tese de mestrado: Estudo , desenvolvimento e implementação de soluções de medida para irradiância, absoluta relativa e de cor . (Departamento de Física, Universidade de Aveiro, 2016).

44. X-rite. Color Guide and Glossary - Communication measurement and control for digital imaging and graphic arts. 1–52 (2013).

45. Hoffman, G. CIE Color Space. *Brain* 1–30 (2000).

46. Lopes, A. Lessons: Material Characterization II -X-ray Diffraction. 1–34 (2016).

47. Colthup, N., Lawrence, D. & Wiberley, S. *Introduction to infrared and Raman spectroscopy*. *Spectrochimica Acta Part A: Molecular Spectroscopy* **47,** (Academic Press, Inc., 1991).

48. Bumbrah, G. S. & Sharma, R. M. Raman spectroscopy: Basic principle, instrumentation and selected applications for the characterization of drugs of abuse. *Egypt. J. Forensic Sci.* **6,** 209–215 (2016).

49. Queraltó, A. *et al.* Ultrafast Epitaxial Growth of Functional Oxide Thin Films by Pulsed Laser Annealing of Chemical Solutions. *Chem. Mater.* (2016).

50. http://www.vma-getzmann.com/bead_mill_dispermat_sl (Acessed on 10th March 2017)

51. http://www.lagep.cpe.fr/wwwlagep7/en/2013/10/. (Accessed: 15th March 2017)

52. More Swati, K. & Wagh, M. P. Review on Spray Drying Technology. *Int. J. Pharm. Chem. Biol. Sci.* **4,** 219–225 (2014).

53. http://www.malvern.com/en/products/technology/laser-diffraction/. (Accessed: 22nd March 2017)

54. http://archaeometry.missouri.edu/xrf_overview.html. (Accessed: 25th March 2017)

55. Zhou, W., Apkarian, R. P. & Wang, Z. L. Fundamentals of Scanning Electron Microscopy. *Scanning Microsc. Nanotechnol.* 1–40 (2007).

56. C.D, W., Riggs, W. ., Davies, L. ., J.F, M. & Muilenberg, G. . *Hanbook of X-ray photoelectron spectroscopy*. (Perkin-Elmer Corporation, 1979).

57. http://www.twi-global.com/technical-knowledge/job-knowledge/hardness-testing-part-1-074/.

(Accessed on 10th April 2017)

58. Niihara, K., Morena, R. & Hasselman, D. Evaluation of fracture toughness of britlle solids by the indentation method with low crack-to-indent ratios. *J. Mater. Sci. Lett.* **1,** 13–16 (1982).

59. https://en.wikipedia.org/wiki/Palmqvist_method (Accessed on 20th May 2017)

60. Zhao, X. & Vanderbilt, D. First-principles study of structural, vibrational and lattice dielectric properties of hafnium oxide. **8019,** (2002).

61. Deville, S., Chevalier, J. & Gremillard, L. Influence of surface finish and residual stresses on the ageing sensitivity of biomedical grade zirconia. *Biomaterials* **27,** 2186–2192 (2006).

62. Nakajima, H. & Mori, T. Photoluminescence excitation bands corresponding to defect states due to oxygen vacancies in yttria-stabilized zirconia. *Solid State Communications* **412,** 728–731 (2006).

63. Wachsman, E. D., Jiang, N., Frank, C. W., Mason, D. M. & Stevenson, D. A. Spectroscopy Investigation of Oxygen Vancancies in Solid Oxide Electrolytes. *Appl. Phys. A* **549,** 545–549 (1990).

64. Liu, D., Lord, O., Stevens, O. & Flewitt, P. E. J. The role of beam dispersion in Raman and photo-stimulated luminescence piezo-spectroscopy of yttria-stabilized zirconia in multi-layered coatings. *Acta Mater.* **61,** 12–21 (2013).

65. Yu, H. & Clarke, D. R. Effect of Codoping on the R-Line Luminescence of $Cr^{3+}$-Doped Alumina. *J. Am. Ceram. Soc.* **85,** 1966–1970 (2002).

66. Jonghe, L. C. De & Rahaman, M. N. in *Handbook of Advanced Ceramics* (2003).

67. Pyda, W. Theory and Practice of Ceramic Processes. (2011).

68. Li, J., Tang, Z., Zhang, Z. & Luo, S. Study of factors influencing the microstructure and phase content of ultrafine Y-TZP. *Mater. Sci. Eng. B Solid-State Mater. Adv. Technol.* **99,** 321–324 (2003).

69. Zhao, J., Shen, Z., Si, W. & Wang, X. Bi-colored zirconia as dental restoration ceramics. *Ceram. Int.* 1–7 (2013). doi:10.1016/j.ceramint.2013.05.036

70. https://srdata.nist.gov/xps/ElmSpectralSrch.aspx?selEnergy=PE (Acessed on 2nd June 2017)

# Appendix A

**00-037-1484** Jul 20, 2017 3:52 PM (Metoxidid Oxidos)

**Status** Primary **QM:** Star **Pressure/Temperature:** Ambient **Chemical Formula:** Zr O2
**Empirical Formula:** O2 Zr **Weight %:** O25.97 Zr74.03 **Atomic %:** O66.67 Zr33.33
**Compound Name:** Zirconium Oxide **Mineral Name:** Baddeleyite, syn
**Common Name:** zirconia, zirconium dioxide, zirkite

**Radiation:** CuKα1 **λ:** 1.5406 Å **Filter:** Graph Mono **d-Spacing:** Diff. **Cutoff:** 17.70
**Intensity:** Diffractometer **I/Ic:** 2.6

**SYS:** Monoclinic **SPGR:** P21/a (14)
**Author's Cell [ AuthCell a:** 5.3129(4) Å **AuthCell b:** 5.2125(4) Å **AuthCell c:** 5.1471(5) Å
**AuthCell β:** 99.218(8)° **AuthCell Vol:** 140.70 Å³ **AuthCell Z:** 4.00 **AuthCell MolVol:** 35.17 **]**
**Author's Cell Axial Ratio [ c/a:** 0.969 **a/b:** 1.019 **c/b:** 0.987 **]** **Density [ Dcalc:** 5.817 g/cm³ **]**
**SS/FOM:** F(30) = 111.1(0.0073, 37) **Temp:** 298.5 K (Author provided temperature) **Color:** Colorless

**Space Group:** P21/a (14) **Molecular Weight:** 123.22
**Crystal Data [ XtlCell a:** 5.313 Å **XtlCell b:** 5.213 Å **XtlCell c:** 5.147 Å **XtlCell α:** 90.00°
**XtlCell β:** 99.22° **XtlCell γ:** 90.00° **XtlCell Vol:** 140.70 Å³ **XtlCell Z:** 4.00 **]**
**Crystal Data Axial Ratio [ c/a:** 0.969 **a/b:** 1.019 **c/b:** 0.987 **]**
**Reduced Cell [ RedCell a:** 5.147 Å **RedCell b:** 5.213 Å **RedCell c:** 5.313 Å **RedCell α:** 90.00°
**RedCell β:** 99.22° **RedCell γ:** 90.00° **RedCell Vol:** 140.70 Å³ **]**

**Atomic parameters are cross-referenced from PDF entry 04-010-6452**
**Crystal (Symmetry Allowed):** Centrosymmetric
**SG Symmetry Operators:**

| Seq | Operator | Seq | Operator | Seq | Operator | Seq | Operator |
|---|---|---|---|---|---|---|---|
| 1 | x,y,z | 2 | -x,-y,-z | 3 | -x,y+1/2,-z+1/2 | 4 | x,-y+1/2,z+1/2 |

**Atomic Coordinates:**

| Atom | Num | Wyckoff | Symmetry | x | y | z | SOF | IDP | AET |
|---|---|---|---|---|---|---|---|---|---|
| Zr | 1 | 4e | 1 | 0.2744 | 0.0394 | 0.2084 | 1.0 | | |
| O | 2 | 4e | 1 | 0.0614 | 0.3263 | 0.3404 | 1.0 | | |
| O | 3 | 4e | 1 | 0.4495 | 0.7575 | 0.4757 | 1.0 | | |

**Subfile(s):** Common Phase, Educational Pattern, Forensic, Inorganic, Metals & Alloys, Mineral Related (Mineral , Synthetic), NBS Pattern, Superconducting Material (Superconductor Reaction Product)
**Prototype Structure [Formula Order]:** Zr O2 **Prototype Structure [Alpha Order]:** O2 Zr
**LPF Prototype Structure [Formula Order]:** Zr O2-b,mP12,14
**LPF Prototype Structure [Alpha Order]:** O2 Zr,mP12,14 **Pearson Symbol:** mP12.00
**Cross-Ref PDF #'s:** 00-007-0343 (Alternate), 00-013-0307 (Alternate), 00-036-0420 (Alternate), 04-001-7279 (Alternate), 04-002-0185 (Alternate), 04-002-5420 (Alternate), 04-002-5426 (Alternate), 04-002-8305 (Alternate), 04-004-4339 (Primary), 04-004-5524 (Alternate), 04-004-9022 (Alternate), 04-006-2300 (Alternate), 04-006-5878 (Alternate), 04-006-7679 (Alternate), 04-006-7954 (Alternate), 04-006-9855 (Alternate), 04-007-4751 (Alternate), 04-008-0367 (Alternate), 04-008-2588 (Alternate), 04-008-6531 (Alternate), 04-008-8214 (Alternate), 04-010-6452 (Alternate)
**CAS Number - PR:** 1314-23-4 **Entry Date:** 09/01/1987

**References:**

| Type | DOI | Reference |
|---|---|---|
| Primary Reference | | McMurdie, H., Morris, M., Evans, E., Paretzkin, B., Wong-Ng, W., Hubbard, C. Powder Diffr. 1, 275 (1986). |
| Crystal Structure | | Crystal Structure Source: LPF. |
| Structure | | (1) McCullough, J., Trueblood, K. Acta Crystallogr. 12, 507 (1959). |
| Structure | | (2) Smith, D., Newkirk, H. Acta Crystallogr. 18, 983 (1965). |

**Database Comments:** Additional Patterns: To replace 00-013-0307 and 00-036-0420 and validated by calculated pattern 00-024-1165. See PDF 01-072-1669, 01-072-0597, 01-074-0815 and 01-078-0050. Analysis: Spectrographic analysis showed that this sample contained less than 0.01% each of Al, Hf and Mg and between 0.1 and 0.01% each of Fe, Si and Ti. Color: Colorless. General Comments: Pattern reviewed by Holzer, J., McCarthy, G., North Dakota State Univ., Fargo, North Dakota, USA, ICDD Grant-in-Aid (1990). Agrees well with experimental and calculated patterns. Additional weak reflections (indicated by brackets) were observed. Polymorphism/Phase Transition: There are a number of polymorphic forms of "Zr O2" stable at different temperatures and pressures. Sample Source or Locality: Sample was obtained from Titanium Alloy Manufacturing Co. (1990) and was heated to 1300° for 48 hours. Structures: The structure of "Zr O2" (baddeleyite) was determined by McCullough and Trueblood (1) and confirmed by Smith and Newkirk (2). Temperature of Data Collection: The mean temperature of the data collection was 298.5 K. Unit Cell Data Source: Powder Diffraction.

**d-Spacings (59) - Zr O2 - 00-037-1484 (Stick, Fixed Slit Intensity) - Cu Kα1 1.54056 Å**

| 2θ (°) | d (Å) | I | h | k | l | * | 2θ (°) | d (Å) | I | h | k | l | * | 2θ (°) | d (Å) | I | h | k | l | * |
|---|---|---|---|---|---|---|---|---|---|---|---|---|---|---|---|---|---|---|---|---|
| 17.4186 | 5.087010 | 3 | 0 | 0 | 1 | | 28.1743 | **3.164700** | 100 | -1 | 1 | 1 | | 34.3821 | 2.606180 | 11 | 0 | 2 | 0 | |
| 24.0474 | 3.697650 | 14 | 1 | 1 | 0 | | 31.4672 | **2.840630** | 68 | 1 | 1 | 1 | | 35.3082 | 2.539920 | 13 | 0 | 0 | 2 | |
| 24.4404 | 3.639070 | 10 | 0 | 1 | 1 | | 34.1591 | 2.622680 | 21 | 2 | 0 | 0 | | 35.8991 | 2.499450 | 2 | -2 | 0 | 1 | |

| 2θ (°) | d (Å) | I | h | k | l | * |
|---|---|---|---|---|---|---|
| 38.3953 | 2.342500 | 1 | -2 | 1 | 0 | E |
| 38.5400 | 2.334040 | 4 | 1 | 2 | 0 | |
| 39.4099 | 2.284500 | <1 | 0 | 1 | 2 | |
| 39.9890 | 2.252740 | <1 | -2 | 1 | 1 | |
| 40.7239 | 2.213770 | 12 | -1 | 1 | 2 | |
| 41.1489 | 2.191880 | 5 | 2 | 0 | 1 | |
| 41.3729 | 2.180530 | 5 | -1 | 2 | 1 | |
| 44.8248 | 2.020300 | 7 | 2 | 1 | 1 | |
| 45.5209 | 1.991010 | 6m | -2 | 0 | 2 | |
| 48.9477 | 1.859330 | 2 | -2 | 1 | 2 | |
| 49.2649 | 1.848100 | 18 | 2 | 2 | 0 | |
| 50.1145 | **1.818740** | 22 | 0 | 2 | 2 | |
| 50.5578 | 1.803830 | 13 | -2 | 2 | 1 | |
| 51.1917 | 1.782970 | 5 | -1 | 2 | 2 | |
| 54.1027 | 1.693710 | 11m | 0 | 0 | 3 | |
| 54.6784 | 1.677230 | <1 | 2 | 2 | 1 | |
| 55.2689 | 1.660700 | 11 | 1 | 2 | 2 | E |
| 55.3985 | 1.657120 | 11 | 3 | 1 | 0 | |
| 55.5686 | 1.652450 | 9 | -3 | 1 | 1 | |
| 55.8814 | 1.643940 | 6 | 0 | 3 | 1 | |
| 57.1665 | 1.610000 | 7m | -1 | 1 | 3 | |
| 57.8596 | 1.592350 | 4 | -1 | 3 | 1 | |
| 58.2663 | 1.582200 | 3 | -2 | 2 | 2 | |
| 59.7733 | 1.545860 | 8 | 1 | 3 | 1 | |
| 60.0533 | 1.539320 | 7 | -2 | 0 | 3 | |
| 61.3652 | 1.509520 | 5 | 3 | 1 | 1 | |
| 61.9825 | 1.495960 | 5 | -3 | 1 | 2 | |
| 62.8363 | 1.477670 | 8 | 1 | 1 | 3 | |
| 64.0774 | 1.452010 | 1 | 3 | 2 | 0 | |
| 64.2483 | 1.448560 | 2 | 2 | 3 | 0 | |
| 64.9640 | 1.434320 | <1 | 0 | 3 | 2 | |
| 65.3819 | 1.426160 | 2 | -2 | 3 | 1 | |
| 65.6981 | 1.420060 | 6m | 0 | 2 | 3 | |
| 65.8821 | 1.416540 | 4 | -1 | 3 | 2 | |
| 68.9099 | 1.361500 | 1 | 2 | 3 | 1 | |
| 69.6182 | 1.349370 | <1 | 3 | 2 | 1 | |
| 70.1883 | 1.339800 | <1 | -3 | 2 | 2 | |
| 71.0692 | 1.325340 | 2 | -2 | 2 | 3 | |
| 71.2978 | 1.321650 | 4 | -4 | 0 | 1 | |
| 71.9479 | 1.311300 | 1 | 4 | 0 | 0 | |
| 72.1017 | 1.308880 | 1 | -2 | 3 | 2 | |
| 72.4477 | 1.303480 | <1 | 0 | 4 | 0 | |
| 72.6401 | 1.300500 | <1 | 3 | 1 | 2 | |
| 73.5782 | 1.286220 | <1 | -3 | 1 | 3 | |
| 74.6800 | 1.269950 | 2 | 0 | 0 | 4 | |
| 75.0440 | 1.264690 | 4 | 1 | 4 | 0 | |
| 76.4076 | 1.245480 | 1 | -1 | 1 | 4 | |
| 77.3895 | 1.232110 | <1 | 3 | 3 | 0 | |
| 78.0764 | 1.222980 | <1 | 4 | 0 | 1 | |
| 78.8640 | 1.212730 | 1m | 0 | 3 | 3 | |

# Appendix B

**00-050-1089** Jul 20, 2017 3:51 PM (Metoxidid Oxidos)

**Status** Primary **QM:** Star **Pressure/Temperature:** Ambient **Chemical Formula:** Zr O2
**Empirical Formula:** O2 Zr **Weight %:** O25.97 Zr74.03 **Atomic %:** O66.67 Zr33.33
**Compound Name:** Zirconium Oxide

**Radiation:** CuKα1 **λ:** 1.5405 Å **Filter:** Ni Beta **d-Spacing:** Diff. **Intensity:** Diffractometer

**SYS:** Tetragonal **SPGR:** P42/nmc (137)
**Author's Cell [ AuthCell a:** 3.5984(5) Å **AuthCell c:** 5.152(1) Å **AuthCell Vol:** 66.71 Å³ **AuthCell Z:** 2.00
**AuthCell MolVol:** 33.35 ] **Author's Cell Axial Ratio [ c/a:** 1.432 ] **Density [ Dcalc:** 6.134 g/cm³ ]
**SS/FOM:** F(18) = 55.3(0.0136, 24) **Temp:** 298.0 K (Ambient temperature assigned by ICDD editor)

**Space Group:** P42/nmc (137) **Molecular Weight:** 123.22
**Crystal Data [ XtlCell a:** 3.598 Å **XtlCell b:** 3.598 Å **XtlCell c:** 5.152 Å **XtlCell α:** 90.00°
**XtlCell β:** 90.00° **XtlCell γ:** 90.00° **XtlCell Vol:** 66.71 Å³ **XtlCell Z:** 2.00 ]
**Crystal Data Axial Ratio [ c/a:** 1.432 **a/b:** 1.000 **c/b:** 1.432 ]
**Reduced Cell [ RedCell a:** 3.598 Å **RedCell b:** 3.598 Å **RedCell c:** 5.152 Å **RedCell α:** 90.00°
**RedCell β:** 90.00° **RedCell γ:** 90.00° **RedCell Vol:** 66.71 Å³ ]

**Atomic parameters are cross-referenced from PDF entry 04-005-4479** **ADP:** B **Origin:** O2
**Crystal (Symmetry Allowed):** Centrosymmetric

**SG Symmetry Operators:**

| Seq | Operator | Seq | Operator | Seq | Operator | Seq | Operator |
|---|---|---|---|---|---|---|---|
| 1 | x,y,z | 5 | x,-y+1/2,z | 9 | y,x,z+1/2 | 13 | y,-x+1/2,z+1/2 |
| 2 | -x,-y,-z | 6 | -x,y+1/2,-z | 10 | -y,-x,-z+1/2 | 14 | -y,x+1/2,-z+1/2 |
| 3 | -x+1/2,y,z | 7 | -x+1/2,-y+1/2,z | 11 | -y+1/2,x,z+1/2 | 15 | -y+1/2,-x+1/2,z+1/2 |
| 4 | x+1/2,-y,-z | 8 | x+1/2,y+1/2,-z | 12 | y+1/2,-x,-z+1/2 | 16 | y+1/2,x+1/2,-z+1/2 |

**Atomic Coordinates:**

| Atom | Num | Wyckoff | Symmetry | x | y | z | SOF | Biso | AET |
|---|---|---|---|---|---|---|---|---|---|
| Zr | 1 | 2a | -4m2 | 0.75 | 0.25 | 0.75 | 1.0 | 0.41 | 8-a |
| O | 2 | 4d | 2mm. | 0.25 | 0.25 | 0.4546 | 1.0 | 0.36 | 10-a |

**Subfile(s):** Ceramic (Bioceramic), Common Phase, Forensic, Inorganic, Metals & Alloys, Superconducting Material
**Prototype Structure [Formula Order]:** Zr O2 **Prototype Structure [Alpha Order]:** O2 Zr
**LPF Prototype Structure [Formula Order]:** Zr O2,tP6,137 **LPF Prototype Structure [Alpha Order]:** O2 Zr,tP6,137
**Pearson Symbol:** tP6.00

**Cross-Ref PDF #'s:** 01-088-1007 (Alternate), □ 04-005-4207 (Primary), □ 04-005-4479 (Alternate), □ 04-005-4504 (Alternate), □ 04-006-0278 (Alternate), □ 04-012-8132 (Alternate)

**Entry Date:** 09/01/2000

**References:**

| Type | DOI | Reference |
|---|---|---|
| Primary Reference | | Malek, J., Benes, L., Mitsuhashi, T. Powder Diffr. 12, 96 (1997). |
| Crystal Structure | | Crystal Structure Source: LPF. |

**Database Comments:** Additional Patterns: See PDF 01-088-1007. General Comments: t-Phase. Tetragonal phase is stable between 1170 C and 2370 C. Pattern taken on metastable phase at room temperature. Sample Preparation: An ammonia solution was added to a solution of "Zr O Cl2" to form a gel. The partially dried gel was slowly heated to 600 C under nitrogen, then quenched to room temperature. Unit Cell Data Source: Rietveld or profile fit analysis.

**d-Spacings (18) - Zr O2 - 00-050-1089 (Stick, Fixed Slit Intensity) - Cu Kα1 1.54056 Å**

| 2θ (°) | d (Å) | I | h | k | l | * | 2θ (°) | d (Å) | I | h | k | l | * | 2θ (°) | d (Å) | I | h | k | l | * |
|---|---|---|---|---|---|---|---|---|---|---|---|---|---|---|---|---|---|---|---|---|
| 30.2700 | **2.950200** | 100 | 0 | 1 | 1 | | 59.6102 | 1.549700 | 14 | 0 | 1 | 3 | | 82.4750 | 1.168540 | 6 | 0 | 3 | 1 | |
| 34.8111 | 2.575040 | 8 | 0 | 0 | 2 | | 60.2052 | **1.535800** | 24 | 1 | 2 | 1 | | 84.1955 | 1.148990 | 4 | 1 | 1 | 4 | |
| 35.2553 | 2.543610 | 12 | 1 | 1 | 0 | | 62.9673 | 1.474910 | 7 | 2 | 0 | 2 | | 84.9171 | 1.141060 | 3 | 2 | 2 | 2 | |
| 43.1384 | 2.095290 | 1 | 0 | 1 | 2 | | 73.4644 | 1.287930 | 3 | 0 | 0 | 4 | | 85.2234 | 1.137740 | 3 | 1 | 3 | 0 | |
| 50.3767 | **1.809890** | 43 | 1 | 1 | 2 | | 74.5378 | 1.272020 | 5 | 2 | 2 | 0 | | 94.7153 | 1.047150 | 3 | 0 | 2 | 4 | |
| 50.7107 | 1.798750 | 22 | 0 | 2 | 0 | | 81.9713 | 1.174440 | 11 | 1 | 2 | 3 | | 95.4772 | 1.040800 | 9 | 1 | 3 | 2 | |